



HAL
open science

Printed flexible antenna for energy harvesting

Do Hanh Ngan Bui

► **To cite this version:**

Do Hanh Ngan Bui. Printed flexible antenna for energy harvesting. Optics / Photonic. Université Grenoble Alpes, 2017. English. NNT : 2017GREAT062 . tel-01721461

HAL Id: tel-01721461

<https://theses.hal.science/tel-01721461>

Submitted on 2 Mar 2018

HAL is a multi-disciplinary open access archive for the deposit and dissemination of scientific research documents, whether they are published or not. The documents may come from teaching and research institutions in France or abroad, or from public or private research centers.

L'archive ouverte pluridisciplinaire **HAL**, est destinée au dépôt et à la diffusion de documents scientifiques de niveau recherche, publiés ou non, émanant des établissements d'enseignement et de recherche français ou étrangers, des laboratoires publics ou privés.

THÈSE

Pour obtenir le grade de

DOCTEUR DE LA COMMUNAUTE UNIVERSITE GRENOBLE ALPES

Spécialité : **Optique et Radiofréquences**

Arrêté ministériel : 25 mai 2016

Présentée par

Do Hanh Ngan BUI

Thèse dirigée par **Philippe BENECH** Professeur, Université
Grenoble-Alpes et
codirigée par **Tan-Phu VUONG**, Professeur, Grenoble INP, et
Jacques VERDIER, Maître de conférences, INSA de Lyon

préparée au sein du **Laboratoire IMEP-LAHC**
dans l'**École Doctorale Électronique, Électrotechnique,
Automatique et Traitement du signal (EEATS)**

Antennes souples imprimables pour la récupération d'énergie de champs électromagnétiques ambiants

Thèse soutenue publiquement le **25 Octobre 2017**,
devant le jury composé de :

M. Bruno ALLARD

Professeur, INSA de Lyon, Président

M. Ke WU

Professeur, Polytechnique Montréal, Rapporteur

M. Laurent CIRIO

Professeur, Université Paris-Est Marne-la-Vallée, Rapporteur

Mme. Valérie VIGNERAS

Professeur, Institut Polytechnique de Bordeaux, Examinatrice

M. Philippe BENECH

Professeur, Université Grenoble-Alpes, Membre

M. Tan-Phu VUONG

Professeur, Grenoble INP, Membre

M. Jacques VERDIER

Maître de conférences, INSA de Lyon, Membre

M. Emmanuel DREINA

Docteur, Schneider Electric, Membre

M. Gael DEPRES

Docteur, Arjowiggins, Membre



Remerciements

Le travail de thèse a été financé par la région Auvergne Rhône-Alpes dans le cadre du projet ARC4-Energies. Ces travaux de thèse ont été réalisés aux Laboratoire IMEP LAHC à Grenoble et aux Laboratoire AMPERE à Lyon et rattaché à l'Institut Polytechnique de Grenoble.

Je tiens à remercier Monsieur Bruno Allard, Professeur de INSA de Lyon, pour l'intérêt porté à mes travaux et m'avoir fait honneur de présider le jury de ma thèse.

J'adresse toute ma connaissance à Monsieur Ke Wu, Professeur à Université Polytechnique Montréal – Canada et Monsieur Laurent Cirio, Professeur à Université Paris-Est Marne-la-Valée, qui ont cordialement accepté d'être rapporteurs de ce travail.

Un très grand merci à Madame Valérie Vigneras, professeuse à l'Institut Polytechnique de Bordeaux, Monsieur Emmanuel Dreina, docteur de Schneider Electric et Monsieur Gael Depres, docteur d'Arjowiggins Creative, pour avoir accepté d'être membre de jury de ma thèse.

Je remercie très chaleureusement mes directeurs de thèse, Monsieur Philippe Benech, Professeur à Université Grenoble Alpes, Monsieur Tan-Phu Vuong, Professeur à l'Institut Polytechnique de Grenoble et Monsieur Jacques Verdier, Maître de conférences à INSA de Lyon. Merci beaucoup pour vos conseils précieux, votre soutien, et surtout toute la confiance que vous avez su m'accorder.

J'adresse mes sincères remerciements à Monsieur Nicolas Corrao, Responsable de la plate-forme de caractérisation Hyperfréquences pour m'aider de réaliser les circuits et les mesures. Je tiens à remercier Monsieur Xavier Mescot, Responsable de la plate-forme de caractérisation électrique et physique pour votre aide de mettre à disposition du matériel et les explications techniques. Je tiens également à remercier Monsieur Antoine Pisa, technicien à Phelma, pour votre aide de fabriquer les circuits, toujours dans le meilleur délai.

Merci à tous les membres de l'IMEP-LAHC, en particulier mes collègues pour tous vos aides, vos encouragements et le temps qu'on a passé ensemble.

Enfin, je tiens à remercier ma famille et mes chers amis qui m'ont encouragé durant toutes ces années.

Contents

Introduction	13
1. State of the art	17
1.1 Solutions of energy harvesting	17
1.1.1 Ambient energy harvesting	17
1.1.2 Promising frequencies for ambient RF energy harvesting.....	18
a. Limitation standard.....	19
b. Available power densities.....	20
1.2 Rectenna structures for ambient RF energy harvesting.....	21
1.2.1 Techniques to increase RF-to-DC conversion efficiency of rectenna.....	22
a. Nonlinear device choices.....	22
b. Circuit topologies choices	24
c. Harmonic termination techniques	25
d. Impedance matching.....	26
1.2.2 Techniques to increase the harvested power	28
a. Combining techniques	28
b. Single-frequency: Multiple antennas in RF-combiner configuration.....	29
c. Single-frequency: Multiple antennas in DC-combiner configuration	30
d. Single-frequency: Multi-input of an antenna in DC-combiner configuration.....	31
e. Multi-frequency: Multiple single-band antennas and single-tone rectifiers	32
f. Multi-frequency: Wideband/Multiband antenna and single-tone rectifiers	33
g. Multi-frequency: Wideband/Multiband antenna and multi-tone rectifier	34
1.3 Flexible antenna in energy harvesting system	36
1.3.1 Antenna using flexible material.....	36
a. Textile material	36
b. Paper-based and polymer-based material.....	37
1.3.2 Techniques to increase realized gain of flexible antenna	38
1.3.3 Integration of flexible antenna in energy harvesting system.....	39
1.4 Conclusion	43
2. Antenna.....	45
2.1 Requirements of antenna for ambient energy harvesting.....	45
2.2 3D flexible multi-band antenna.....	46

2.2.1	Dipole-based antenna	47
a.	Antenna Configuration	47
b.	Simulation and measurement results	48
c.	Applying for printed antenna on flexible substrate	53
2.2.2	Coplanar-based antenna	55
a.	Antenna configuration.....	55
b.	Bending and folding analysis.....	58
c.	Fabrication and measurement.....	60
d.	Conclusion	64
2.3	Technique to overcome high-loss substrate	64
2.3.1	Design and characterization of suspended patch antenna.....	65
a.	Paper substrate characteristics	65
b.	Antenna configuration.....	65
2.3.2	Simulation and measurement results	66
2.3.3	Applying for flexible multi-band antenna with suspended ground.....	68
a.	Antenna configuration.....	68
b.	Simulation and measurements	68
2.4	Adjustable frequency antenna using flexible substrate	70
2.4.1	Antenna configuration.....	70
2.4.2	Simulation and measurement results	71
2.4.3	Conclusion.....	73
2.5	High gain flexible antenna.....	73
2.5.1	Target of design.....	73
2.5.2	Antenna configuration.....	74
2.5.3	Fabrication and measurement	74
2.6	Conclusion	75
3.	Rectifier	77
3.1	Diode modeling.....	78
3.1.1	Diode characterization	78
a.	Parameters of a Schottky diode.....	78
b.	Parameter extraction of equivalent circuit model.....	80

3.1.2	Measurements and results.....	81
a.	Extraction of I_s and n	81
b.	Extraction of R_s	82
c.	Extraction of R_j	82
d.	Discussion.....	83
3.1.3	Proposed physical-based model.....	84
a.	DC forward modeling.....	84
b.	DC reverse modeling.....	85
c.	C-V modeling.....	86
d.	S-parameter modeling.....	88
e.	Proposed model.....	89
3.2	Rectifier to combine different sources of energy.....	91
3.2.1	Energy addition at RF level using a diplexer.....	91
a.	Band-stop filter design.....	91
b.	Diplexer design:.....	93
c.	Fabrication and measurement.....	94
d.	Conclusion.....	96
3.2.2	Energy addition at DC level.....	96
a.	Design of rectifier with 1-input at 2.45GHz.....	96
b.	Design of rectifier with two inputs at 2.45 GHz.....	101
3.3	Conclusion.....	102
4.	Global system and measurements.....	103
4.1	Co-design.....	103
4.1.1	Impedance matching in co-design rectenna.....	104
4.1.2	Choosing matching impedance.....	106
4.2	Operation of spatial diversity rectenna in realistic environment.....	108
4.2.1	Diversity antenna concept.....	109
4.2.2	Rectenna design.....	110
a.	Antenna arrangement.....	110
b.	Rectifier structure.....	112
4.2.3	Experimental setup.....	114
4.2.4	Measurement results.....	115
a.	Antenna measurement.....	115

b.	Rectifier measurement.....	116
c.	Rectenna measurement in realistic environment.....	116
d.	Conclusion	120
4.3	Flexible diversity rectenna	120
4.3.1	Flexible diversity antenna design	121
a.	Antenna configuration.....	121
b.	Technique to reduce mutual coupling and enhance the antenna gain.....	122
4.3.2	Interface between antenna and rectifier.....	125
a.	On flexible-substrate rectifier	125
b.	Separate rectifier	126
4.3.3	Fabrication and measurement	127
a.	Fabrication	127
b.	Antenna measurement.....	128
c.	Diversity rectenna measurement in realistic environment.....	131
4.4	Conclusion	133
5.	Conclusion and perspectives.....	135
5.1	Conclusion	135
5.2	Perspectives	137
References.....		139
List of publications.....		151
List of acronyms and abbreviations.....		153
Résumé.....		155
Abstract.....		157

LIST OF FIGURES

Fig. 1-1 Basic architecture of a rectenna.....	21
Fig. 1-2 Relationship between the efficiency and losses in rectifying circuit as a function of input power [32][33].....	22
Fig. 1-3 State-of-the-art microwave rectifier circuits with various Schottky diodes [34]	23
Fig. 1-4 Simulation of Rectifier Figure of Merit of different topologies versus input power[6] ..	25
Fig. 1-5 Ideal Class-F rectifier topology used in circuit design [40]	26
Fig. 1-6 Schematic of the proposed circuit in [41]	26
Fig. 1-7 Harmonic termination of each diode [41]	26
Fig. 1-8 Antenna-rectifier circuit interface [43].....	26
Fig. 1-9 Prototyped rectenna (a) 50-Ω matched; (b) complex conjugately matched [48]	27
Fig. 1-10 Power conversion efficiency (PCE) of the rectennas show in Fig. 1-9 as a function of R_L, at $f=868$ MHz and $P_{in}=-10$ dBm.[48]	27
Fig. 1-11 Structures of multi-frequency solutions for RF energy harvesting	29
Fig. 1-12 Photo of the fabricated rectenna array in RF-combiner configuration [50].....	30
Fig. 1-13 Picture of the fabricated RF power harvester: Antenna array and rectifier array [51]31	
Fig. 1-14 Schematic of the rectifier in DC-combiner configuration [51].....	31
Fig. 1-15(a) Top view of radiating patch; (b) Bottom view of rectifier circuit [54].....	31
Fig. 1-16 DTV, GSM 900, GSM 1800 and 3G copper wire antennas [55].....	32
Fig. 1-17 Rectennas array architecture with individual PMMs [55]	32
Fig. 1-18 Multiband rectenna with wideband antenna and multiple single-tone rectifiers [56] 33	
Fig. 1-19 Multiband RF harvester schematic [56].....	33
Fig. 1-20 Schematic (a) and fabricated circuit (b) of the multitone rectifier with EPR [59]	34
Fig. 1-21 Antenna bent around bending gauge with 75 mm diameter [63]	36
Fig. 1-22 Embroidered textile AMF antenna on organza fabric [65].....	37
Fig. 1-23 Different way of folding antenna [69].....	37
Fig. 1-24 Structure of the conformal antenna ingestible wireless capsule [70]	38
Fig. 1-25 Fabricated antenna with the integration of a Fresnel lens [75].....	39
Fig. 1-26 Antenna with ground-backed FSSs design [79].....	39
Fig. 1-27 Proposed SIW cavity-backed slot antenna with integrated solar harvester [82]	40
Fig. 1-28 Designed of hybrid solar/EM energy harvester in different bent radius [83]	40
Fig. 1-29 Parylene interposer as thin flexible 3-D packaging enabler for wireless applications [84].....	40
Fig. 2-1 Configuration of the proposed antenna.....	48
Fig. 2-2 3-D structure of the proposed antenna.....	48
Fig. 2-3 Fabricated 3-D antenna	49

Fig. 2-4 Simulated (CST Time Domain) and measurement reflection coefficient of the proposed antenna.....	50
Fig. 2-5 Simulated far-field pattern of the antenna at 1800MHz.....	51
Fig. 2-6 Radiation Patterns of the antenna at GSM frequency (1800 MHz): (a) $\varphi = 0^\circ$ (b) $\varphi = 90^\circ$	51
Fig. 2-7 Radiation Patterns of the antenna at UMTS frequency (2100 MHz) (a) $\varphi = 0^\circ$ (b) $\varphi = 90^\circ$	51
Fig. 2-8 Radiation Patterns of the antenna at Wi-Fi frequency 2.45 GHz: (a) $\varphi = 0^\circ$ (b) $\varphi = 90^\circ$	52
Fig. 2-9 Radiation Patterns of the antenna at Wi-Fi frequency 5.2 GHz: (a) $\varphi = 0^\circ$ (b) $\varphi = 90^\circ$	52
Fig. 2-10 Foldable structure of proposed paper antenna.....	53
Fig. 2-11 Simulated reflection coefficient of 3D paper antenna at different values of h (mm)....	54
Fig. 2-12 Prototype of proposed paper antenna.....	54
Fig. 2-13 Prototypes of folded paper antenna (a) h=18 mm; (b) h=4 mm; (c) h=0 mm (flat antenna).....	55
Fig. 2-14 Simulation and measurement reflection coefficient of the paper substrate antenna in flat and folded configuration (h=0 mm and h=18 mm).....	55
Fig. 2-15 Configuration of the proposed co-planar antenna.....	56
Fig. 2-16 (a) Simulated results of reflection coefficient; Simulated results of radiation pattern at (b)900 MHz; (c)1800 MHz; (d) 2.6 GHz.....	58
Fig. 2-17 (a) Bending antenna in function of radius rbend; (b) folding antenna in function of length u; (c) folding antenna in function of width v.....	58
Fig. 2-18 Simulated reflection coefficient of bending antenna at different bending radius rbend (mm).....	59
Fig. 2-19 Simulated reflection coefficient of folding antenna at different folding length u (mm).....	59
Fig. 2-20 Simulated reflection coefficient of folding antenna at different folding width v (mm).....	59
Fig. 2-21 Fabricated antenna in flat, folding and bending configurations.....	61
Fig. 2-22 Simulation and measurement reflection coefficient of the flexible coplanar antenna, in planar state.....	61
Fig. 2-23 Simulated and measured reflection coefficient of the flexible coplanar antenna (a) by bending rbend=14 mm; (b) by folding along x-axis u=30 mm.....	61
Fig. 2-24 Radiation pattern of the antenna in flat configuration(a) at (b) 900 MHz; (c) 1800 MHz; (d) 2.6 GHz.....	62
Fig. 2-25 Radiation pattern of the antenna in bending configuration (a) on toward a cylindrical form rbend=14 mm: (b) 900 MHz; (c) 1800 MHz; (d) 2.6 GHz.....	62
Fig. 2-26 Radiation pattern of the antenna in folded configuration (a) along x-axis, u=30 mm: (b) 900 MHz; (c) 1800 MHz; (d) 2.6 GHz.....	62

Fig. 2-27 (a) Conventional microstrip patch antenna using high-loss substrate; (b) simulated surface current of conventional patch at 1800 MHz; (c) simulated results of reflection coefficient; (d) simulated results of E-plane radiation pattern at 1800 MHz	65
Fig. 2-28 Configuration of inverse suspended patch antenna	65
Fig. 2-29 Configuration of antenna before miniaturizing	66
Fig. 2-30 Configuration of the proposed antenna after miniaturizing: (a) Perspective view; (b) Side view; (c) Front view of radiating element	66
Fig. 2-31 Photo of fabricated prototype using adhesive copper: (a) Antenna before miniature (ANT1); (b) Antenna after miniature (ANT2); (c) Radiating element of miniaturized antenna (ANT2)	67
Fig. 2-32 Simulation and measurement of proposed antenna before miniature (ANT1): (a) Reflection coefficient; (b) E-plane radiation pattern at 1800 MHz	67
Fig. 2-33 Simulation and measurement of proposed antenna after miniature (ANT2): (a) Reflection coefficient; (b) E-plane radiation pattern at 1800 MHz	67
Fig. 2-34 Configuration of multi-band patch antenna (a) Flat antenna-top view; (b) Folded antenna -top view; (c) Folded antenna with suspended ground - side view	68
Fig. 2-35 Surface currents of proposed antenna at frequency (a) 1800 MHz and (b) 2.1 GHz	68
Fig. 2-36 Photo of fabricated suspended multi-band antenna using adhesive copper (a) top view before folded;(b) top view after folded; (c) side view.....	69
Fig. 2-37 Simulated and measured of reflection coefficient of multi-band suspended antenna	69
Fig. 2-38 Simulation and measurement of E-plane radiation pattern at two operational frequencies (a) 1800 MHz; (b) 2.1 GHz.....	69
Fig. 2-39 Configuration of proposed circuit (a) Antenna; (b) Cover box; (c) Feed network; (d) Side view	71
Fig. 2-40 Parameters of proposed antenna for (a) GSM 1800 MHz; (b) GSM 1900 MHz; (c) UMTS 2100 MHz; (d) WLAN 2.4 GHz	71
Fig. 2-41 Simulated far-field pattern of the antenna at four frequency bands.....	72
Fig. 2-42 Fabricated antenna with removable patch antenna for frequency of (a) 1800 MHz; (b) 1900 MHz; (c) 2100 MHz; (d) 2.4 GHz	72
Fig. 2-43 (a) Simulation and measurement of the reflection coefficient at four working frequencies; (b)E-plane radiation pattern at four frequencies.	73
Fig. 2-44 (a) Configuration of basic planar-printed quasi-Yagi structure; (b) Top view; (c) Bottom view.....	74
Fig. 2-45 Fabricated high gain antenna on flexible substrate	74
Fig. 2-46 E-plane radiation pattern of fabricated planar quasi-Yagi antenna.....	75
Fig. 3-1 Basic architecture of rectifier.....	77
Fig. 3-2 Equivalent circuit of the zero-bias Schottky diode.....	78

Fig. 3-3 $\ln I_1 - eqV/kT$ versus V_{in} for diode HSMS-2860	81
Fig. 3-4 IG_d versus current I for diode HSMS-2860	82
Fig. 3-5 Junction resistance R_j versus voltage bias V_{in} for diode HSMS-2860 (from measured data).....	82
Fig. 3-6 Measured and simulated current in reverse bias of diode HSMS 2860	83
Fig. 3-7 Measured and simulated current in forward bias of diode HSMS 2860	84
Fig. 3-8 Diode model after step #1, “DC forward bias modeling”	84
Fig. 3-9 Simulated and measured current in DC forward bias of diode HSMS 2860 (a) from 0 to 1.2V; (b) zooming from 0 to 0.1 V.....	85
Fig. 3-10 Diode model after step #2, “DC reverse model”	86
Fig. 3-11 Simulated and measured current in DC reverse bias of diode HSMS 2860	86
Fig. 3-12 Diode model after step #3, “C-V model”	87
Fig. 3-13 Total capacitance versus input voltage of diode HSMS2860	87
Fig. 3-14 Diode model at DC-OFF State (unbiased).....	88
Fig. 3-15 Simulated and measured S-parameters DC-Off state of diode HSMS2850	89
Fig. 3-16 Simulated and measured S-parameters (S11) DC-ON State of diode HSMS2850	89
Fig. 3-17 Three different types of diode packaging.....	89
Fig. 3-18 Physical-based diode model, compatible with ADS.....	90
Fig. 3-19 Proposed matching band-stop filter.....	92
Fig. 3-20 Simulation results of both filters as described in Fig. 3-19.....	93
Fig. 3-21 Simulated impedance of Filter 2	93
Fig. 3-22 Geometry of the diplexer: (a) Straight topology; (b) Meander topology	94
Fig. 3-23 Pictures of the fabricated circuits: (a) Filters; (b) Diplexer	94
Fig. 3-24 Simulated and measured reflection coefficient at common port	95
Fig. 3-25 Simulated and measured transmission coefficient at Port 2 and Port 3.....	95
Fig. 3-26 Simulated and measured reflection coefficient at Port 2 and Port 3	95
Fig. 3-27 Schematic of single stage voltage-doubler rectifier.....	97
Fig. 3-28 Dimensions and construction of an ceramic chip capacitor extracted from [130].....	97
Fig. 3-29 Equivalent model of an SMD capacitor	97
Fig. 3-30 Equivalent model of a thick film resistor	98
Fig. 3-31 Rectifier schematic for HB simulation.....	99
Fig. 3-32 Fabricated 1-input rectifier using diode HSMS 2850	100
Fig. 3-33 Simulated and measured efficiencies of 1-input rectifier using diode HSMS2850 versus input power with $R_{load}=6800k\Omega$	100
Fig. 3-34 Schematic of the two-input rectifier.....	101
Fig. 3-35 Fabricated two-input rectifier.....	102

Fig. 3-36 Simulation and measurement efficiencies of rectifier versus input power using diode HSMS 2850.....	102
Fig. 4-1 Design challenges of the system.....	103
Fig. 4-2 Antenna- Rectifier circuit interface.....	104
Fig. 4-3 Input voltage versus resistance R_{in} with $P_{deliver} = 2.4 \mu W$	106
Fig. 4-4 (a) Schematic model of the rectifier using diode SMS 7630; (b) Input impedance of diode SMS 7630 at $P_{in}=0.32 \mu W$; $f=2.45$ GHz; Load is optimized at maximum power point	107
Fig. 4-5 Input voltage versus resistance R_{in} with $P_{deliver}= 0.32 \mu W$ ($f=2.45$ GHz)	107
Fig. 4-6 (a) Planar array antenna; (b) Simulated radiation pattern of each antenna at 2.45 GHz; (c) E-plane of both four antennas at 2.45 GHz.....	111
Fig. 4-7 (a) 3D array antenna; (b) Simulated radiation pattern of each antenna at 2.45 GHz ; (c) E-plane of both four antennas at 2.45 GHz.	111
Fig. 4-8 Structure of proposed antenna diversity	111
Fig. 4-9 Mutual coupling between antenna (dB)	112
Fig. 4-10 Structure of proposed rectifiers: (a) Rectifier A- Single input rectifier schematic; (b) Rectifier B- Multi-input rectifier schematic	113
Fig. 4-11 Simulated output power versus different levels DeltaP between branches of rectifiers.	114
Fig. 4-12 Photo of fabricated Rectenna: (a) Rectifier A; (b) Rectifier B and 4 antennas.....	114
Fig. 4-13 Measurement setup	115
Fig. 4-14 Comparison of S-parameters between simulation and experimental results for both fabricated antennas.	116
Fig. 4-15 Measured output power versus input power of rectifier A and B	116
Fig. 4-16 Probability density function of input power (dBm) in different directions of antenna	117
Fig. 4-17 Cumulative density function of input power (dBm) in different directions of antenna	117
Fig. 4-18 Output voltage distribution of each antenna (mV): (a) Antenna 1; (b) Antenna 2; (c) Antenna 3 (d) Antenna 4; (e) Four Antennas.....	118
Fig. 4-19 Probability densities function of harvested power (nW) by various antennas.....	118
Fig. 4-20 Cumulative density function of harvested power (nW) in different scenarios of the multi-antenna system	119
Fig. 4-21 Design of feed-line to connect to common circuit (a) original solution; (b) Proposed configuration.....	121
Fig. 4-22 (a) Simulated reflection coefficient; (b) Radiation pattern of proposed antenna.....	122

Fig. 4-23 (a) Configuration of four antennas in the system packaging; (b) S-parameters of four antennas.....	122
Fig. 4-24 (a) Detail of inclined position of driven and director element; (b) Mutual coupling in function of da.....	123
Fig. 4-25 Configuration of flat structure: (a) Top view; (b) Bottom view.....	123
Fig. 4-26 Mutual coupling between two antennas ANT1 and ANT2 in system	124
Fig. 4-27 Structure of proposed diversity antenna: (a) Perspective view; (b) Bottom view.....	124
Fig. 4-28 (a) Simulated reflection coefficient; (b) Radiation pattern of the proposed diversity antenna.....	124
Fig. 4-29 (a) On-flexible-substrate rectifier with the antenna diversity; (b) Details of the rectifier circuit.....	125
Fig. 4-30 Simulated efficiency of the rectifiers using PET and Rogers 4003 substrate depending on input power with deltaP between ports is 5 dB.	126
Fig. 4-31 Transition part between antenna and circuit: (a) Top view; (b) Side view	126
Fig. 4-32 Simulated S-parameters of the transition part	127
Fig. 4-33 (a) Prototype of one antenna attached to the ground plane: (b) Simulation and experimental of reflection coefficient.....	128
Fig. 4-34 Details of the end-launch connector in order to perform the measurement.....	128
Fig. 4-35 Photo of fabricated rectenna before folding	128
Fig. 4-36 (a) Details of the end launch connector in order to perform the measurement; (b) Simulation and measurement of reflection coefficient of four antennas in the diversity antenna system.....	129
Fig. 4-37 (a) Photo of 3D diversity antenna with end-launch connectors; (b) Mutual coupling between antenna ANT1 and others antennas (in dB)	130
Fig. 4-38 Simulation and measurement of E-plane radiation pattern of four antennas.....	130
Fig. 4-39 (a) fabricated 4-port rectifiers with transition part; (b) connected diversity rectenna (bottom view); (c) connected diversity rectenna (top view).....	131
Fig. 4-40 Two completed diversity rectenna (a) With separated rectifier (Rectenna 2); (b) With on-flexible substrate rectifier (Rectenna 3)	131
Fig. 4-41 Probability density function (PDF) of harvested power (nW) from four rectennas...	132
Fig. 4-42 Cumulative density function (CDF) of harvested power (nW) from four rectennas ..	132

LIST OF TABLES

Table 1-1 Available power density summary of ambient energy harvesting.....	18
Table 1-2 Limited reference max level defined by ANRF [22].....	19
Table 1-3 Summary the overall analysis of the 2955 measurement results [25]	20
Table 1-4 Summary of available power levels in ambient RF frequency (adapted from [10], [24]-[31]).....	21
Table 1-5 Main parameters of most popular Schottky diodes [36].....	23
Table 1-6 Most suitable rectification mode versus R_S and V_{Br} [39]	25
Table 1-7 References of combining rectenna design.....	35
Table 1-8 Comparison of the flexible antennas in literature	41
Table 2-1 Designed parameters of the proposed antenna	49
Table 2-2 Comparison of reflection coefficient between simulation and measurement at targeted frequencies.....	50
Table 2-3 Comparison of performances between simulation and measurement at targeted frequencies.....	52
Table 2-4 Comparison of simulated gain between two prototypes	54
Table 2-5 Influence of parameters of proposed antenna	57
Table 2-6 Optimized parameter values of the proposed antenna	57
Table 2-7 Simulated gain of proposed antenna at different configurations	60
Table 2-8 Measured gain of proposed antenna at three configurations	62
Table 2-9 Comparison between coplanar flexible antennas presented in the literature (λ_g is guided wavelength at lowest resonant frequency)	63
Table 2-10 Simulated and measured gain (dBi) at each frequency	73
Table 3-1 Extracted parameters from the measurement in comparison with nominal values provided in the device's datasheet.....	83
Table 3-2 Extracted parameters of 3 different diodes.....	90
Table 3-3 Parameters of two filters	92
Table 3-4 Comparison between proposed diplexer and references.....	96
Table 3-5 Typical values of parasitic elements of SMD capacitor (C=1 pF) at 25° C, 2.45 GHz	98
Table 3-6 Typical value of parasitic elements in thick film resistor.....	98
Table 4-1 Calculated power delivered to the input of rectifier circuit	105
Table 4-2 Measurement scenarios	115
Table 4-3 Comparison of harvested power (HP) between configurations	119
Table 4-4 Optimized width of the transmission line in the transition part	127
Table 4-5 Measured bandwidth of four antennas at 2.4 GHz	129
Table 4-6 Comparison of S-parameters between simulation and measurement at 2.45 GHz... 	130
Table 4-7 Comparison of performance between configurations	133

Introduction

Internet-of-Things (IoT) and the growing development of inter-networking devices require exploiting all possible energy sources for energy-autonomous sensor. Ambient energy resources, especially those present in the human environment, that are generally renewable and/or "quasi-free", are limited but may be sufficient for different applications. Many generators can convert mechanical, thermal, photovoltaic, chemical, biological or radio frequency energy into electrical energy. When there is no light, when the object is not moving or when there is no temperature gradient, the ambient electromagnetic field, even with extremely small amplitude is then a credible alternative to supply an object with a low rate of activity.

The energetic requirements of the sensors were discussed in the literature and a floor value of $10 \mu\text{J}$ per 24 hours was underlined for lost sensors [1]. This consumption value is compatible with ambient electromagnetic fields with amplitude of less than -20 dBm . Harvesting electromagnetic energy receives more attention in terms of research in relation to the problem of wireless power transfer. Nikola Tesla has introduced first the concept of rectenna [2], that is the combination of an antenna and an electronic circuit rectifying the radio-frequency signal. In order to target high performance while operating with power density below -30 dBm , the design of rectenna remains the major problem of the antenna and recovery scenarios.

The IoT cannot be satisfied with a rigid and cumbersome antenna; applications like active dressing or other kinds of applications can be addressed require that the electronic functionalization of the dressing does not incommode its use. The structural and geometric richness of the IoT system requires also the flexibility of the harvester in terms of form and configuration. It is therefore essential to establish the autonomy of the smart function on a harvester based on flexible antennas. The realization of passive components by printing, such as an antenna, is already the object of research [3]. Part of the innovation is related to the ability to manufacture antennas on paper or textile, with the possibility of a high degree of recycling. In addition, the electrical performances of the antenna must be controlled within energy harvesting scenarios. Indeed the mechanical flexibility of the antenna will cause its morphology to be altered. The electronic part of the harvester must therefore anticipate this variability of the characteristics of the antenna.

This thesis, therefore, falls into several distinct aspects:

Antenna design: the design of the antenna will be based on several features, such as the bandwidths to be sought for energy harvesting, operation under non-optimal conditions, given the

flexible support may lead to modification of the surface of the antenna. Electromagnetic simulation tools will be used to optimize the most suitable antenna geometry. The antenna may consist of several associated radiating portions to cover all useful frequency bands. An important study is conducted on the connection between the radiating element (s) and the electronics.

The materials: the project aims to take advantage of the printing possibilities on various flexible supports. The main problems in terms of materials will be to obtain a metallic layer, which is sufficiently powerful to minimize the losses of the conductor and to have a support material whose dielectric properties are sufficient to obtain an efficient antenna.

Associated electronics: low-power energy circuits are of interest when low-power sources are available for stand-alone wireless sensor applications. This discipline combines the concepts of power electronics to achieve high conversion efficiency and microelectronics for technological realization. A low voltage starting circuit must be integrated into the structure of the rectenna. In addition, the possibility of addressing several frequency bands and several levels of input power necessitates reconfiguring the rectenna actively. This degree of freedom constitutes at the same time a constraint for the design of the antenna.

The final objective of the thesis is to realize a stand-alone demonstrator in energy of the sensor type on paper, polymer or textile.

This manuscript is organized in four chapters. The first chapter gives a review of energy harvesting solutions in the literature. It includes the review of various rectenna structures for ambient RF energy harvesting; especially the techniques allow increasing the RF-to-DC conversion efficiency of rectenna and increasing the harvested power. This section also mentions the development of flexible antenna using different materials such as textile, paper, and polymer. Due to the specific characteristic of the material, the flexible antenna suffers from low performances, from high-losses, and from super thin thickness. Therefore, techniques to increase realized gain of the flexible antenna are revisited.

In the second chapter, several antennas are proposed corresponding to varied techniques allowing increasing the performance of the energy harvester. Aware of the low-density power in the ambiance, solutions of combinations in frequency and space are proposed. All antenna's configurations aim to meet a requirement for integration within an object or system packaging. It includes the 3D flexible multi-band antennas, the technique to overcome high losses substrate, the adjustable frequency antenna solution and the design of the high gain flexible antenna. The geometry of these antennas is introduced together with the results of simulations and measurements.

Chapter 3 addresses the modeling of nonlinear devices in rectifying circuit. Several low barrier Schottky diodes are analyzed in order to propose a more precise model for low power energy

harvesting system design. The diodes are characterized and their physical-based model was proposed, based on parameter extraction method. Otherwise, in the approach of energy combination, a diplexer for energy addition at RF level and several rectifier structures for energy addition at DC level along with experimental results are presented.

Chapter 4 gives an overall review of the global system in two aspects: the co-design and the operation of rectenna in a realistic environment. The detailed analysis of the impedance matching in co-design rectenna is included in this section. This helps to clarify the condition and suitable impedance at the interface of antenna-circuit in order to make the decision in the pre-design phase. Eventually, the global systems of antenna and rectifier circuit using spatial diversity conception and combining several sources at DC level are designed and are tested in a realistic environment. The conventional patch antenna and circuit on Rogers substrate are then compared with a system designed on a flexible substrate. The analysis of probability density functions, cumulative density functions of harvested power in ambient is conducted and experimental results are discussed.

Finally, we summarize the work carried out in this thesis. The future perspectives concerning the design of flexible rectenna to take account the environment are presented.

1. State of the art

Energy harvesting from the ambient energy source is attracting attention for decades, as it is a potential alternative replacement or range extender for batteries in some applications, especially in low-power applications. It is also in some harsh applications the only practical way to supply a remote and lost sensor for example. This section introduces some facts from literature. It puts ambient RF energy harvesting in the frame of the expanding world of energy scavenging and harvesting. The transducer of RF energy harvesting is revisited. Particularly, the flexible antenna using in the RF energy harvesting system is investigated here.

1.1 Solutions of energy harvesting

1.1.1 Ambient energy harvesting

The classification of available ambient energy can be organized according to their characteristics as human body energy, natural energy, mechanical energy, thermal energy, light energy, biomass energy and electromagnetic energy [4].

Table 1-1 shows a summary of the power density of several common ambient power sources. Comparing to other sources, ambient RF energy offers a very limited power density. The solar cells offer the strongest power densities (up to mW/cm^3) and provide an excellent electrical source for many applications. However, the drawback of this technology is the solar panel which must be placed in a well-lighted location, correctly oriented and free from obstruction or shadow [5]. Indoor solar panels are becoming commercially available that simplifies indoor applications. Nevertheless, where there is only shadow, this approach is limited. The same state is true for mechanical sources, whether vibrational or not. The potential of scavenging from these sources is larger but some applications are in neutral position. Ambient RF energy, on the other hand, is free from these limitations. Because of more and more popular mobile communications, the RF waves are omnipresent in our living environment and fasten with our quotidian life. This work is focusing the microwave range frequencies. Electromagnetic energy in the frame of coupling (kHz), low or medium frequency (MHz) is not the topic covered here. The work in this manuscript comes in the continuity of numerous previous works [6]–[10].

Table 1-1 Available power density summary of ambient energy harvesting

Class of resource	Source of energy	Power density
Human body	Piezoelectric shoe inserts	5 W/(116 cm ² x 52 kg) [11] ~ 0.82 mW/cm ² /kg
	Heel strike	0.98 W/kg [12]
Natural energy (wind, water flow, ocean waves, solar energy)	Airflow	1 W/cm ² [4]
	Water flow	18 mW/m ³ s [13]
	Ocean waves	10 kW/m [14]
	Acoustic noise	0.003 μW/cm ³ @75 Db [15] 0.95 μW/cm ³ @ 100 Db [15]
	Indoor room light	6 μW/cm ³ [15]
	Solar cells	15 mW/cm ³ [16] [15] 150 μW/cm ³ (cloudy) [15]
Mechanical energy (vibration from machines and mechanical stress)	Micro-generator	100 μW/cm ³ [15] 116 μW/cm ³ [16]
	Piezoelectric	330 μW/cm ³ [16]
	Push buttons	50 J/N [4]
Thermal energy (waste heat energy variations)	Thermoelectric	40 μW/cm ³ [16]
	Daily temperature variation	10 μW/cm ³ [15]
	Temperature gradient	15 μW/cm ³ @10°C gradient [15]
Electromagnetic energy (inductor, coils, variable capacitor, radio frequency waves)	Inductor coupled coils	32 mW/cm ² [17]
	Electrostatic	4 mJ/cm ³ [4]
	Ambient Radio-Frequency	1 μW/cm ³ [18]

1.1.2 Promising frequencies for ambient RF energy harvesting

Nowadays, wireless applications using electromagnetic waves (radio, television, mobile phone, Wi-Fi, Wi-Max, Bluetooth, Lora, RFID, DSRG...) are becoming progressively accessible. This produces a significant presence of RF emitters in the environment. Most of these emitters are omnidirectional and permanent over time. The availability of this radiant energy in the ambience becomes interesting for low power applications. It has to be recognized that this is also a technological challenge because available energy exists in a very low power density, in range of μW-mW/m².

The first step in applying RF energy harvesting technology is to identify appropriate working frequencies and the maximum power to be emitted in order to estimate the level of power available in each frequency channel.

a. **Limitation standard**

In term of health protection and the limitation of the risks associated with electromagnetic fields, there are international and national standards to define levels of exposure to electromagnetic fields. A number of different national and international organizations have issued recommendations for the protection of human from exposure to electromagnetic fields and radiation in public and professional spaces. This part will give a review of the most important recommendations.

International Commission on Non-Ionizing Radiation Protection (ICNIRP) issued the guidelines for limiting exposure to time-varying electric, magnetic and electromagnetic fields [19]. The IEEE International Committee on Electromagnetic Safety (ICES) equally issued a standard for safety levels with respect to human exposure to radiofrequency electromagnetic fields from 3 kHz to 300 GHz [20]. The ICNIRP guidelines were adopted in the Recommendation of the Council of the European Union (EU) on public exposure to electromagnetic fields [21] and the vast majority of EU member countries follow this recommendation of the EU Council, either by incorporating it into its national regulations or in the form of recommendations. There are different approaches applied by some members with the introduction of more restrictive limits in "living places".

Table 1-2 Limited reference max level defined by ANRF [22]

Frequency bands (MHz)	Service	Electric field (V/m)	Magnetic field (A/m)	Power density S (W/m²)
87.5- 108	Radio FM	28	0.073	2
174-223	Radio RNT	28	0.073	2
380-470	PMR	28-29	0.073-0.08	2-2.3
470-790	Digital TV band IV, V	29-39	0.08-0.1	2.3-4
800	Mobile phone band	39	0.1	4
921-960	GSM 900, UMTS 900, GSM-R	41	0.1	4.5
1805-1880	GSM 1800	58	0.15	9
2100-2170	UMTS 2100	61	0.16	10
2450	WLAN	61	0.16	10
2600	LTE band 2600	61	0.16	10
3500	WiMAX	61	0.16	10
5150	WLAN	61	0.16	10

In France, the national agency of frequencies (ANFR) issued the code relating to the exposure limits of the people to the electromagnetic fields emitted by equipment used in telecommunication

networks or by radio installations [22]. The limited reference level of the electric field, magnetic field, and power density are presented in Table 1-2.

b. Available power densities

Conforming to the recommended limits, Equivalent Isotropically Radiated Power (EIRP) of each mobile telecommunication service is fixed by the standard in each country for the authorized frequency bands. Several studies have been conducted to analyze exposure levels to electromagnetic fields and estimate the available power in surrounding environments, in general, to define acceptable power levels.

The study in [23] estimated theoretically the power available from the main electromagnetic sources at a distance from transmitters determined by the services to which they are associated. According to this report, power available is about hundreds pW/cm² for radio and television services and about nW/cm² for GSM mobile and WLAN services.

The measurements in the realistic environment were also carried out by different research groups [10], [24]–[31]. The report [25] concerns the analysis of 2955 measures carried out in France in 2014; the level of electromagnetic radiated power has been analyzed through the combined contributions of all RF sources. Overall analyses in Table 1-3 showed a median field intensity of 0.38 V/m, equivalent to the power density of 38 nW/cm². The measured field levels are slightly higher in urban areas than in rural areas and slightly higher in outdoor areas than in indoor areas.

Table 1-3 Summary the overall analysis of the 2955 measurement results [25]

Locations	Number of measures	50% (median)	90%	99%	Max
Rural	472 (16%)	0.26 V/m	0.77 V/m	2.5 V/m	10.2 V/m
Urban	2483 (84%)	0.43 V/m	1.5 V/m	5.5 V/m	15.7 V/m
Indoor	1797 (61%)	0.31 V/m	1.3 V/m	4.7 V/m	10.4 V/m
Outdoor	1158 (39%)	0.53 V/m	1.6 V/m	5.6 V/m	15.7 V/m
TOTAL	2955	0.38 V/m	1.4 V/m	5 V/m	15.7 V/m

From frequency point of view, results in [25] also show that in approximately 57% of cases the most important signals correspond to the maximum exposure fields of cellular base station antennas from mobile telephone frequency (800 MHz, 900 MHz, 1800 MHz and 2100 MHz). The mobile telephone is also dominant in 75% of cases in the outdoor environment.

A spectral RF survey of the city was carried out in London [26] in more than 50 locations. The results also suggested that the power densities of available RF sources at outdoor environment are in the range of nW/cm².

In an office-like environment, the power density of WLAN signal is measured and estimated in [26], [29], [30], [31]. Level of WLAN power densities is smaller than telephone mobile energy, however, this type of source is stable over time and the antenna size is smaller. Table 1-4 presents the summary of different sources in ambient RF frequency.

According to available power levels, the frequency bands selected to harvest energy are, in order of priority: GSM 1800MHz, UMTS 2100MHz and GSM 900MHz and Wi-Fi 2.45 GHz. In addition, the 4G technology nowadays has been increasingly developed and implemented widespread, especially in the urban area. Therefore, LTE band at 2.6 GHz are still looked at though they are not included in the scope of this study.

Table 1-4 Summary of available power levels in ambient RF frequency (adapted from [10], [24]–[31])

Service	DTV	GSM900	GSM1800	UMTS 3G	Wi-Fi
Frequency (MHz)	400-800	900	1800	2100	2400
Antenna's size	Large	Average	Small	Small	Small
Energy					
<i>Main contributors outdoor [25]</i>	9%	75%			1%
<i>Main contributors indoor [25]</i>	16%	46%			11%
Density power (nW/cm²)					
[25] (median)	68	44	44	51	
[26] (average)	0.89	36	84	12	0.18
[27] (average)		13.5	5.1		
[10] (maximal)		3.95x10 ³	2x10 ³	17.8x10 ³	
[28]		100			
[29]					0.52
[30]					5.2-52
[31]		10-100	1-50		1

1.2 Rectenna structures for ambient RF energy harvesting

In the RF energy harvesting system, the most crucial element is the rectenna (rectifier and antenna) which has the role of receiving electromagnetic waves and converting them into electric DC energy. The basic structure of a rectenna consists of an antenna, an impedance matching circuit, a rectifying component, a DC filter and a resistance load (Fig. 1-1).

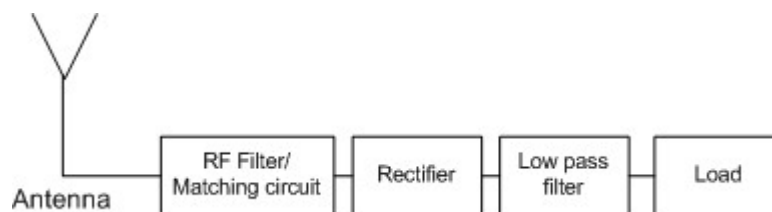


Fig. 1-1 Basic architecture of a rectenna

Nearly all modern energy harvesting circuit use semiconductor-based rectifying elements to convert RF to DC energy [32]. In RF energy harvesting system, the Schottky diode is chosen due to

the low threshold voltage and lower junction capacitance than PN diodes. This low threshold allows higher efficiency at low power input and the junction capacitance allows the diode to operate at RF frequency.

1.2.1 Techniques to increase RF-to-DC conversion efficiency of rectenna

A rectifying circuit that gives large DC voltage and high efficiency even if incident power levels are very low is desired. RF-to-DC conversion efficiency is an important characterization of the rectifier in the energy harvesting system and this one is decided mostly by the behavior of the diode.

The diode normally modeled by the nonlinear characteristic in three main regions of operation: reverse biased while below the reverse breakdown voltage (region 1), off-state while between breakdown voltage and turn on voltage (region 2) and forward biased (region 3) while above turn-on voltage. However, with a very low power density of ambient RF energy, the input voltage of rectifier is very low and the diode can operate only in the transition between region 2 and region 3. The diode is only in “on-state” for a small fraction of the RF wave period [32].

On the other hand, circuit losses come from the impedance mismatch as harmonic generation and the device parasitic such as junction resistance and junction capacitance of diode can decrease significantly the circuit efficiency. Therefore, techniques to increase the power conversion efficiency concentrate on the behavior of the diode and various topologies concerning the diode.

a. *Nonlinear device choices*

The diode parameters have a crucial role to maximize power conversion efficiency of rectifying circuit. Fig. 1-2 shows the impact of the diode main parameters on the rectifying circuit efficiency [32] [33].

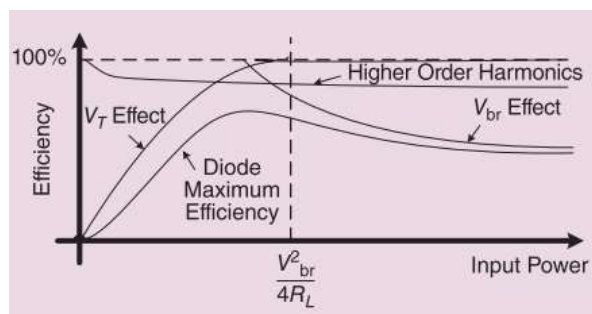


Fig. 1-2 Relationship between the efficiency and losses in rectifying circuit as a function of input power [32][33]

- The threshold voltage V_T is the most important parameter especially in ambient RF energy harvesting because it limits efficiency at low input power (V_T effect).

- The reverse breakdown voltage V_{Br} also limits the diode efficiency as this allows energy to short the diode demonstrated by V_{Br} effect. However, in the very low power system, input power is not high enough to exceed this voltage.
- The parasitic junction resistance R_s will dissipate power in the semiconductor junction, therefore, limits diode efficiencies [33].
- The parasitic junction capacitance C_j and junction resistance R_s constitute a low-pass filter, which limits the maximum operating frequency of the diode.

For these reasons, a careful choice of the diode with low threshold voltage, high reverse breakdown voltage, low series resistance and low junction capacitance can naturally increase the efficiency of the circuit. Nevertheless, due to the limitation in device material and fabrication, it is difficult to obtain all the optimal values simultaneously.

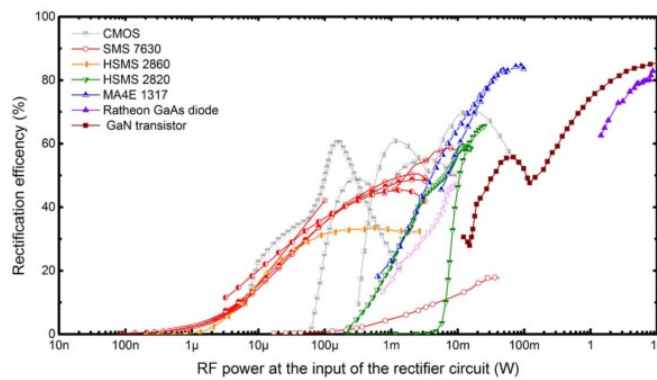


Fig. 1-3 State-of-the-art microwave rectifier circuits with various Schottky diodes [34]

The work of Hemour *et al.* [34] provides the state-of-the-art rectifiers reported in the literature with Schottky diodes. All the work reported in Fig. 1-3 is related to very different researches but the diode Schottky SMS 7630 had an important role in the map.

Table 1-5 Main parameters of most popular Schottky diodes [36]

Code of diode	HSMS-285x	HSMS-286x	SMS-7621	SMS-7630
V_{Br} (V)	3.8	7	3	2
C_j (pF)	0.18	0.18	0.1	0.14
V_T (mV) for 1 mA	250	350	260	135
R_s (Ω)	25	5	12	20

However, existing Schottky and CMOS devices are limited by the junction nonlinearity and the conversion efficiency is reduced to only a few percent at nW level. The magnetic tunnel junctions (MTJs) or spin diode was then analyzed in [34] with much smaller series resistance, junction capacitance as well as zero-bias junction resistance. This device, therefore, is a promising choice for low power energy harvesting apart from the traditional Schottky diode. In a companion work to this one, a specific rectenna is fabricated for intentional wireless energy transmission [36]. In

fact, the received energy is not different in order of magnitude from ambient energy levels considered here. Most popular Schottky diodes have been analyzed and main parameters are reported in Table 1-5.

b. *Circuit topologies choices*

The microwave rectifying circuit may adopt different topologies depending on incident power and frequency and as a function of position and number of diodes in the circuit. Among the most common topologies are:

- Single series half-wave rectifier topology: this is the simplest topology and it can be used in the very low input power circuit. The drawback of this topology is the low output voltage.
- Single shunt half-wave rectifier topology: this topology is similar to the single series one and also adapted with very low power application.
- Voltage multipliers topologies: in order to boost the output voltage, a number of voltage multiplier topologies have been reported in the literature [37]:
 - o Voltage doubler
 - o Crockcroft Walton/Greinacher/Villard charge pump
 - o Dickson charge pump
 - o Modified Cockcroft-Walton/Greinacher charge pump
 - o Mandal-Sarpeshkar voltage multiplier

The voltage multipliers topologies help to increase the output voltage and in the high-power circuit, they can achieve fair efficiency values. However, with the very low incident power, the input voltage is very low compared to the voltage across the diode and the diode bridge-based rectification becomes very inefficient [37]. The more the diode is involved in the circuit, the more losses appear. Therefore, in the low-power circuit of ambient RF energy harvesting, the single series or shunt topologies are preferred.

A Rectifier Figure of Merit (RFoM) can be defined as the product between open-circuit DC output voltage and the efficiency when the rectifier reaches its maximum power point (optimal load) (1-1).

$$RFoM_{Pin} = V_{DC \text{ open circuit}} \times \eta_{optimal \ load} \tag{1-1}$$

Authors in [6] have simulated four circuits to evaluate the RFoM of each topology. The results (Fig. 1-4) show that the single series diode topology offers a better trade-off in low power region below -5 dBm.

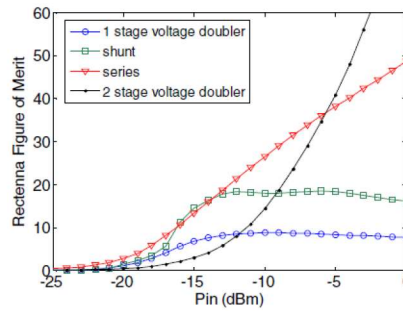


Fig. 1-4 Simulation of Rectifier Figure of Merit of different topologies versus input power[6]

c. Harmonic termination techniques

Typically, the rectifier is optimized to have impedance matching with the antenna at the fundamental frequency. In a microwave rectifier, the nonlinear diode also generates current and voltage at the harmonics of the operating frequency [38]. As described in Fig. 1-2, as the incident voltage continues to increase, the energy lost in harmonics further increase. Therefore, the efficiency of the rectifier can be improved by terminating its harmonic component across the diode.

The choice of harmonic termination technique is based on series resistance R_S and reverse breakdown voltage V_{Br} . Table 1-6 shows most suitable rectification mode versus R_S and V_{Br} , but as the input RF decreases, each class begins to operate with approximately the same efficiency [39]. Furthermore, the most realistic diode is the diode with high R_S and low V_{Br} , which is most suitable for Class-F harmonic termination.

Table 1-6 Most suitable rectification mode versus R_S and V_{Br} [39]

	High R_S	Low R_S
Low V_{Br}	Class-F	Inverse Class-E
High V_{Br}	Class-E	Inverse Class-F

Class-F harmonic termination presents the diode with zero impedance at even harmonics and infinite impedance at odd harmonics, what will reshape the diode voltage and current waveforms. An ideal Class-F rectifier is presented in Fig. 1-5. This rectifier uses ideal RF choke, ideal DC block, lossless transmission line; the input impedance is a conjugated match with the source impedance (antenna impedance in case of RF energy harvesting) [40].

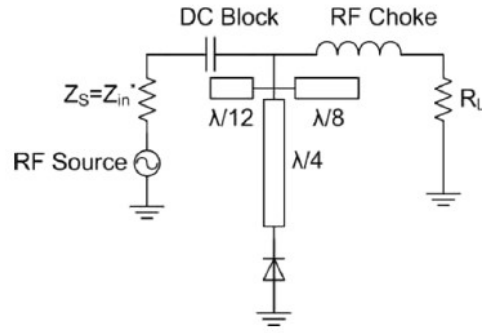


Fig. 1-5 Ideal Class-F rectifier topology used in circuit design [40]

Authors in [41] proposed a compact Class-F RF-DC converter at 2.45 GHz. The harmonic power dissipations are eliminated by open and short terminations for the odd and the even harmonics, respectively. The proposed circuit consists of an impedance matching network and a third-harmonic rejection filter (Fig. 1-6). The results show that this circuit also realized short termination for the second and the fourth harmonic (Fig. 1-7). Authors in [42] proposed a similar work that has an inverse Class-F rectifier, which operates at short terminations for the odd harmonic and open for even harmonic.

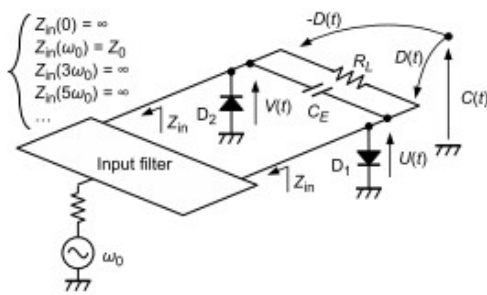


Fig. 1-6 Schematic of the proposed circuit in [41]

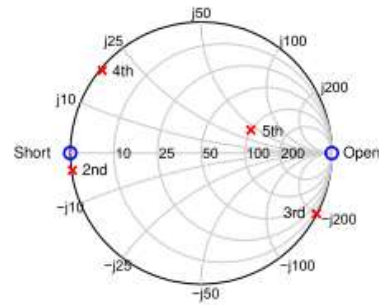


Fig. 1-7 Harmonic termination of each diode [41]

d. Impedance matching

The choice of interface impedance between the antenna and the rectifier plays a crucial role in maximizing the power conversion efficiency of rectenna systems. The interface between antenna and rectifier circuit is shown in Fig. 1-8 [43].

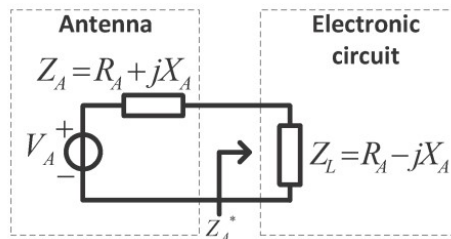


Fig. 1-8 Antenna-rectifier circuit interface [43]

Typically, the induced voltage from antenna V_A is very low due to the low power in the ambient and this input voltage amplitude is not greater than the threshold voltage V_{th} of the nonlinear component. For some applications, a very low start-up voltage of the rectifier is more important than the power conversion efficiency and in that condition, the impedance matching between the antenna and the rectifier in its cold-start is not desirable, hence the input RF filter, i.e. matching network, is not considered [44] [45].

However, when the antenna is not matched to the rectifier, the input voltage of rectifier is identical to the input voltage for the matched situation times a multiplicative factor. This factor is equal to 1 in the matched situation and smaller than 1 in other cases [46]. So in order to maximize the input voltage and power transfer, the interface should be impedance matched. Discussion about matching or not matching has been considered and it seems that there are more limitations than advantages to consider an unmatched scheme [47].

This does not implicate that 50- Ω is the best reference impedance with respect to harvesting. Unfortunately, the majority of antenna interfaces are 50- Ω due to the historical development of coaxial cable using in the experimental environment. A characteristic impedance of 50- Ω is a compromise between power handling and signal loss in high power radio waves [47]. Therefore, great deals of reported rectenna in literature have been developed with 50 Ω interfaces.

On the other hand, the design consists of an antenna having an input impedance that is complex conjugate with the rectifier input impedance was proposed to increase the performance of the rectenna. This means the antenna has a low resistive part and high inductance, which make the antenna electrically small [48]. A comparison between the 50- Ω interface and complex conjugate interfaces were performed and presented in Fig. 1-9 and Fig. 1-10 [48]. The result shows that the compact antenna with conjugated matching has about 5% higher in efficiency and this difference due to the loss in the matching circuit.



Fig. 1-9 Prototyped rectenna (a) 50- Ω matched; (b) complex conjugately matched [48]

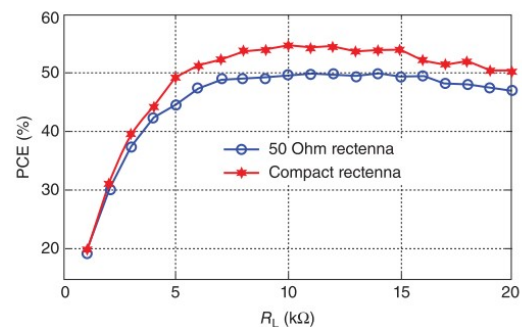


Fig. 1-10 Power conversion efficiency (PCE) of the rectennas show in Fig. 1-9 as a function of R_L , at $f=868$ MHz and $P_{in}=-10$ dBm.[48]

1.2.2 Techniques to increase the harvested power

a. *Combining techniques*

Harvested power from a single rectenna is mostly not sufficient in supplying energy for typical device operation. In order to build up the harvested power that can be suitable to supply low-power devices, techniques of combining several elements into one system are developed.

Combining single-frequency rectenna:

This direction concentrates in boosting the harvested power from RF sources at only one frequency. In the environment when only one mobile service is available, this technique is more productive. The most common practice is using multiple antennas arranged in a large array to produce a large amount of power. There are two most commonly used configurations [49]:

- RF-combiner: in which multiple antennas associated with an RF combiner and then connected with a rectifier. This array antenna works together as a single antenna with higher gain in order to increase the received power at the input of rectifier.
- DC-combiner: in which each antenna associated with its own rectifier and DC power then combined in parallel, series or hybrid. Besides, the DC-combiner can also be realized from two port of a single circular polarization antenna.

Combining multi-frequency rectenna:

This is an attractive approach since several RF sources exist in the ambiance from mobile services, especially in the urban and semi-urban environment. This trend has given rise to a lot of publications on the topic. However, due to the nonlinearities of the diode, the input impedance of the circuit varies as a function of the frequency, input power level, and load impedance. This creates a challenge for impedance matching of multi-frequency rectennas.

The multi-frequency solutions for RF energy harvesting include different approaches of rectenna (rectifier + antenna) architectures as described in Fig. 1-11.

- (I): Using different structures of single-band antenna and single-band rectifier side-by-side to form a multi-frequency rectenna
- (II): Using multiband or wideband antenna
 - o (II.1): Design multi-band antenna with different excitation points for different frequencies. The single-band rectifiers are used then to connect with each port of the multiband antenna.
 - o (II.2): Design consists of multi-band antenna connected to single-band rectifiers by adding multiplexers in between.

- (II.3): Design consists of reconfigurable frequency antennas, corresponding to each frequency band, and connected directly to multi-tone rectifiers.
- (II.4): Design consists of a multi-band antenna and a multi-tone rectifier.

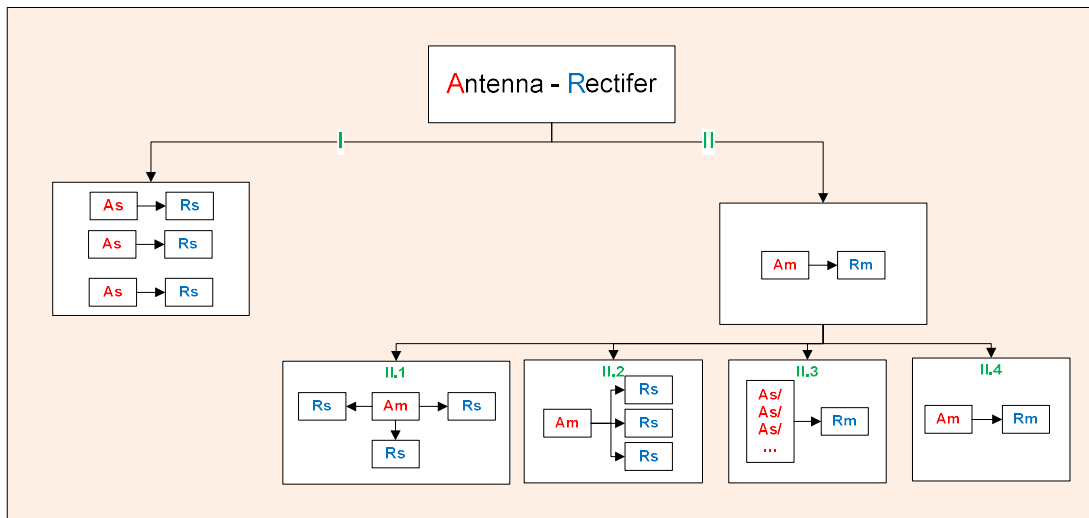


Fig. 1-11 Structures of multi-frequency solutions for RF energy harvesting

In the current literature, only the solutions I, II.2 and II.4 were proposed due to the complexity in the design of multiport antenna and reconfigurable frequency antenna.

Below are given some details about each technique and the results that have been reported.

b. Single-frequency: Multiple antennas in RF-combiner configuration

While using multiple antennas in an RF-combiner configuration, the phase of the incident wave is taken into account. This phased array of antenna offers to steer the beam in the desired direction. This topology has the advantage of harvesting more power near the main beam of the incident waves.

Mavaddat *et al.* proposed in [50] a 4x4 microstrip patch antenna array for millimeter-wave energy harvesting (Fig. 1-12). A step-impedance low-pass filter is used between the antenna and rectifier to suppress second-order harmonics generated by the diode. A GaAs Schottky diode MAE1317 was used in shunt topology as a half-wave rectifier. The antenna array has a gain of 19 dBi and the maximum RF-to-DC conversion efficiency was 67% at 35.7 GHz with an input power of 7mW.

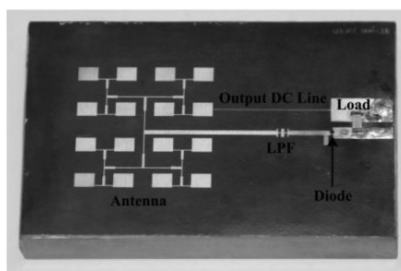


Fig. 1-12 Photo of the fabricated rectenna array in RF-combiner configuration [50]

c. **Single-frequency: Multiple antennas in DC-combiner configuration**

In the DC-combiner configuration, the rectifier received RF signal of each antenna prior to combining it at DC output. Each rectifier responds to the broader pattern of each antenna and therefore is less sensitive to the incidence angles.

Olgun *et al.* presented in [51] a 3x3 planar array of the simple Koch-type patch antenna and 3x3 rectifiers built-in directly in the lower layer of the substrate (Fig. 1-13). The rectifier is a single-stage full wave Greinacher rectifier and was optimized for the input power between -40 dBm to -20 dBm (Fig. 1-14).

The rectifier array was then combined by the series-connected array. This design has the advantage that the matched load is higher than the parallel topology and matches with the impedance of the energy management unit. The array setting also took into account the DC lines from each rectifier. In order to step-up and regulate the output voltage from the harvester circuit, the energy management units used the charge pump integrated circuit S882 and step-up DC-DC converter AS1310. When tested in the typical office environment, the device was able to supply a continuous current of 10 μA to the load. The maximum output current reached 50 μA . The total load varies between 85 and 105 k Ω , therefore the harvested power is about 10.5 μW .

Suffice to recall that a simple core microcontroller like STM32 by STMicroelectronics in its low-power configuration has current consumption under 1 μA that is equivalent to a resistor of 30 k Ω in standby mode [52]. Other way said, 1 μA is a non-negligible current with looking for digital computation.

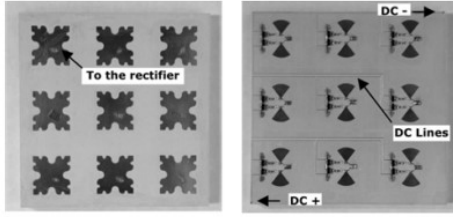


Fig. 1-13 Picture of the fabricated RF power harvester: Antenna array and rectifier array [51]

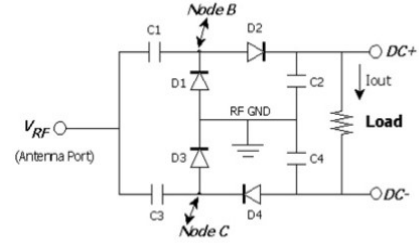


Fig. 1-14 Schematic of the rectifier in DC-combiner configuration [51]

Ferreira et al. in [53] also proposed a 4x3 rectenna array that has the same principle except that the rectifiers were combined in a parallel topology to maximize the output current. This prototype was able to power a 56 mW LED at a 2-Hz rate with the incident power of -10 dBm.

The effectiveness of the two configurations RF-combiner and DC-combiner depend on the number of antennas in the array and RF-to-DC conversion efficiency of the rectifier. The more antennas involved in the array, the better the DC-combiner configuration performs. The more the RF-to-DC conversion efficiency, the better the RF-combiner configuration effectiveness [49]. With similar characteristics of both antenna and rectifier, the RF-combiner has narrower beam width than the DC-combiner, but at the direction normal to the main beam, its performance is better.

d. **Single-frequency: Multi-input of an antenna in DC-combiner configuration**

Another way to combine energy from different polarization is connecting the rectifier with two excitation point of a square aperture-coupled patch antenna with dual linear antenna [54]. The antenna has the measured gain of 7.7 dBi for both polarizations. The RF-to-DC efficiency was 15.3% at vertical polarization and 11.3% for horizontal polarization.

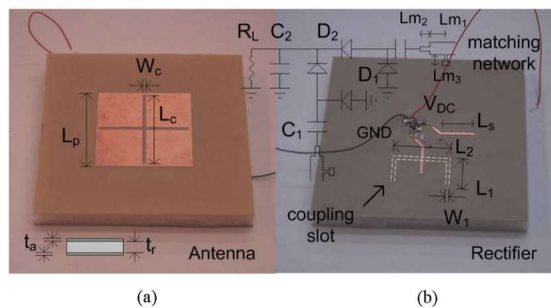


Fig. 1-15(a) Top view of radiating patch; (b) Bottom view of rectifier circuit [54]

The two voltage doublers were connected to two orthogonal polarization inputs (Fig. 1-15). The circuit has a maximum efficiency of 32.5% at an input power of 1.5 $\mu\text{W}/\text{cm}^2$ at 2.43 GHz. This design allows harvesting power regardless the input signal polarization.

e. **Multi-frequency: Multiple single-band antennas and single-tone rectifiers**

The structure of multiple single-band antenna and single-band rectifiers has been used to implement efficient ambient RF energy harvesters from different available bands in ambience.

Pinuela *et al.* have presented multiple rectenna structures with individual and shared power management modules (PMMs) in [55]. This structure consists of four wire antennas operated at a frequency of GSM 900 MHz, GSM 1800 MHz, 3G 2100 MHz and DTV from 470 MHz to 610 MHz. Powers from all signals are then combined in parallel array architectures.

A linear polarized folded dipole was selected in order to have an omnidirectional pattern and to avoid the need for beam pointing since the location of source stays unknown (Fig. 1-16).

The antennas were not integrated onto the substrate to embed the harvester into surrounded environments (furniture, windows, etc.). These wire antennas have the gain around 4.35 dBi and bandwidth of 5% around a central frequency. The unwanted coupling between single-band antennas was minimized by placing them apart of a distance of $\lambda_L/5$ (where λ_L is the wavelength of the lowest frequency band antenna).

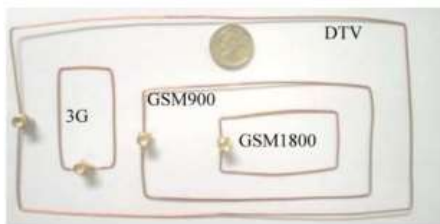


Fig. 1-16 DTV, GSM 900, GSM 1800 and 3G copper wire antennas [55]

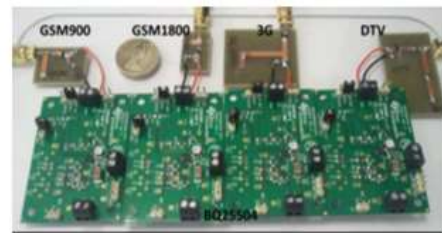


Fig. 1-17 Rectennas array architecture with individual PMMs [55]

The rectifier was designed by using the zero-bias SMS7630 diode in a series configuration. The impedance matching network used a series lumped-element inductor to absorb the capacitive reactance from the series diode and a $\lambda/4$ short-circuit shunt stub to achieve the 50- Ω impedance of input antennas. The optimal output load resistance was chosen for an RF input level of -20 dBm.

The low-power integrated circuit PMM from Texas Instruments Inc. (BQ25504) was integrated for maximum power point tracking. In this research, two different architectures were investigated, one with a single shared PMM (Fig. 1-17) and the second with multiple PMMs.

In the structure with share PMMs, the outputs of multiple rectenna were connected in series to increase the probability of the voltage at the input of PMM for reaching the cold-start level. The efficiency using shared PMMs is 15% with a combined input RF power of -12 dBm. The multiple rectenna with individual PMMs used a parallel topology to have the advantage of running each rectenna at its maximum power point. The efficiency using individual PMMs is 13% at an input power of -12 dBm. Both structures have lower efficiency compared to a single-band harvester but

the output power level is higher. The volumetric output DC power density is something like $7.4 \mu\text{W}/\text{cm}^3$. It is not so bad when referring to Table 1-1.

f. **Multi-frequency: Wideband/Multiband antenna and single-tone rectifiers**

The broadband rectenna has the advantage of collecting energy efficiently at any frequency regardless of the number of RF signals in the targeted bandwidth. However, the rectifier is a nonlinear circuit and its input impedance and efficiency indeed depend on input power level and frequency. Therefore, this kind of rectenna usually results in a very low efficiency in any particular frequency because of the quality of the impedance match between the antenna and a single rectifier. This efficiency is also reduced when increasing the bandwidth.

In the multiband rectenna, the available multi-frequency sources require a multiplexer circuit to separate energy between frequencies before entering the rectifier circuit, as it is better to use a specific rectifier for each frequency band. To ensure good performance of the system energy recovery, multi-frequency antennas are preferable to a multi-antenna system, because it is quite difficult to integrate several antennas in a small footprint while keeping good isolation between them. Two types of antennas may be used, wideband antenna or multi-band antenna that cover all the selected frequencies.

Kuhn *et al.* in [56] presented an architecture of multiband rectenna. Each RF branch consists of an impedance matching network, a rectifier and a DC filter. A number of branches is not limited and one wideband or multiband antenna is connected to the input of the circuit (Fig. 1-18).

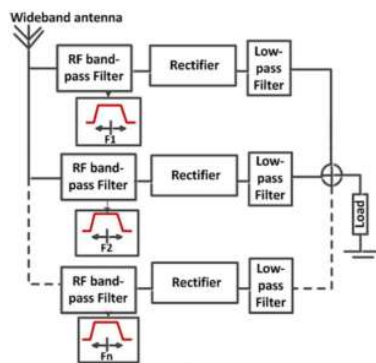


Fig. 1-18 Multiband rectenna with wideband antenna and multiple single-tone rectifiers [56]

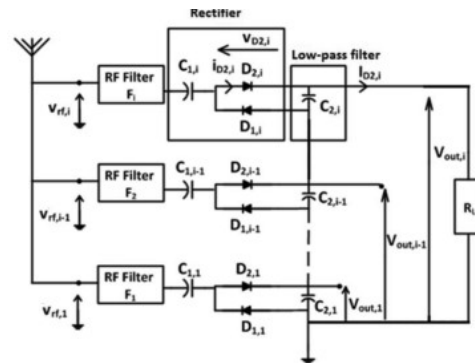


Fig. 1-19 Multiband RF harvester schematic [56]

This architecture allows obtaining a more compact circuit. However, there is a challenge to impedance matching. Each branch has a band-pass filter to match each rectifier with a selected frequency. The rectifier component is diode MSS20-41, which was chosen because of its higher efficiency and low power capability compared to the diode SMS7630. The rectifier was a modified voltage doubler structure whereof the connection to the ground was suppressed in order to create a differential output. The single-tone rectifiers were then connected in series. This structure allows

preventing DC interferences between the RF branches (Fig. 1-19). The harvester is connected with a wideband dipole antenna with a reflector plane. The gain of the antenna was 6 dBi throughout the band from 0.9 to 3 GHz.

The measurement in controlled environment showed an RF-to-DC conversion efficiency of 15% for an input power of -20 dBm. The rectenna was also measured in outdoor conditions and the DC power reached 15 μ W at MPP (maximum power point).

Song *et al.* present a similar work with six-band dual circular polarization rectenna [57]. Each rectifier branch was optimized for the two-separated band. The broadband log-periodic cross dipole was proposed with the gain of 2.5 to 5 dBi over the entire band. The RF-to-DC conversion efficiency of the structure is 11% at -30 dBm and measured harvested DC power in outdoor ambience reaches 96 μ W at MPP.

g. Multi-frequency: Wideband/Multiband antenna and multi-tone rectifier

Another approach to harvest ambient RF energy is to harvest simultaneously RF energy from several spectral bands. In this case, the multitone rectifying circuit is proposed [58], [59]. Liu *et al.* proposed a dual-band rectifier in simultaneous mode [59]. The rectifier consists of a zero-bias Schottky diode HSMS2850 and a GaAs pHEMT ATF34143 in order to have a low threshold voltage and high reverse breakdown (Fig. 1-20). This design allows extending the operating power range of the rectifier. This work has achieved an RF-to-DC conversion efficiency of 20% at -20 dBm.

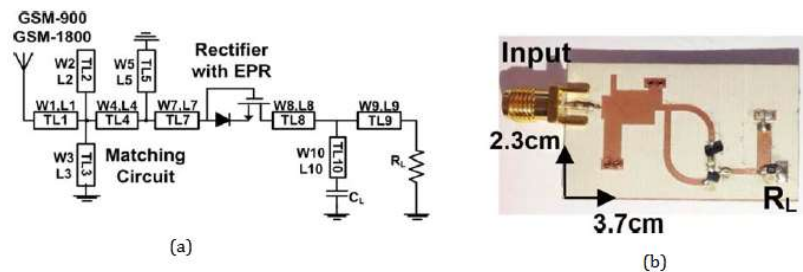


Fig. 1-20 Schematic (a) and fabricated circuit (b) of the multitone rectifier with EPR [59]

Table 1-7 compares the state-of-the-art designs of combining rectenna systems, considering only the works dedicated to ambient sources of very low power density.

Table 1-7 References of combining rectenna design

Design	Number of rectifier	Antenna	Size	Operating frequency (GHz)	Antenna gain (dBi)	RF-DC conversion Efficiency	Harvested power
[50]	1	16 x patch	Rectenna: 22 x 42 mm ²	35.7	19	67% at 7 mW (8.45 dBm)	
[51]	9	9 x Koch fractal patch	Rectenna: 90 x 90 x 10 mm ³	2.4	4.5	4.5% at -35 dBm	50 μ A at indoor ambient (10.5 μ W)
[55]	4	4 x folded dipoles		0.5; 0.9; 1.8; 2.1	4.48-4.76	15% at -12 dBm Single-tone: 40% at -15 dBm	
[56]	4	1 x wideband dipole with reflector plane	Antenna: 100 x 100 mm ²	0.9; 1.8; 2.1; 2.4	6	15% at -20 dBm	15 μ W at outdoor ambient
[57]	3	1 x log periodic cross dipole	Antenna: 160 x 160 mm ²	0.55; 0.75; 0.9; 1.85; 2.15; 2.45	2.5-4	11% at -30 dBm 30% at -20 dBm	96 μ W at outdoor ambient
[59]	1	-	23 x 37 mm ²	0.915; 1.8	-	20% at -20 dBm	-

1.3 Flexible antenna in energy harvesting system

1.3.1 Antenna using flexible material

There is a variety of flexible materials usable in antenna design such as textile material, paper-based material, polymer-based material. The properties of the material have an important influence on the behavior of the antenna. In general, the dielectric properties of a material depend on the frequency, temperature, and surface roughness. Bandwidth and efficiency of planar microstrip antenna mainly determined by permittivity and thickness of the material [60]. In addition, the conductivity is an important factor in the efficiency of the antenna.

a. *Textile material*

Textile presents a very low dielectric constant, the presence of air gives a relative permittivity close to one [60] therefore reducing surface wave losses and increasing the impedance and the bandwidth of the antenna. However, textiles material constantly exchanges water molecules with the environment, which affects their electromagnetic properties. When water is absorbed by textile fibers or trapped in the fabric structure, the permittivity and loss tangent of the textile increase.

Textile antennas are mainly planar antennas, specifically microstrip patch antennas, in which the propagation direction is normal to the antenna. In addition, the ground plane shields the effect of the human body [61]. The advantages of the electronic textile are essentially the physical flexibility and the ease of integration in wearable application [62].

Authors in [63] proposed to use the silver-plated knitted fabric and silver-copper-nickel woven fabric possessing a sheet resistance less than $1 \Omega/\text{sq}$ to keep the losses to a minimum. The patch antenna was characterized under bending condition until 37.5 mm of radius (Fig. 1-21). The realized gain is 4.4 dBi and the efficiency is 34.7%.

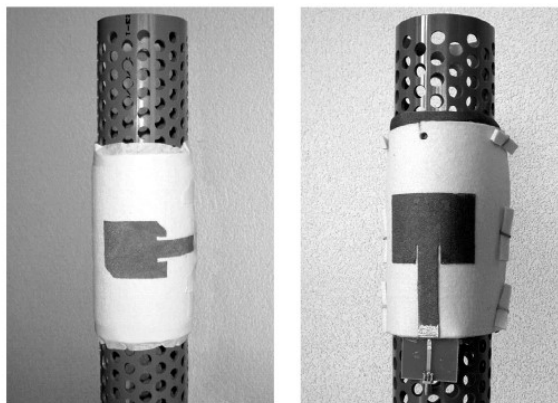


Fig. 1-21 Antenna bent around bending gauge with 75 mm diameter [63]

The washable antenna was also proposed with a breathable thermoplastic polyurethane coating to protect antenna against water absorption and corrosion [64]. However, due to the high-loss substrate, this type of antenna has low radiation efficiency, about 20-49%. The asymmetric meandered flare (AMF) dipole antenna based on the conductive Ag-coated Zylon fibers (E-fibers) was proposed in [65] in order to achieve higher radiation efficiency but the antenna gain stays low about 2 dBi (Fig. 1-22).



Fig. 1-22 Embroidered textile AMF antenna on organza fabric [65]

In order to increase the realized gain of the system, the patch antenna array based on polyurethane protective foam substrate (Azzurri) typically used in firefighters jackets was proposed [66].

b. Paper-based and polymer-based material

Flexible antenna using paper-based and the polymer-based substrate were profusely introduced such as silver nanoparticle ink printed on Kapton polyimide film, ceramic-polymer and carbon-epoxy composites, conductive polymers such as PEDOT or polypyrrole (PPy), metamaterial based artificial magnetic conductor structures [67].

A study compared two antennas based on two types of conductive polymers with different thickness and conductivities PEDOT and PPy using Ultralam 2000 substrate were presented in [68]. The results show that with thicker thickness (158 μm over 7 μm), the antenna has a much higher efficiency (80% over 2.6.6%).

To take advantage of the flexibility property, a different way of folding the antenna patch using Kapton substrate was designed and tested [69]. The proposed antenna is more tolerant to folding than its conventional patch counterpart, with a smaller variation of the resonant frequency and the gain over the different way of folding.

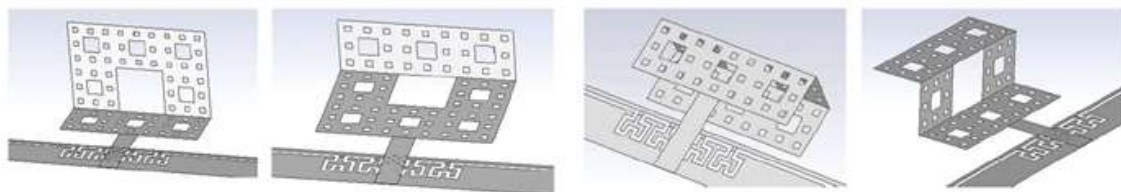


Fig. 1-23 Different way of folding antenna [69]

Embedded antennas for medical wireless communication systems can also make use of the flexible material to roll up inside an ingestible wireless capsule, which serves the diagnosis process.

A 50 μm thickness flexible substrate AP8525 from DuPont Pyralux was used to design a short-circuited Stepped Impedance Resonator (SIR) antenna [70]. This antenna has achieved a compact size of $18 \times 5.4 \text{ mm}^2$ at frequency 434 MHz (Fig. 1-24). However, the realized gain is very low, about -33 dBm.

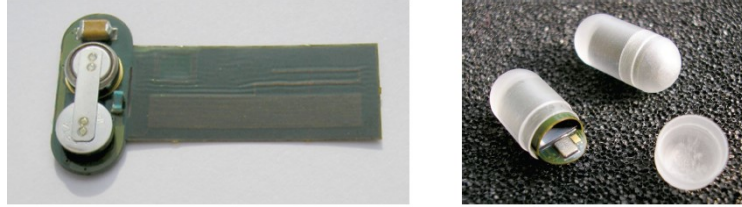


Fig. 1-24 Structure of the conformal antenna ingestible wireless capsule [70]

Inkjet printing technology is also a promising technique for flexible antenna due to the low-cost fabrication, capability of using a wide range of flexible material and eco-friendly. Numerous antennas were developed and characterized using this technology [71]–[75].

1.3.2 Techniques to increase realized gain of flexible antenna

Besides the advantages of the flexible substrate in antenna designing for a dedicated application, there are also the inconvenient comes from the characteristic of this type of substrate such as high-loss, super thin thickness, dependence on the implanted object. In some applications, this leads to decrease the gain and radiation efficiency of the antenna or increase the antenna's size. Monopole-based and dipole-based antennas were usually used to overcome these difficulties but they have the omnidirectional pattern and therefore low gain about 2 dBi.

On that account, techniques to increase the realized gain of the flexible antenna were proposed. A UWB antenna based on a half circular disc monopole and a rectangular patch with two steps is designed and realized [72] to archive the gain of 4.2 dBi at 3 GHz.

Series-fed of two dipole antenna comprising a balun filter on liquid crystal polymer substrate was designed to be used at a frequency band of 26-33 GHz [71]. With the dipole-base structure, even the substrate thickness is only 0.1 mm, the maximal gain can reach 6.2 dBi without bending and 5.2 dBi after bending. However, the antenna's size is quite large, about $1.20 \lambda_0 \times 0.38 \lambda_0$.

Using the combination of 3D and 2D inkjet printing, the integration of a Fresnel lens to a helix antenna (Fig. 1-25), the antenna gain can enhance from 4.6 dBi to a peak gain of 12.9 dBi at 8.8 GHz [75]. The dielectric material used is a photosensitive polymer named VeroBlackPlus with a permittivity 2.6 and a high loss tangent of 0.023.

The directional-type antennas such as patch antenna, Vivaldi antenna, quasi-yagi uniplanar were also adapted to use in a planar structure in order to enhance the gain [76]–[78]. Authors in [76] proposed a Vivaldi antenna based on silicon foam substrate, with permittivity of 3.02 and loss

tangent of 0.04. This antenna achieved the gain of 3 to 7.6 dBi in the frequency range of 150 MHz to 900 MHz.

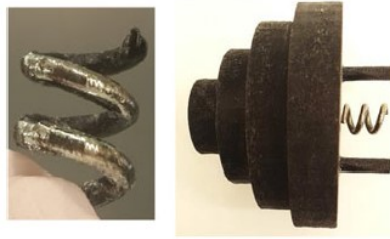


Fig. 1-25 Fabricated antenna with the integration of a Fresnel lens [75]

A very effective solution to use in the high-loss organic substrate such as paper is to use ground-backed frequency selective surfaces (FSSs) (as described in Fig. 1-26) for the artificial magnetic conductor (AMC) [79]. This technique allows increasing the gain by 5dB over the conventional structure.

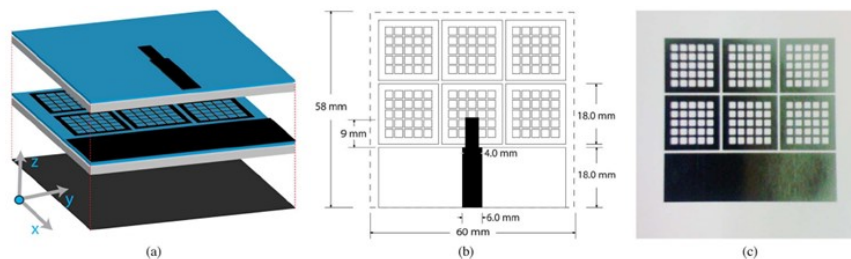


Fig. 1-26 Antenna with ground-backed FSSs design [79]

1.3.3 Integration of flexible antenna in energy harvesting system

Although being used a lot in designing an antenna, the integrated flexible antenna in energy harvesting system is not too common.

Authors in [80] proposed a wideband planar monopole antenna on cardboard for RF energy harvesting. This antenna has the maximum realized gain of 5 dBi but only 2 dBi at fundamental mode. Another dipole-like antenna was proposed for UHF RFID energy harvesting system based on Silicon-on-Insulator technology [81] and the modest gain is achieved about 1.85 dBi.

In order to integrate the rectifier circuit at the back of the antenna, a one-sided directional flexible antenna was designed with the gain of -0.7 dBi at 900 MHz. The flexible material used in this structure allows the whole system to bend and stick to the wall for ambient RF energy harvesting or wireless power transfer. Antennas for RF energy harvesting were also integrated with other solution such as solar harvester to increase the harvested power. In [82], a dual-band substrate integrated waveguide textile antenna was presented, the antenna has the gain of 4.7 dBi at 2.45 GHz. The structure has high robustness against bending, the low influence of human body and effectively exploited the surface area for integrated solar cell (Fig. 1-27). Similar hybrid

solar/RF harvester was proposed in [83] except that the antenna was a monopole with a realized gain of 0 dBi at 850 MHz (Fig. 1-28).

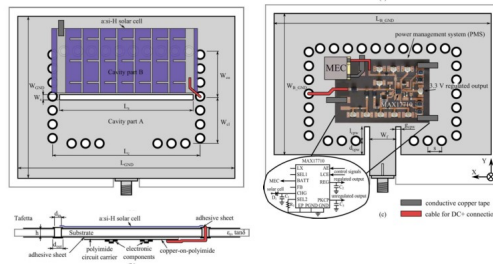


Fig. 1-27 Proposed SIW cavity-backed slot antenna with integrated solar harvester [82]

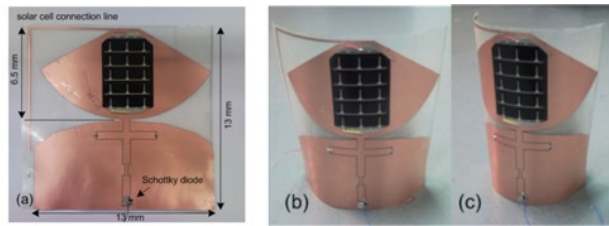


Fig. 1-28 Designed of hybrid solar/EM energy harvester in different bent radius [83]

The flexibility property can also be taken as an advantage for antennas in 3-D packaging (Fig. 1-29) [84]. In this application, the Parylene substrate has a very thin thickness down to 50 μm and the loss tangent is about 0.002. The miniature embedded loop antenna was proposed and the total size of receiver module on Parylene interposer is 6 mm x 3mm. However, the antenna gain is about -15 dBi at 4 GHz.

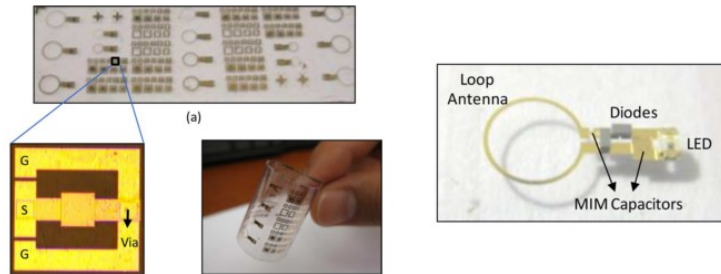


Fig. 1-29 Parylene interposer as thin flexible 3-D packaging enabler for wireless applications [84]

Table 1-8 presents the comparison of the several developed flexible antennas in current literature. From the point of view of antenna design, current flexible antenna designs for energy harvesting system are mainly suitable for the integration in hybrid systems on various thin and flexible substrates. However, the performance of the antenna is not quite high as the demand of the RF energy harvesting, especially the gain and radiation efficiency. Furthermore, the system packaging of a conventional electronic circuit such as rectangular box was not made use of. On the other hand, considering the need to combine multiple energy harvesting circuits to increase the harvested power, combining multiple antennas in one surface or area is also required to be analyzed and developed.

Table 1-8 Comparison of the flexible antennas in literature

Reference	Frequency GHz	Dielectric material				Conductive Material	Antenna	Size (λ_0^2)	Performance	
		Material	h_{sub} (mm)	ϵ_r	$\tan\delta$				Gain	Efficiency
[63]	2.4	Textile (Woolen felt)	3.5	1.45	0.02	Silver-copper-nickel plated woven fabric	Rectangular patch	0.46x0.39	4.4	34.7%
[65]	0.6					Conductive E-fiber 0.8 Ω /sq	Asymmetric meander flare dipole	0.49x0.49	2	
[64]	2.4	Cotton/Polyester	2.808	1.6	0.02	Flectron/Electrodag conductive ink 0.1 Ω /sq	Rectangular patch	0.54x0.35		49%
[66]	2.4	polyurethane protective foam	3.55	1.19	0.003	Flectron 0.01 Ω /sq	Triangular patch	3.93x1.475	10	
	0.434	polyimide film AP8525	0.05	3.4		Copper 18 μ m	Short-circuited SIR	0.02x0.007	8	-33
[68]	3.1-10.6	Ultralam 2000	1.5	2.5	0.0022	PEDOT: 7 μ m, 9 Ω /sq	Monopole	0.625x0.62	2	26.6%
[68]	3.1-10.6	Ultralam 2000	1.5	2.5	0.0022	PPy:158 μ m, 2.3 Ω /sq	Monopole		2	79.2%
[71]	26-33	Ultralam 3650	0.1	2.9-3.2	0.005	Silver nanoparticle	Series-fed two dipole	1.2x0.38	6.2	

[76]	0.15-0.9	Silicone foam	1.5	3.02	0.04	Adhesive e-textile	Vivaldi	0.3x0.3	3 to 7.6	
[77]	1.574	Rogers 5880	0.127	2.2	0.0009	copper	Quasi-yagi printed uniplanar	0.17 x0.43	5.76	
[78]	1.574	Rogers 5880	0.127	2.2	0.0009	copper	CPW-fed uniplanar	0.26x0.22	3.57	
[79]	5	Foam-backed paper	1.25	2.92	0.06	silver	3x2 array ground- backed FSSs	1x1	7	
[80]	0.6-1.5	Paper-based	0.56	1.78	0.025	Silver ink 3 μm ; $2e7$ S/m	Monopole		2-5	72%-80%
[82]	2.4; 2.6	Textile rubber protective foam	3.94	1.49 5	0.016	copper polyester Taffeta 0.18 Ω/sq	SIW cavity - backed slot	0.76x1.02	5	89%
[81]	0.8665	Paper-based					Dipole like			
[85]	0.83 0.9	-	1.27	10.2	0.0023	Copper 18 μm	One-sided directional slot	0.18x0.15	-0.7	
[86] [83]	0.8-6	PET Akaflex PCL	0.075	3.3	0.08	Copper 35 μm	CPW monopole	0.25x0.34	-1.83 to 0.24	
[84]	4	Parylene-C	0.05	3	0.0002	Metal 0.2 μm	Loop antenna	3x3	-15	

1.4 Conclusion

This chapter has reviewed reported solutions for ambient energy harvesting for low-power applications. A summary of ambient RF measurements as detailed in literature has been presented. From these results, the working frequencies are chosen.

As given in literature review, the ambient RF sources have very low power density. Hence in order to increase the overall efficiency and harvested power, combinations of antenna and rectifier are performed.

Table 1-7 compares the state-of-the-art designs of rectenna systems, several designs were tested in the realistic environment while most of them were measured with controlled sources and environment. These state-of-the-art informs of a lack of measurements in the realistic environment by sectorization of the incident waves [87]. Table 1-8 gives the overall comparison of flexible antennas in literature. This summary shows the limitation in the use of this type of antenna for RF energy harvesting.

Our goal is to design a rectenna suitable for demands of IoT applications. These antennas are expected to be fabricated on a flexible substrate and their forms allow them to be integrated as a background feature such as a circuit in packaging. It is necessary to consider the transition from the antenna to the rectifier in order to minimize the insertion loss of the overall system.

The measurements are expected in a realistic environment where multipath and reflections are taken into account in order to estimate the probability of energy harvesting at the receiving circuit.

2. Antenna

The antenna is a crucial element of RF energy harvesters, which has the role of receiving an electromagnetic wave in free space and delivering its power to the load. Therefore, the study of antenna that is suitable for energy harvesting system is necessary.

Antenna technology was the fundamental subject in electrical engineering and physical domain for centuries. For this reason, there was a great deal of developments and advancements of antenna's techniques in the literature and we will not present in this manuscript the principle and fundamental characteristic of an antenna but rather the development of antenna from the point of view of energy harvesting for IoT. The IoT devices, which can be represented by a network of wireless sensors, have the challenge of recovering the energy from an extremely low ambient field. In respect to the growing development of interconnected objects within the industry and domestic uses, the antenna in energy harvesting system, therefore, must also meet a requirement for flexibility for its future integration with an object and the electronics for energy storage and conversion.

Current flexible antennas developed in literature for energy harvesting (as presented in Chapter 1) are multiform and tend to integrate on hybrid energy harvesting system in considering other sources such as solar energy [82] [83]. Many techniques has been applied in antenna design on flexible substrate, such as dipole/monopole-based antenna [83][68][80][86][81], patch/microstrip antenna [63][64][66][79], Vivaldi antenna[76], quasi-Yagi antenna [77] and SIW cavity-backed slot antenna [82]. However, the performance of these antennas is not quite high as demand in term of gain and efficiency in regards their dimensions.

On account of the requirements, the specifications for the flexible antenna in RF energy harvesting system are discussed and several types of antenna that meet these requirements will be introduced. In this section, detailed simulation, fabrication and measurement of these antennas will be presented.

2.1 Requirements of antenna for ambient energy harvesting

As analyzed in Chapter 1, frequency bands that are suitable for RF ambient energy harvesting are the band of GSM900, GSM1800, UMTS2100, LTE2600 and Wi-Fi band 2.45 GHz. Therefore, the combination of all sources is necessary and normally multi-band and wideband antennas for mobile applications are preferred to use in this system. As mentioned in Chapter 1 (Fig1-11) about structures of multi-frequency solutions for RF energy harvesting, different approaches of rectenna structures were presented but not all of these solutions were developed in the literature. These

propositions aim to combine several sources in the ambient into one system. The solutions of the antenna can be used in the combinations ambient energy harvesting are:

- Using multiband/wideband antenna, connected with an independent rectifier or multi-tone rectifier.
- Using reconfigurable frequency antenna corresponds to each frequency band, which is available in the ambient.
- Using several single-band antennas at each frequency to form a multi-frequency system. This requires the design of multiple antennas at each frequency bands mentioned.
- Using several single-band antennas to form diversity antenna in space.

The analysis and proposition of each solution are presented below. In order to evaluate the performance of each design, their specifications will be defined in advance to guide the design.

The antenna gain and radiation characteristics play an important role in the system's ability to amplify the signal level. While harvesting from identified sources, a directional antenna is desired but while scavenging from unspecified sources, which is the case of ambient energy, an omnidirectional antenna is desired.

In the case of using multiple-antenna, the mutual coupling can induce interchange of energy between antennas. Amount of energy received by each antenna will be the vector sum of the incident waves and parasitic coupled waves from others [88]. The objective of the multiple-antenna design is minimizing the influence of this undesired coupling. This can be done by properly choosing the structure and terminating impedance of each antenna.

In the context of wireless network sensors, a compact and flexible system is also required. The system packaging of a conventional electronic circuit such as rectangular box will be made use of in order to immerse the antenna as a background feature. The conventional flexible substrate will be used in order to achieve the low cost and facilitate for mass production. However, this type of substrate has the characteristic of high-loss and complement technique is expected to overcome this loss and maintain the gain of the antenna.

2.2 3D flexible multi-band antenna

In present literature, there is a wide variety of multi-band antenna types for energy harvesting systems which have been studied [89]–[93]. However, these studies have been limited to two to three bands of the frequencies listed above. Further, most of their shapes are planar or 3-D which is not compatible with the requirement of IoT devices and can be too complex to integrate into different forms of the circuit or system packaging, such as a rectangular box.

To fix these shortcomings, two novel types of antenna are being developed in the present study. The aim is to create an antenna that covers a wider range of frequency bands and with a design that is more versatile thus easier to implement with various types of circuitry and modern sensors.

This section proposes two new compact 3-D multiband antennas that operate on three to five frequency bands (GSM, UMTS, and WLAN service). Study methodology, results of simulation and experimental data are included.

2.2.1 Dipole-based antenna

a. Antenna Configuration

The performance of current multi-band antennas is traditionally limited by the shape and arrangement of their radiating elements. A high number of the multi-band antennas published in the literature have correlated operating frequencies. Consequently, the relation between these frequencies is dependent and not easily controllable. Moreover, at the different operating frequencies, the radiation patterns of these antennas are often not very similar and difficult to modify.

Wireless communications antennas are generally developed as passive planar structures, which consist of a main radiating element, a support ground plane, a support substrate, and a feeding structure [94]. Nowadays, antennas for wireless devices are mainly built using planar printed technology. The multi-band operations can be realized by creating several radiators for different resonances of a single feeder or extending the physical length of the main radiator to achieve several resonance modes.

Due to the compact size and omnidirectional radiation pattern, a dipole antenna was used as a base design, which was modified in order to work with several frequencies simultaneously.

In order to scale down the antenna size and to use a 3-D form of the typical packaging, the planar dipole has been modified to form a U-dipole which length (including two sides) is half-wavelength. With this configuration, the equivalent antenna area for collecting energy remained unaffected but the size is more compact. The two resonant frequencies of fundamental and second mode at GSM band 1800 MHz and WLAN band 5 GHz (including 5.2 GHz and 5.8 GHz) were achieved.

Secondly, to attain another resonant frequency of Wi-Fi band at 2.4 GHz, a parasite element was placed near the first conductor to create the coupling between them.

The third conductor was added on the other side to obtain the impedance matching for the bandwidth between 1800 MHz and 2.4 GHz and to accommodate another operation frequency at

UMTS band 2.1 GHz. These two coupling conductors were essential components for the multi-band operation of the proposed antenna.

The configuration of the proposed 3-D dipole antenna is shown in Fig. 2-1 and the geometry of the antenna is presented in Fig. 2-2. The initial substrate used for this design is a Rogers 4003 with a thickness of 0.813 mm, a relative permittivity $\epsilon_r = 3.55$ and a loss tangent $\tan\delta = 0.0027$.

The two sides of the proposed antenna include shapes in different sizes aimed to affect the characteristic impedance of the antenna, therefore minimizing the reflection coefficient at design frequencies. The shape at feed point was designed as trapezoidal to match the input impedance of the antenna.

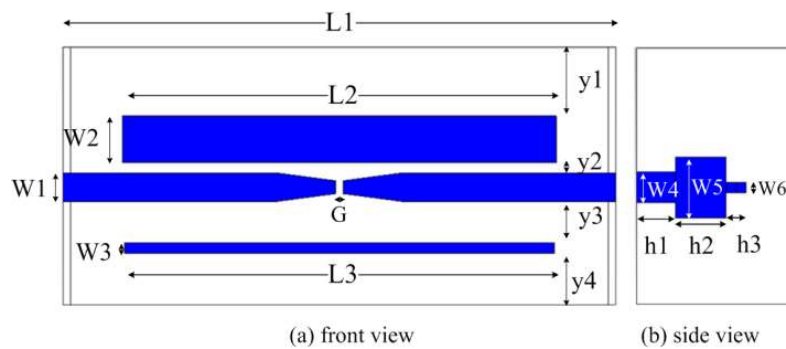


Fig. 2-1 Configuration of the proposed antenna

b. Simulation and measurement results

The transient Solver within CST Microwave Studio was used for simulation. The antenna was excited by a waveguide port of 50- Ω input impedance through a model of SMA connector.

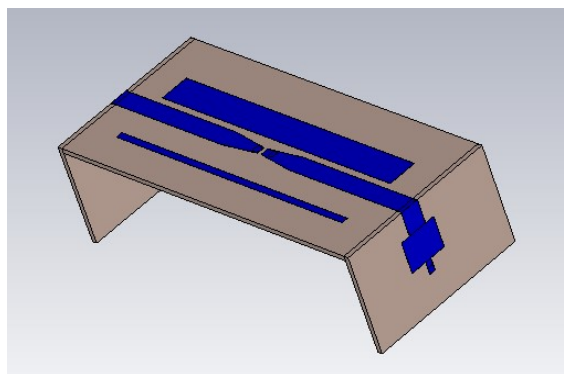


Fig. 2-2 3-D structure of the proposed antenna

The lengths of each conductor ($L1$, $L2$, $L3$, $h1$, $h2$, and $h3$) were optimized in order to obtain the resonance at targeted frequencies. Other parameters need to be optimized in order to minimize the reflection coefficient, such as the gap-feed dimension (g), the distance between conductors ($y1$, $y2$, $y3$, $y4$) and the widths of each element ($W1$, $W2$, $W3$, $W4$, $W5$, $W6$).

By considering all these characteristics, the design values for all parameters are obtained as given in Table 2-1. The total volume of the 3D-antenna under the geometry of the packaging box is $60 \times 25 \times 15 \text{ mm}^3$.

Table 2-1 Designed parameters of the proposed antenna

Symbol	Length (mm)	Symbol	Length (mm)	Symbol	Length (mm)
L1	54.8	Y1	5.7	W3	1
L2	43	Y2	1	W4	3
L3	42.6	Y3	5	W5	6
h1	3	Y4	5	W6	1
h2	5	W1	2.8	G	0.7
h3	2	W2	4.5		

The 3-D dipole antenna with optimal dimensions was then fabricated using RO4003 substrate. Fig. 2-3 presents a photo of the realized prototypes. The antenna was constructed by printing metal on one side of the substrate and thickness of metal is 0.017 mm. The conductor parts in two sides of the antenna were linked with the main part by two sections of metal tape.



Fig. 2-3 Fabricated 3-D antenna

The measurement of reflection coefficient was performed by using the Agilent Vector Network Analyzer (VNA) 8720ES over the frequency range 50 MHz-6 GHz.

Fig. 2-4 presents the simulated and measured reflection coefficient in dB of the proposed 3-D antenna. In a comparison between these results, we can notice good agreement at all resonant frequencies.

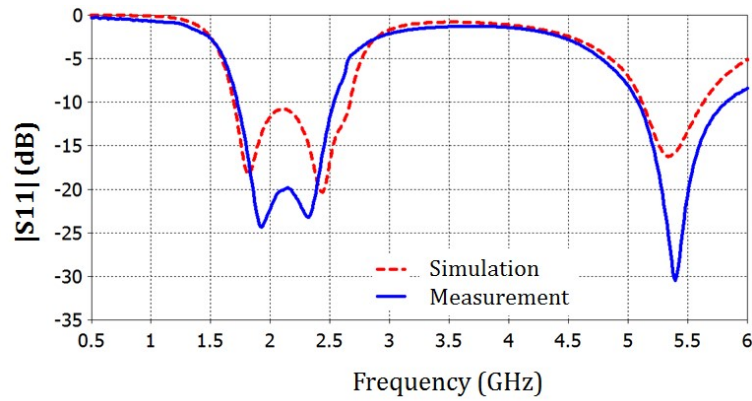


Fig. 2-4 Simulated (CST Time Domain) and measurement reflection coefficient of the proposed antenna

Table 2-2 shows the comparison of reflection coefficient between simulation and measurement. It can be seen that both results agree correctly except that the measured result exhibits better impedance matching, especially for the UMTS frequency 2100 MHz. This difference can be explained by the way of joining planes together in the fabrication process. This process can cause the discontinuity in the conductor and affect the impedance matching of the antenna.

Table 2-2 Comparison of reflection coefficient between simulation and measurement at targeted frequencies

S11(dB)	GSM 1800MHz	UMTS 2100MHz	Wi-Fi 2.45GHz	Wi-Fi 5.2GHz
Simulation	-18	-11	-20	-13
Measurement	-15	-20	-15	-15

The measured -10 dB impedance bandwidths are 810 MHz (1.72-2.53 GHz) at the first band and 750 MHz (5.07-5.82 GHz) at the second band. The bandwidths cover not only the GSM 1800 MHz band and UMTS 2100 MHz band but also all the 2.4 GHz WLAN channels (from 2.40 GHz to 2.48 GHz) and 5 GHz WLAN channels (from 5.1 GHz to 5.8 GHz).

Radiation characteristics of the proposed antenna were also studied. The simulated far-field pattern of the antenna at 1800MHz is shown in Fig. 2-5. The measurement of radiation pattern was performed in the anechoic chamber. The transmitting antenna is a Vivaldi horn antenna and its largest dimension is 22 cm. The proposed 3-D antenna was located at a distance of 3 m from the horn antenna so the far-field condition is ensured for all frequency bands. The coaxial feed cable is perpendicular to the plane of transmission (z-direction) in order to limit its influence on the measurement.

Fig. 2-6, Fig. 2-7, Fig. 2-8, Fig. 2-9 illustrate the simulated and measured radiation patterns of 2 planes $\varphi=0^\circ$ and $\varphi=90^\circ$ at resonant frequencies 1800 MHz, 2100 MHz, 2.45 GHz and 5.2 GHz, respectively.

The pattern of the antenna is omnidirectional at 1800 MHz, 2100 MHz, 2.45 GHz and directional at 5.2 GHz. There is a slightly different pattern in the direction of 180° between simulation and measurement. These differences were caused by the presence of the rotation motor in which the antenna was attached.

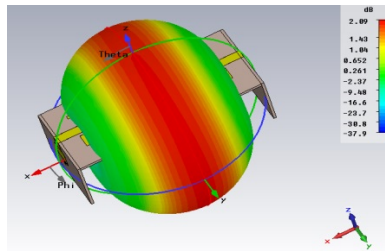


Fig. 2-5 Simulated far-field pattern of the antenna at 1800MHz

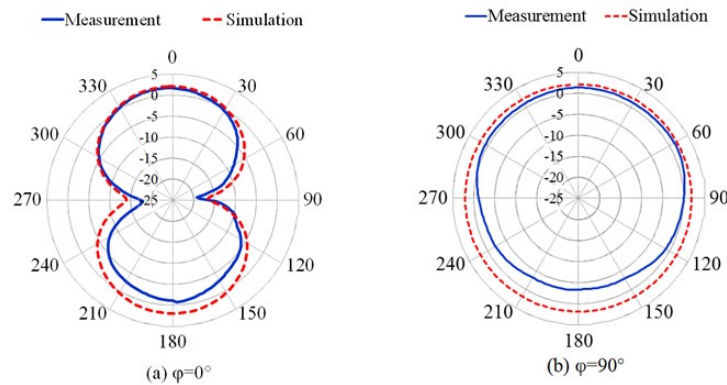


Fig. 2-6 Radiation Patterns of the antenna at GSM frequency (1800 MHz): (a) $\varphi = 0^\circ$ (b) $\varphi = 90^\circ$

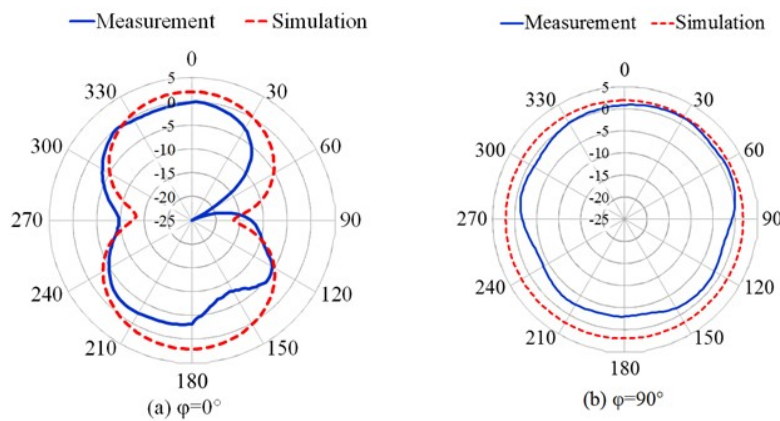


Fig. 2-7 Radiation Patterns of the antenna at UMTS frequency (2100 MHz) (a) $\varphi = 0^\circ$ (b) $\varphi = 90^\circ$

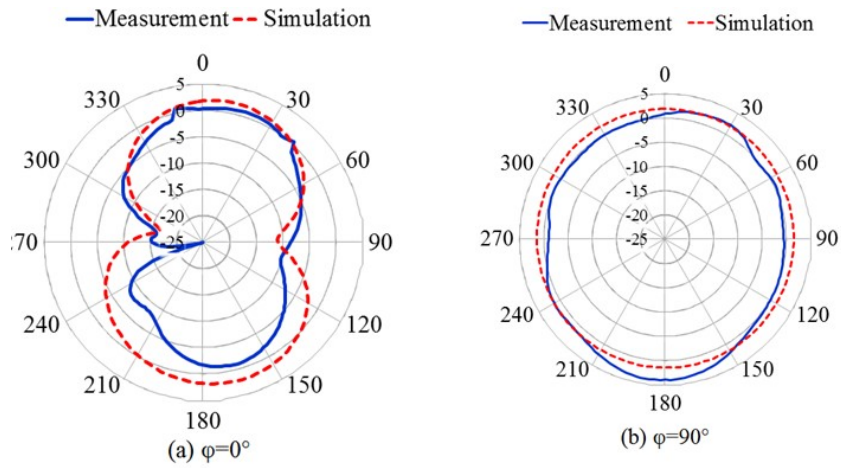


Fig. 2-8 Radiation Patterns of the antenna at Wi-Fi frequency 2.45 GHz: (a) $\varphi=0^\circ$ (b) $\varphi=90^\circ$

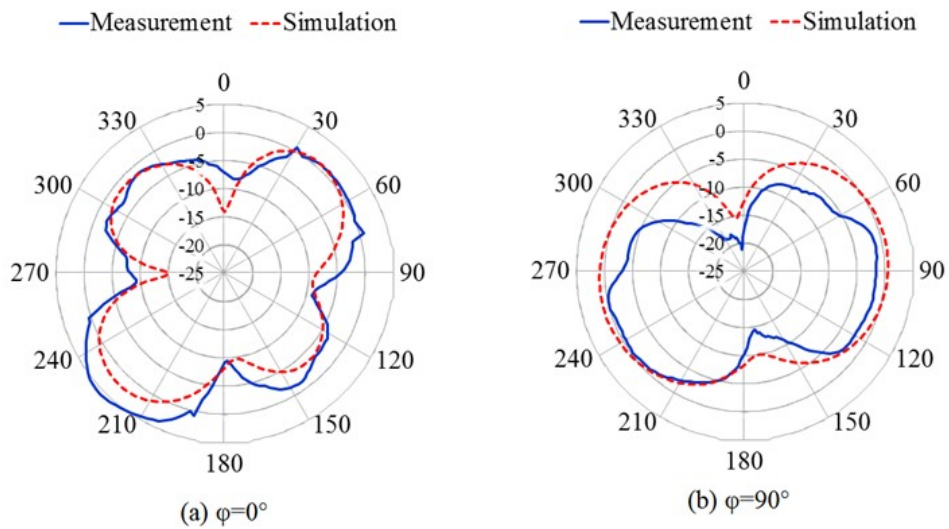


Fig. 2-9 Radiation Patterns of the antenna at Wi-Fi frequency 5.2 GHz: (a) $\varphi=0^\circ$ (b) $\varphi=90^\circ$

The performances of proposed antenna are presented in Table 2-3. The gain difference between simulation and measurement are about 0.5 dB because of the uncertainty on calibration process, metallic loss and additional loss of the connectors and cables during the fabrication and measurement. In the simulation, this antenna has a good efficiency at working frequencies, around 90%.

Table 2-3 Comparison of performances between simulation and measurement at targeted frequencies

Gain (dBi)	GSM 1800MHz	UMTS 2100MHz	Wi-Fi 2.45GHz	Wi-Fi 5.2GHz
Simulation	2.09	2.08	2.33	4.4
Measurement	1.66	1.62	2.7	5.84
Efficiency (simulation)	96%	87%	96%	96%

c. *Applying for printed antenna on flexible substrate*

The development of antenna design and electronic circuits using a paper substrate is increasing in popularity. Benefits include lightweight properties, which are flexible, economical in cost and eco-friendly. If used in RF energy harvesting application, a flexible substrate antenna can be implemented directly on system packaging, thus reducing overall size while enhancing the system performance.

The same design of dipole-based antenna above is applied on the flexible substrate to study the influence of the substrate and the flexible limitation of the structure. The flexible substrate used in this study is a standard commercial paper with a thickness of 0.23 mm. Screen printing technology is used to create an ink layer of a conductor made by silver nanoparticle with a thickness of 0.02 mm. The used substrate has a relative permittivity $\epsilon_r = 3.359$ and very high loss tangent $\tan\delta = 0.125$. The dimensions of the antenna, therefore, were adapted to the new substrate.

Because of the flexible feature, a unified piece of the antenna can be fabricated and then be folded in order to meet the requirement of packaging. The flat structure (Fig. 2-10) has many different folding possibilities corresponding to the box's specification. With this structure, the length and width of the box packaging are not limited to fixed dimensions. Instead of an immovable form of the first prototype, the antenna is possible to fit with various sizes and therefore can increase the applicability. The antenna has the planar size of $84 \times 25 \text{ mm}^2$.

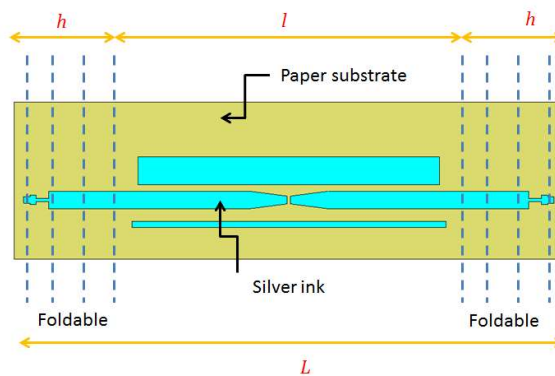


Fig. 2-10 Foldable structure of proposed paper antenna

After folding, the antenna has the sum of double the height (h) and the length (l) equal to the length (L) of the antenna as a planar state. A parametric sweep was conducted in order to define the limited value of these parameters while maintaining the performance of the antenna in term of impedance matching. Fig. 2-11 presents the reflection coefficient of the folded antenna at a different value of height and length. While folding at different positions, the resonant frequency is slightly shifting but the -10 dB impedance bandwidths at operational frequencies are still assured. The results show that the antenna can be suitable for packages having size between $76 \times 4 \times 25 \text{ mm}^3$ and $48 \times 18 \times 25 \text{ mm}^3$.

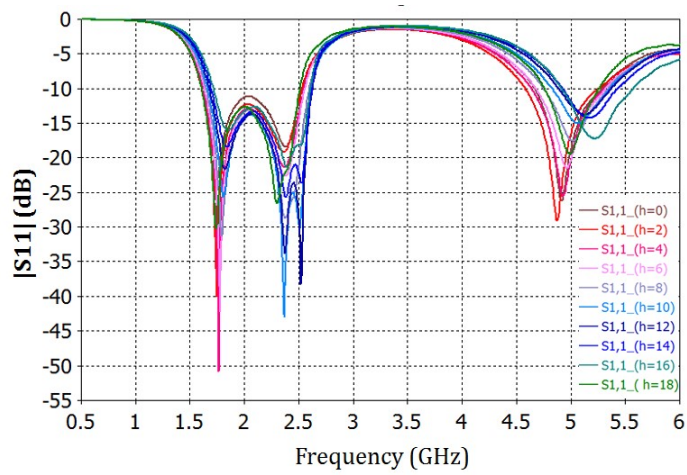


Fig. 2-11 Simulated reflection coefficient of 3D paper antenna at different values of h (mm)

In term of radiation characteristics, the paper antenna has the same radiation pattern as the Rogers prototype presented above. However, due to the high loss substrate, the gains of antenna across operational frequencies decrease as compare to the Rogers 4003 substrate. Table 2-4 shows the comparison between simulated gains of two prototypes.

Table 2-4 Comparison of simulated gain between two prototypes

Simulated gain (dBi)	GSM 1800MHz	UMTS 2100MHz	Wi-Fi 2.45GHz	Wi-Fi 5.2GHz
Rogers 4003 antenna	2.09	2.08	2.33	4.4
Paper antenna (flat)	1.74	1.33	1.1	3.35
Paper antenna (folded, $h=18$)	1.45	1.22	0.96	2.01

The antenna was then fabricated using screen-printing technology. Fig. 2-12 presents a photo of the realized prototype. Fig. 2-13 presents prototypes of the folded antenna with different heights.

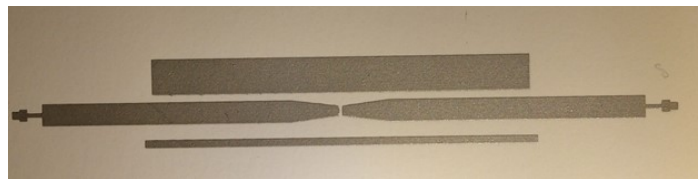


Fig. 2-12 Prototype of proposed paper antenna

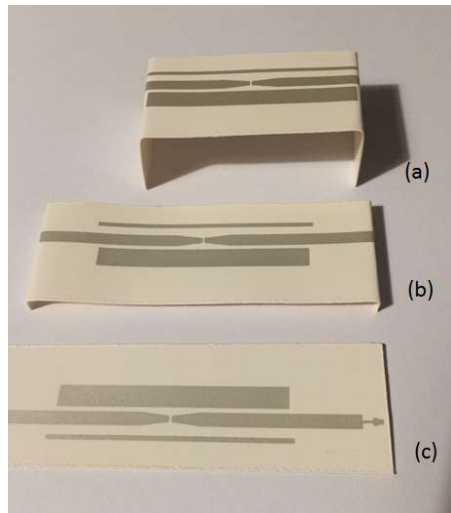


Fig. 2-13 Prototypes of folded paper antenna (a) $h=18$ mm; (b) $h=4$ mm; (c) $h=0$ mm (flat antenna)

Fig. 2-14 presents the simulated and measured reflection coefficient of the flat paper antenna. A good agreement can be noticed at all resonant frequencies.

This 3D flexible antenna has an advantage of structural simplicity and easy to conform to different forms of electronic system packaging. The radiation pattern is similar to the radiation pattern of the same structure on Rogers 4003 substrate. However, in term of gain, this antenna has slightly lower gain and therefore exhibits reduced performance of energy harvesting system.

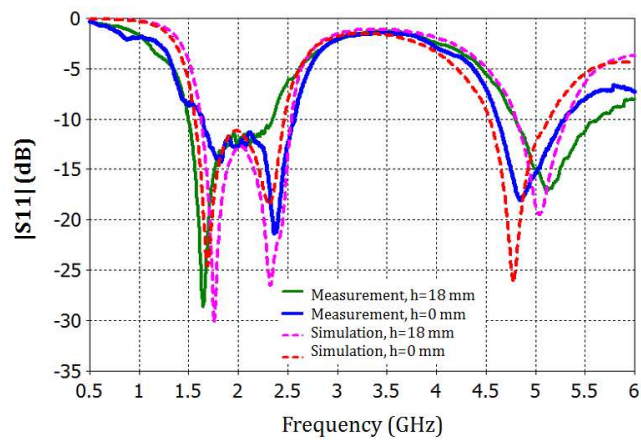


Fig. 2-14 Simulation and measurement reflection coefficient of the paper substrate antenna in flat and folded configuration ($h=0$ mm and $h=18$ mm)

2.2.2 Coplanar-based antenna

a. Antenna configuration

The proposed dipole-based antenna has the advantages of omnidirectional radiation pattern and easily controls the dimensions. However, as mentioned, the realized gain is low and to integrate with rectifier circuit need further development of the transition circuit.

resonant frequency are parameters of the small folded-slot patch ($xi2, xf2, yi2, yf2, xc, gx, xl2$). On the other hand, the parameters that have the most influence on the second and third resonant frequencies and their adaptation are parameters of the first folded-slot patch ($xpat, ypat$). The second and third resonant frequency can be separately controlled by the slot between the patch and the surrounded ground ($g1, g2, xm1$).

Table 2-5 Influence of parameters of proposed antenna

Parameters	f1			f2			f3		
	fresonant	Re(Zant)	Img(Zant)	fresonant	Re(Zant)	Img(Zant)	fresonant	Re(Zant)	Img(Zant)
xsub ↑	-	↑	-	-	↑ lightly	-	-	↓ lightly	-
ysub ↑	-	-	-	-	↓	↓	-	-	-
xpat ↑	-	↓	-	↓	-	-	↓	-	-
ypat ↑	↓ lightly	-	↑ lightly	↓	-	-	↓	-	-
xi2↑	↓	↑	↓	-	-	-	-	↑	↑
xf2↑	↑ lightly	-	-	-	-	-	-	↑	↑
yi2 ↑	↓	↑	↑ lightly	-	-	-	-	-	-
yf2 ↑	↑	↓	-	-	-	-	-	-	-
g1 ↑	↓	↓	-	-	-	-	↑	↓	↓
g2 ↑	↓ lightly	-	-	↑	-	-	↑ lightly	↓	↓
xl2 ↑	↑	-	-	-	-	-	-	↓	↓
gx ↑	↓	-	-	-	-	-	-	-	-
xc ↑	↑	↓	↓	↑	-	-	↑	-	-
xm1↑	↓ lightly	-	↑	↓	↓	↑	↑	↑	↑
ym1 ↑	-	↓	↑	↓ lightly	↑	↑	↓	↑	↓

f1, f2, f3: first, second and third resonant frequency
 Re(Zant): real part of antenna's impedance at the resonant frequency
 Img(Zant): imagine part of antenna's impedance at the resonant frequency
 -: unaffected
 ↑: increased
 ↓: decreased
 ↑ or ↓ lightly: compared to other resonant frequencies

Table 2-6 Optimized parameter values of the proposed antenna

Symbol	Value (mm)	Symbol	Value (mm)	Symbol	Value (mm)
xsub	87	xi2	45.5	xl2	0.4
ysub	77	xf2	47.5	gx	0.3
xpat	80	yi2	20	xc	1
ypat	54	yf2	23	ym1	11.8
xl	3	g1	1.2	g	0.3
g	0.3	g2	1	xl	3

The optimized design values for all parameters are obtained as given in Table 2-6. The antenna has three resonant frequencies: GSM 900 MHz, GSM 1800 MHz, and LTE 2.6 GHz. All resonant frequencies can be controlled independently.

Fig. 2-16a presents the simulated reflection coefficient of proposed antenna. The antenna has a simulated gain of 1.73 dBi, 4.29 dBi, and 6.67 dBi at frequencies 900 MHz, 1800 MHz and 2.6 GHz, respectively (Fig. 2-16b,c,d). The total size of the antenna is 87 x 77 mm².

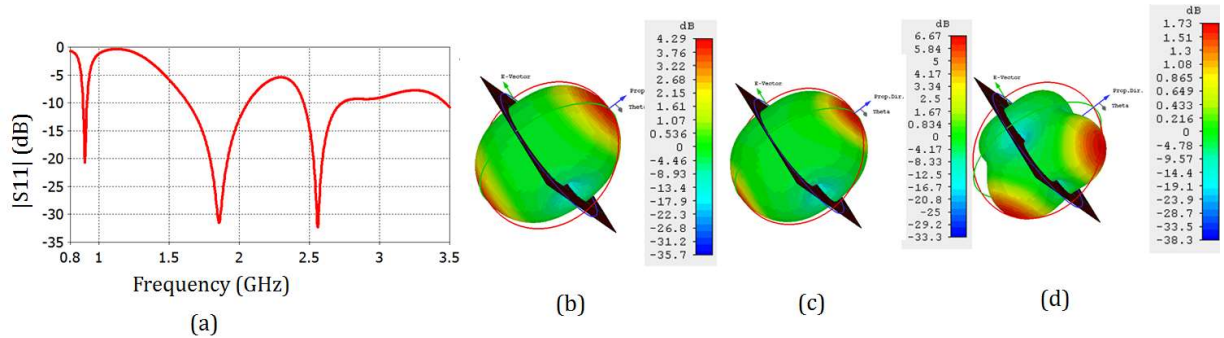


Fig. 2-16 (a) Simulated results of reflection coefficient; Simulated results of radiation pattern at (b)900 MHz; (c)1800 MHz; (d) 2.6 GHz.

b. Bending and folding analysis

The performances of the antenna in the bending and folding conditions are important to evaluate the adaptability of the system to different forms of packaging, objects, and applications. A parametric analysis was carried out to invest the impact of bending (parameter $rbend$) and folding (parameter u and v) effects on the performance of the antenna.

The proposed antenna is bent in function of radius $rbend$ and is folded in two directions in function of length u and width v along x-axis and y-axis as described in Fig. 2-17.

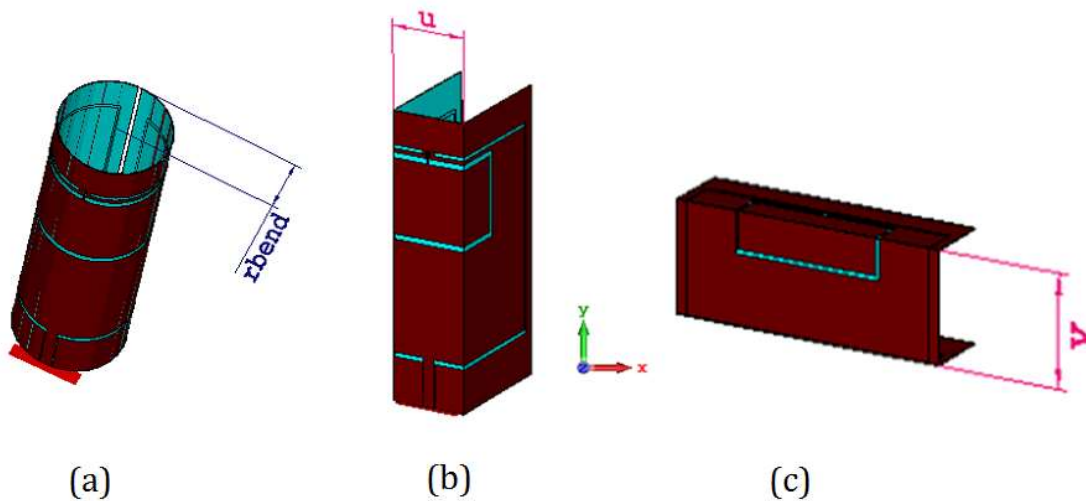


Fig. 2-17 (a) Bending antenna in function of radius $rbend$; (b) folding antenna in function of length u ; (c) folding antenna in function of width v

Fig. 2-18, Fig. 2-19 and Fig. 2-20 show the simulated reflection coefficient of bending and folding antenna with different radius, length, and width.

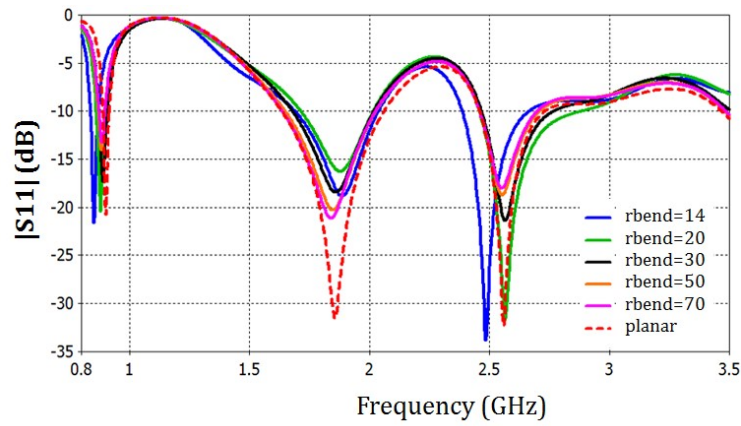


Fig. 2-18 Simulated reflection coefficient of bending antenna at different bending radius $rbend$ (mm)

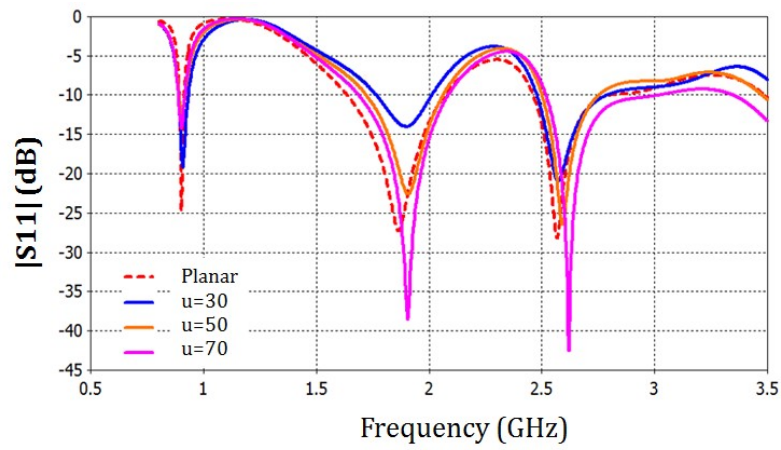


Fig. 2-19 Simulated reflection coefficient of folding antenna at different folding length u (mm)

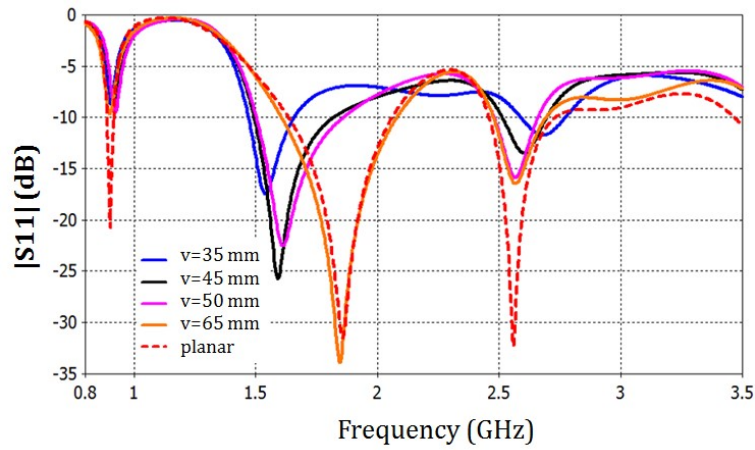


Fig. 2-20 Simulated reflection coefficient of folding antenna at different folding width v (mm)

For both bending and folding configurations along the x-axis, the reflection coefficient has been slightly changed, which indicates that the proposed antenna preserve its resonant frequencies. However, the folding along the height of antenna along y-axis has significantly changed its resonant frequencies. This can be explained by the fact that the polarization is linear along the y-

axis. Therefore, the deformation along this axis can actually change the operating frequency of the antenna.

Regarding the radiation properties, the radiation pattern maintains its form but the gain is degraded due to the deformation of the antenna. Table 2-7 provides the simulated in different configurations of bending and folding. The results show that the more the antenna is bent or folded, the more the gain is degraded. The extreme configuration at which the antenna maintains its characteristic is $rbend=14$ mm; $u=30$ mm and $v=65$ mm.

Table 2-7 Simulated gain of proposed antenna at different configurations

Simulated gain (dBi)		900 MHz	1800 MHz	2.6 GHz
Flat structure		1.73	4.29	6.67
Bending	$rbend=14$ mm	-0.46	1.933	4.17
	$rbend=20$ mm	1.15	2.79	4.9
	$rbend=30$ mm	1.67	3.64	5.87
	$rbend=50$ mm	1.34	4.18	6.36
	$rbend=70$ mm	1.38	4.29	6.43
Folding	$u=30$ mm	1.52	2.83	4.82
	$u=50$ mm	1.3	3.97	5.39
	$u=70$ mm	1.68	4.49	6.67
Folding	$v=35$ mm	-0.1	2.63	2.67
	$v=45$ mm	-0.1	3.32	2.9
	$v=50$ mm	-0.1	3.48	4.4
	$v=65$ mm	1.4	4.27	6.04

c. Fabrication and measurement

The antenna was printed to the PET substrate thickness 0.175 mm using the screen-printing technique. Fig. 2-21 shows the prototype of the fabricated antenna in flat, bending and folding configurations. While the folding configuration along y-axis did not meet the requirement of stable resonant frequency, only the folding configuration along the x-axis is fabricated and characterized.

Simulated reflection coefficient S11 and radiation pattern were compared to the experimental results in three configurations. The measured reflection coefficients are provided in Fig. 2-22 and Fig. 2-23. It is observed that good agreements between measurement and simulation are achieved and the antenna is matched at the resonant frequencies.

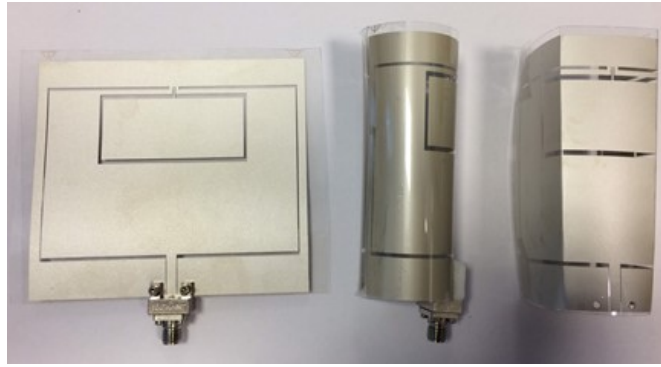


Fig. 2-21 Fabricated antenna in flat, folding and bending configurations

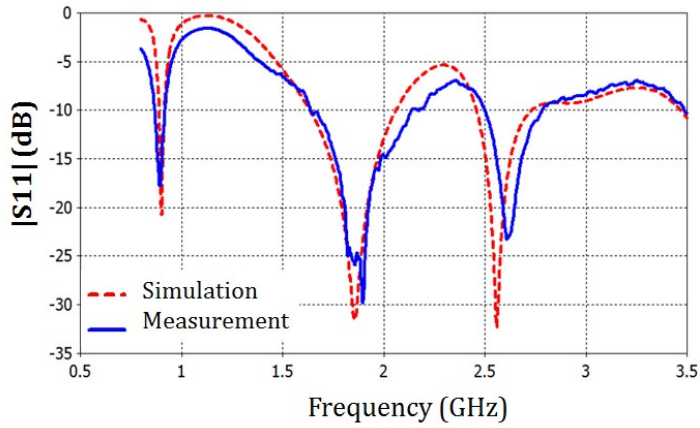


Fig. 2-22 Simulation and measurement reflection coefficient of the flexible coplanar antenna, in planar state

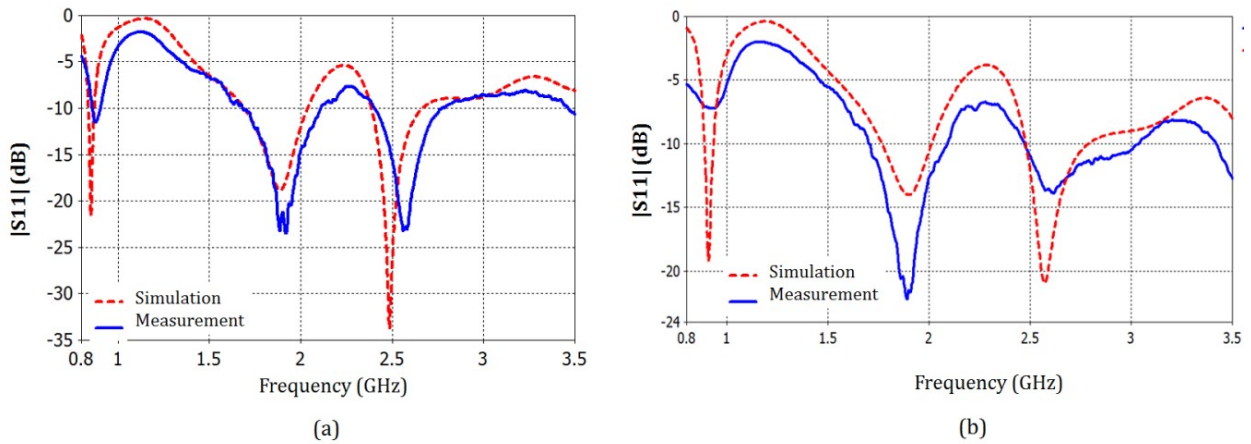


Fig. 2-23 Simulated and measured reflection coefficient of the flexible coplanar antenna (a) by bending $rbend=14$ mm; (b) by folding along x-axis $u=30$ mm.

The radiation pattern of the antenna in two planes and three configurations (flat, bending and folding) was measured (Fig. 2-24, Fig. 2-25, Fig. 2-26). The simulated and measured results show that radiation patterns at resonant frequencies are slightly changed for different radius of curvature and different length of folding. The realized gain of three configurations is provided in Table 2-8. The proposed antenna has the best performances at flat configuration. The folded configuration gives a similar size to bent configurations but the performance is better.

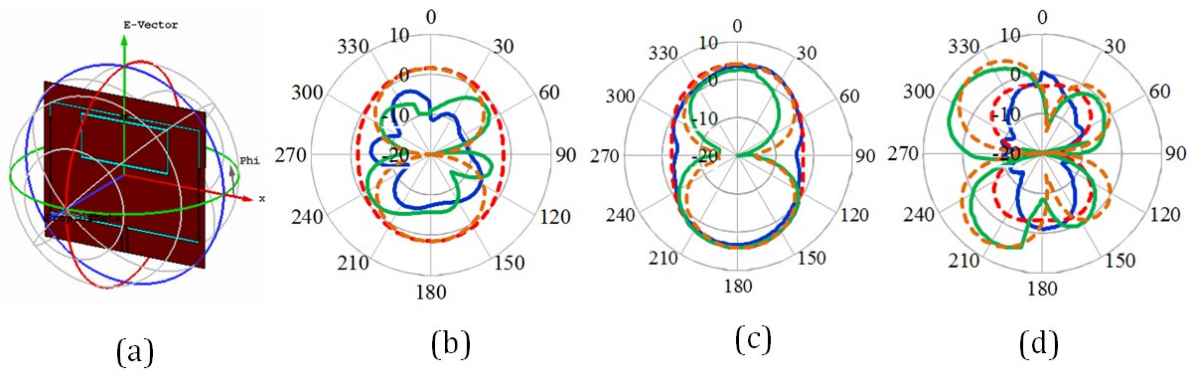


Fig. 2-24 Radiation pattern of the antenna in flat configuration (a) at (b) 900 MHz; (c) 1800 MHz; (d) 2.6 GHz

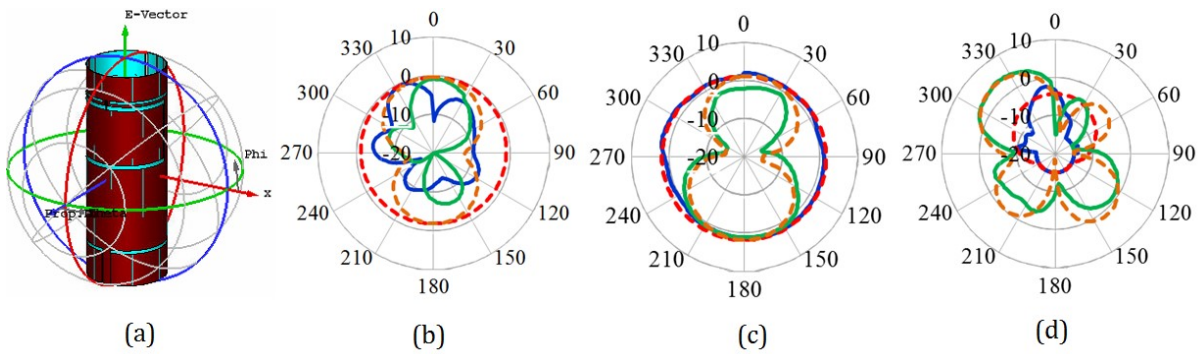


Fig. 2-25 Radiation pattern of the antenna in bending configuration (a) on toward a cylindrical form $r_{bend}=14$ mm: (b) 900 MHz; (c) 1800 MHz; (d) 2.6 GHz

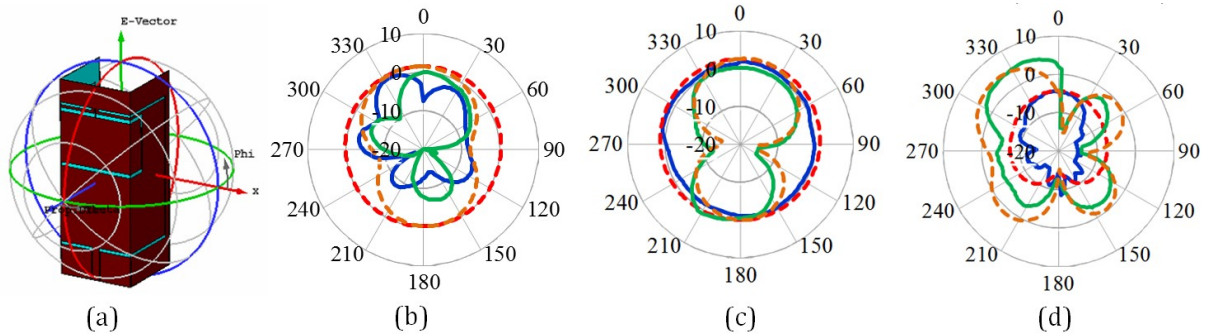


Fig. 2-26 Radiation pattern of the antenna in folded configuration (a) along x-axis, $u=30$ mm: (b) 900 MHz; (c) 1800 MHz; (d) 2.6 GHz

Table 2-8 Measured gain of proposed antenna at three configurations

Measured gain (dBi)	900 MHz	1800 MHz	2.6 GHz
Flat structure	1.37	4.16	6.15
Bending $r_{bend}=14$ mm	-0.57	2.23	4.39
Folding $u=30$ mm	0.58	1.99	4.89

Table 2-9 Comparison between coplanar flexible antennas presented in the literature (λ_g is guided wavelength at lowest resonant frequency)

Reference	Material (thickness, ϵ_r , $\tan\delta$)	Size ($\lambda_g \times \lambda_g$)	Frequencies (GHz)	Gain (dBi)	Bandwidth
Proposed antenna	PET (0.175 mm; 3.21; 0.0049)	0.37x0.33	0.9 1.8 2.6	1.37 4.16 6.15	3% 23.6% 13%
[96]	Silicon (0.3 mm; 3.3; 0.007)	0.07x0.06	2.45	-23	11.4%
[78]	Rogers5880 (0.127 mm; 2.2; 0.0009)	0.35x0.29	1.574	3.57	2%
[77]	Rogers5880 (0.127 mm; 2.2; 0.0009)	0.54x0.21	1.561	5.76	5%
[97]	Roger5880 (0.127 mm; 2.2; 0.0009)	0.45x0.31	1.2 2.4 3.5 5.2	5.47 5.88 1.97 3.56	23.9% 8.5% 4.3% 7.1%
[98]	Kapton (0.11 mm; 3.5; 0.002)	0.42x0.42	1.2 2 2.6 3.4	-1.2 0.6 2.1	54.4% 14% 23.5% 17.2%
[99]	Kapton (0.13 mm; 3.48; 0.002)	0.50x0.35	1.9 5.4	-2.8 0.9	51% 60%
[74]	PET (0.1 mm; 3; 0.008)	0.66x0.35	2.36 3.64	0.7 0.79	6.8%
[100]	PTFE (0.127 mm; 2.2; 0.0009)	0.73x0.36	3.5 9-11	~2 ~2	5.7% 20%
[101]	Kapton (0.58 mm; 3.4; 0.002)	0.70x0.48	3 7 13	2 4 5	116% 35.7% 38.4%
[102]	RO4003C (0.2 mm; 3.38; 0.0027)	0.95x0.71	2.6 3.8	2.34 6.3	57.7% 49.7%
[103]	Felt fabric (1.1 mm; 1.38; 0.023)	0.93x0.93	2.45 5.8	3.9 (6.4) 5.2 (7.6)	4% 16%
[104]	Rogers3003 (0.5 mm; 3; 0.0013)	-	2.45	1.39	6.5%

Table 2-9 provides a comparison of performance between the proposed antenna and others flexible antenna designs in the literature using the same coplanar waveguide technique, in ascending order of electrical size. It is found that the proposed antenna offers the best tradeoff in term of gain and dimensions.

d. *Conclusion*

In this section, a novel coplanar-based antenna was designed on flexible PET substrate. The antenna operates at three bands of frequency that correspond to three mobile telephone services GSM 900 MHz, GSM 1800 MHz and LTE 2.6 GHz. The proposed antenna has two main advantages. First, it provides a higher gain in compared with the dipole-based antenna described above and also other flexible coplanar-based antennas in literature. Secondly, the flexibility allows it to be bent and folded while maintaining the performances, The antenna can change from the dimension 87 mm x 77 mm in a flat configuration to 30 mm x 27 mm x 77 mm in the form of a rectangular box or a cylinder with a radius of 14 mm.

2.3 **Technique to overcome high-loss substrate**

The result of the first design on the paper substrate has shown the primary drawback of paper substrates, which is high loss characteristic. This aspect significantly degrades antenna gain, which is an important consideration for energy harvesting systems.

Previous attempts to overcome this limitation have included a study on inkjet printing processes to increase conductivities and in which is presented the studies of Vivaldi antenna and log-periodic dipole array antenna [105]. However, these antennas lack ground plane and are very susceptible to interference from surrounding constructs in the environment in several specific applications.

Others solutions were proposed using inkjet-printed antennas with an integrated artificial magnetic conductor (AMC) by using ground-backed frequency selective surfaces (FSS) [106][79] However, this requires a large electrical size (around $1\lambda \times 1\lambda \times 0.03\lambda$), where λ is the free-space wavelength.

In the current section, an antenna patch on high loss paper substrate applying suspended plate technique was designed in order to improve the obtained gain. To maintain the low profile of the antenna, the miniaturization process is used to reduce its original size. The proposed antenna operates in GSM frequency 1800 MHz and can be used in an RF energy harvesting system.

2.3.1 Design and characterization of suspended patch antenna

a. Paper substrate characteristics

In case of using the paper substrate above (permittivity of 3.359, loss tangent of 0.125) to design a conventional microstrip patch antenna of 80mm × 70mm, due to the loss tangent, the realized gain is low about -5 dB and the radiated efficiency of -18 dB at 1800 MHz (Fig. 2-27).

The aim of the following design is to improve these performances of the antenna.

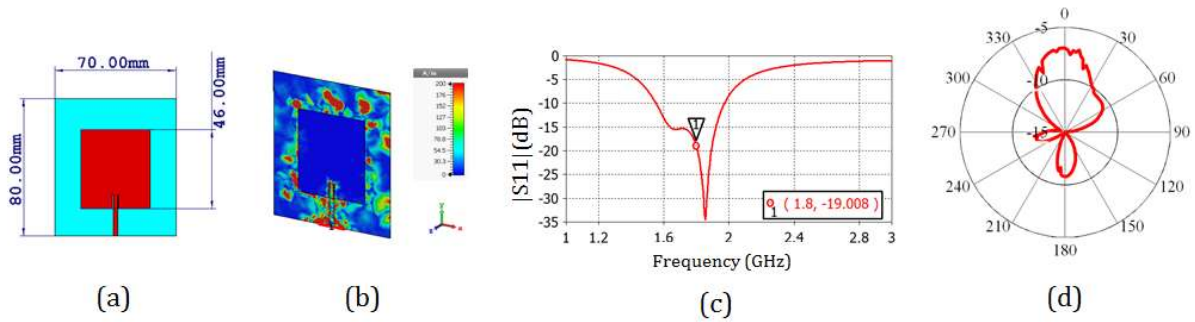


Fig. 2-27 (a) Conventional microstrip patch antenna using high-loss substrate; (b) simulated surface current of conventional patch at 1800 MHz; (c) simulated results of reflection coefficient; (d) simulated results of E-plane radiation pattern at 1800 MHz

b. Antenna configuration

In order to overcome the previously mentioned drawback, we changed the medium between radiating element and ground plane to air-filled medium (air or foam) by using another printed substrate suspended over a ground plane (Fig. 2-28). This antenna is excited by a 50Ω coaxial cable.

While increasing the spacing d between the radiating element and ground plane, the probe becomes longer which causes a higher input inductance around the frequency of resonance. The circular slot is inserted around the excitation point to create the capacitive coupling effect and compensate this inductance.

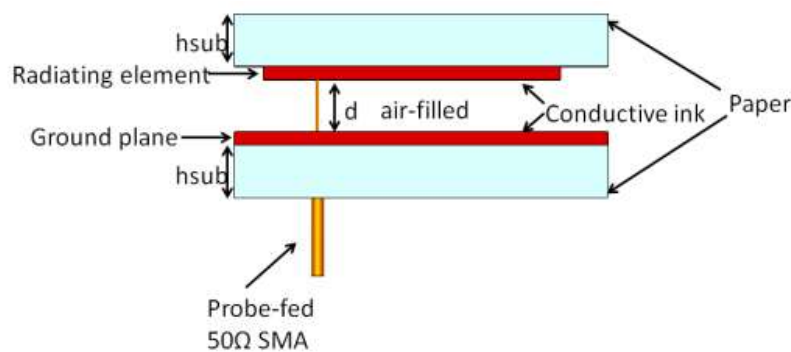


Fig. 2-28 Configuration of inverse suspended patch antenna.

The antenna is optimized at a frequency of 1800 MHz. Due to the low permittivity of the air-filled medium; the antenna becomes larger than the conventional one (Fig. 2-29). In order to reduce this size, the antenna has been folded multiple times to take advantage of the flexibility of the paper substrate (Fig. 2-30).

Another advantage of this antenna is with the ground plane, it can be integrated within different surfaces and materials without perturbation from positioning effects and can be used in various applications.

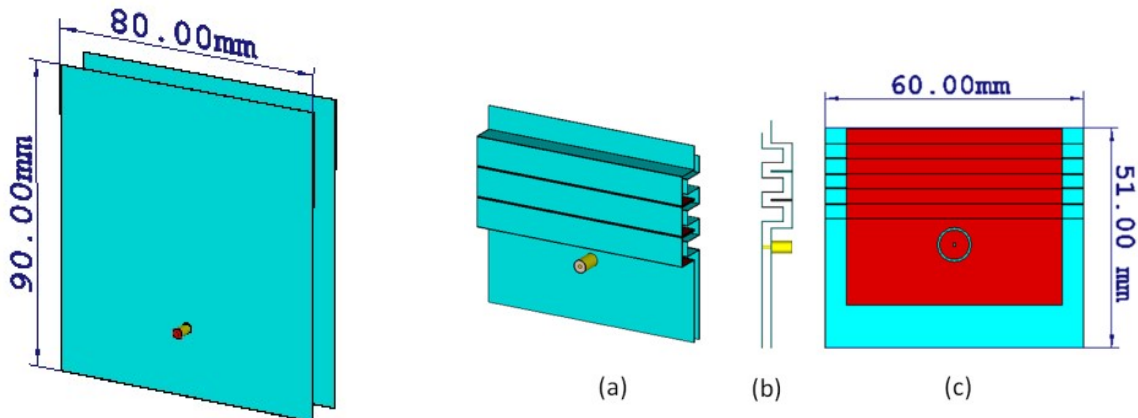


Fig. 2-29 Configuration of antenna before miniaturizing

Fig. 2-30 Configuration of the proposed antenna after miniaturizing: (a) Perspective view; (b) Side view; (c) Front view of radiating element.

2.3.2 Simulation and measurement results

The study used a transient solver within CST Microwave Studio for simulation. The dimensions of inverse suspended patch antenna (ANT1) are 90 x 80 x 12 mm³ to obtain the resonant frequency at 1800 MHz and simulated gain of 8.1 dBi. After miniaturizing, the proposed antenna (ANT2) has reduced the size of more than 55%, of 60 x 55 x 5 mm³, which corresponds to the electrical size of $0.36 \lambda \times 0.33 \lambda \times 0.03 \lambda$ and has a gain of 5.6 dBi. Two prototypes of proposed antenna ANT1 and ANT2 were then fabricated (Fig. 2-31).

A good agreement between simulation and measurement is observed at the resonant frequency of both prototypes (Fig. 2-32, Fig. 2-33). The radiation patterns of both antennas are directional and measured gain of ANT1 and ANT2 are, respectively, 7.6 dBi and 5.3 dBi. The simulated efficiency is around 90%.

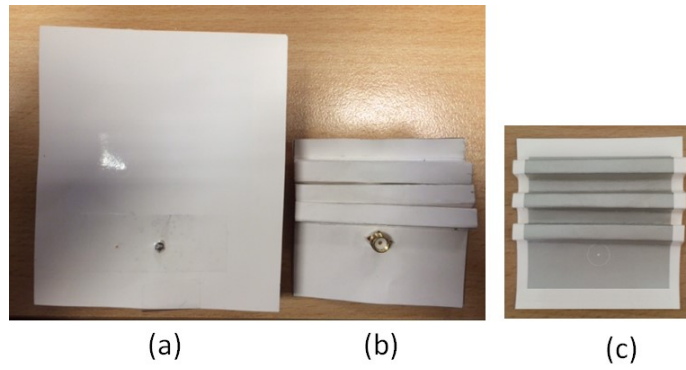


Fig. 2-31 Photo of fabricated prototype using adhesive copper: (a) Antenna before miniature (ANT1); (b) Antenna after miniature (ANT2); (c) Radiating element of miniaturized antenna (ANT2)

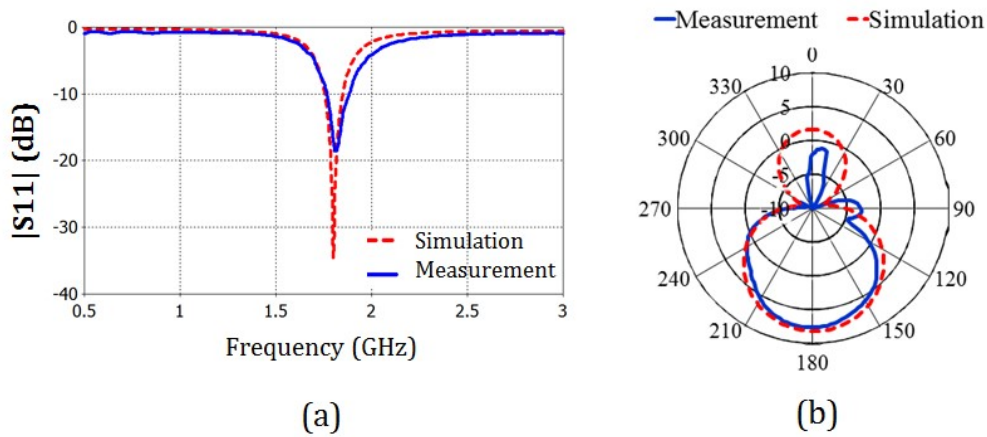


Fig. 2-32 Simulation and measurement of proposed antenna before miniature (ANT1): (a) Reflection coefficient; (b) E-plane radiation pattern at 1800 MHz

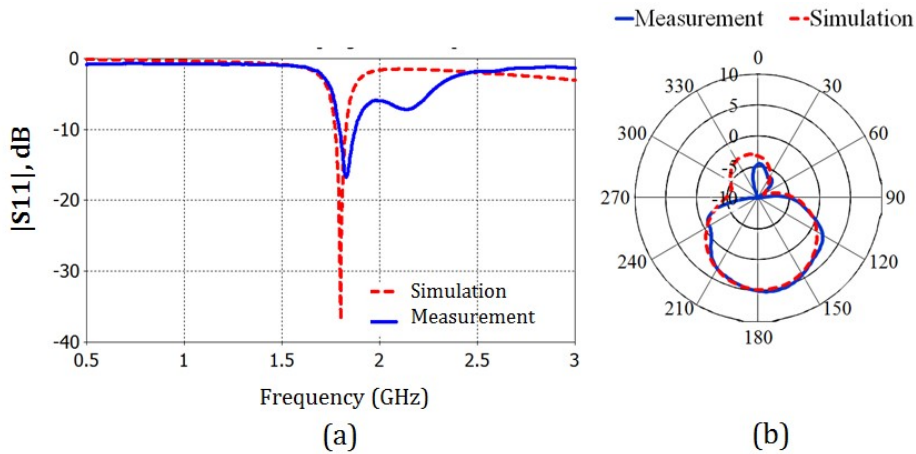


Fig. 2-33 Simulation and measurement of proposed antenna after miniature (ANT2): (a) Reflection coefficient; (b) E-plane radiation pattern at 1800 MHz

This section presented a suspended miniaturized antenna fabricated with high loss paper substrate that has been optimized to enhance gain. The proposed antenna has a total size of $0.36\lambda \times 0.33\lambda \times 0.03\lambda$, the measured gain is 5.3 dBi and radiation efficiency is -0.5 dB at GSM frequency of 1800 MHz. With this design, an increase in 10 dB of gain is achieved in comparison

with conventional patch antenna using this high loss paper substrate while maintaining low profile dimensions.

2.3.3 Applying for flexible multi-band antenna with suspended ground

a. Antenna configuration

The same principle of the suspended technique is applied for the design of a multi-band paper antenna with the suspended ground. The same substrate as mentioned above was used. The antenna consists of two parts, radiation element and a ground element, which were separated by the distance d . In order to decrease the dimension of the antenna while taking advantage of suspended structure, the radiation element was folded as described in Fig. 2-34. The slot was created in order to increase the line of surface currents at a lower frequency (Fig. 2-35). The antenna was optimized at two frequencies 1800 MHz and 2.1 GHz. The antenna was fed by probe, therefore, a circular slot was added to compensate the inductance effect of the feeding line.

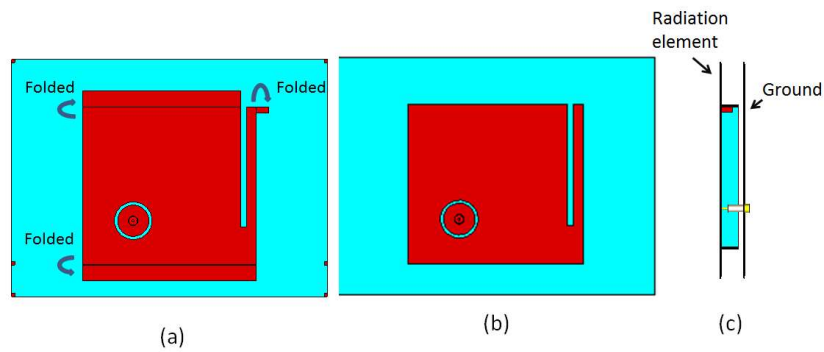


Fig. 2-34 Configuration of multi-band patch antenna (a) Flat antenna-top view; (b) Folded antenna – top view; (c) Folded antenna with suspended ground – side view

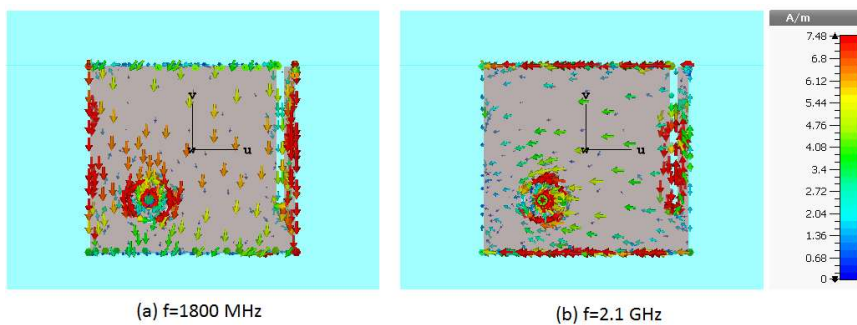


Fig. 2-35 Surface currents of proposed antenna at frequency (a) 1800 MHz and (b) 2.1 GHz

b. Simulation and measurements

The study used CST Microwave Studio for simulation. The dimensions of radiation element of multi-band suspended patch antenna are $50\text{mm} \times 55\text{mm} \times 8\text{mm}$ to obtain the resonant frequencies at 1800 MHz and 2.1 GHz. The prototypes of the proposed antenna were then fabricated (Fig. 2-36).

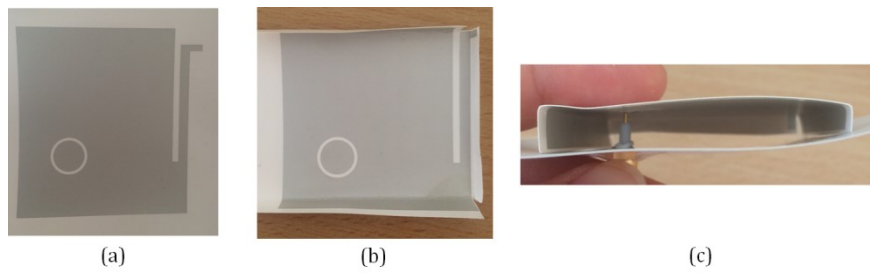


Fig. 2-36 Photo of fabricated suspended multi-band antenna using adhesive copper (a) top view before folded; (b) top view after folded; (c) side view.

A good agreement between simulation and measurement is observed at the resonant frequency (Fig. 2-37). The radiation patterns of both antennas which are shown in Fig. 2-38 are directional and realized gain of proposed antenna are, respectively, 5.24 dBi and 6.91 dBi.

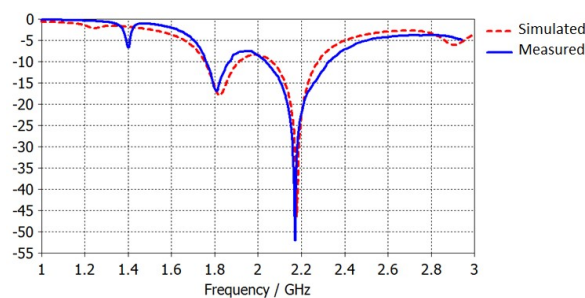


Fig. 2-37 Simulated and measured of reflection coefficient of multi-band suspended antenna

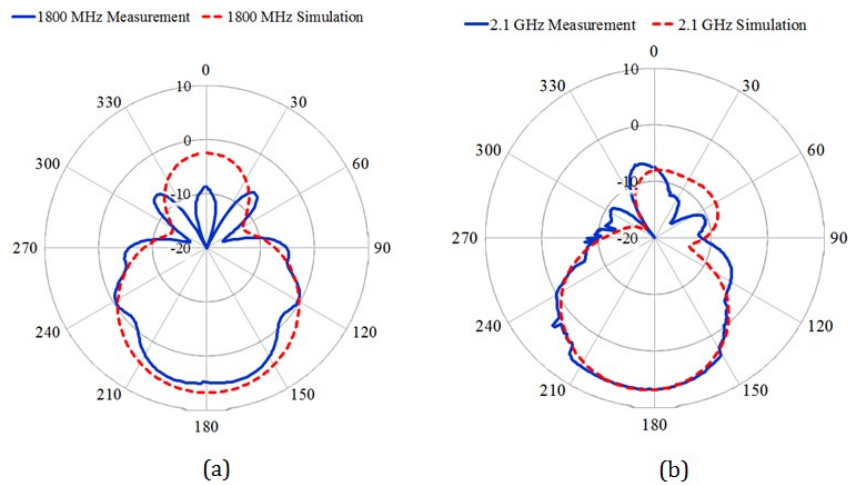


Fig. 2-38 Simulation and measurement of E-plane radiation pattern at two operational frequencies (a) 1800 MHz; (b) 2.1 GHz

The result shows the improvement in gain of the antenna using high-loss paper substrate by using the suspended technique. The proposed prototypes are the evidence show the effectiveness of this method in order to enhance the gain of the patch antenna on the high-loss substrate.

2.4 Adjustable frequency antenna using flexible substrate

The primary challenge to ambient energy harvesting approach is linked to a multitude of different power levels and frequencies used in wireless systems. For example, inside buildings and similar structures, the most common signal in this environment would be those of Wireless Local Area Networks (WLANs) 2400–2484 MHz as they are most stable and powerful indoors [30], [31]. However, the sources of electromagnetic power available outdoors come from alternate sources such as cellular base station antennas of mobile services such as GSM, UMTS, LTE frequencies [107], [108]. In addition, mobile phone frequencies are not the same all around the world. For example in North America, GSM operates on the primary mobile communication bands of 850 MHz and 1900 MHz while in Africa, Europe, Middle East and Asia, most of the providers use 900 MHz and 1800 MHz bands.

The multi-frequency problem requires that any energy harvesting devices have to be compatible with all the bands of the service available on site. This issue normally can be solved using multi-band antennas. However, studies thus far have been limited to altering the operating frequency of antennas to match the location. Instead, this section proposes a novel reconfigurable frequency antenna design that includes two parts: one fixed part and another changeable part, which modifies the resonant frequency of the antenna. The antenna was made by printing a patch with a conductive ink over a flexible substrate, which can easily be stuck or removed from any package. With this technology, the rest of the circuit including the rectifier stays stable inside the system packaging, making the whole circuit easy to install and where the frequency can be easily modified.

This study proposes a configuration with three antennas that operate on four frequency bands: GSM 1800 MHz, GSM 1900 MHz, UMTS 2100 MHz for outdoor application and WLAN 2.4 GHz for indoor application of RF energy harvesting. The included results of simulation and experimental data show that this configuration is suitable for the adjustable frequency purpose.

2.4.1 Antenna configuration

The radiating element is fed by the inside component using an aperture-coupled technique, which does not require a direct connection between the antenna and the feed line. The feed network and the rest of the circuit stay the same inside the system packaging.

The patch antenna was used for the external component. In order to make the removable antenna convenient to install and to operate, we propose to use a flexible substrate, which is very thin and compact. The substrate used for this design is a PET Polyethylene terephthalate (PET) with a thickness of 0.1mm, a relative permittivity $\epsilon_r = 3.76$ and a loss tangent $\tan\delta = 0.0049$. The conductive layer is realized with a commercial conductive ink made with silver particles, the

thickness of 0.007mm. The flexible and thinness substrate is able to function as an antenna, without a need to change the size or design of the circuit.

The feed network was etched on a Rogers 4003 substrate (thickness of 0.813mm, relative permittivity $\epsilon_r=3.55$ and loss tangent $\tan\delta = 0.0027$). The thin rectangular slot is the ideal aperture shape for coupling and we have to put this aperture at the optimal location to maximize the coupling effect.

Fig. 2-39 shows the configuration of the proposed structure with the antenna, the cover box, the feed network.

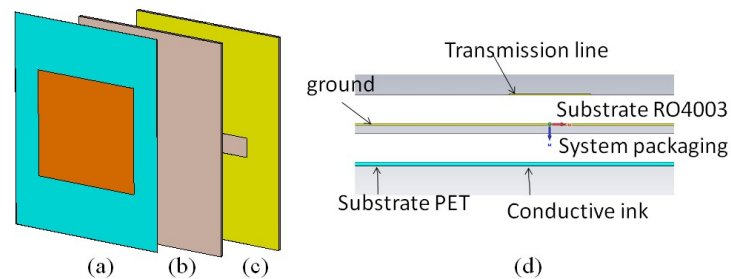


Fig. 2-39 Configuration of proposed circuit (a) Antenna; (b) Cover box; (c) Feed network; (d) Side view

2.4.2 Simulation and measurement results

The transient Solver within CST Microwave Studio was used for simulation. The dimensions and position of the outside patch were optimized in order to obtain the resonance at targeted frequencies while keeping the parameters of the feed network. The total size of the fixed part over the outside of the packaging box is $43 \times 60 \text{ mm}^2$. The size and form of the rectangular patch antenna were altered from $43 \times 47 \text{ mm}^2$ to $41 \times 44 \text{ mm}^2$ and $29 \times 29.5 \text{ mm}^2$ to obtain the resonant frequency at downlink bands of GSM 1800 MHz, GSM 1900 MHz and WLAN 2.4 GHz, respectively (Fig. 2-40a,b,d). The circular patch with a diameter of 42.6 mm was used for the resonant frequency at 2100 MHz (Fig. 2-40c). The 10 dB return-loss bandwidth covers the desired frequencies for the four cases.

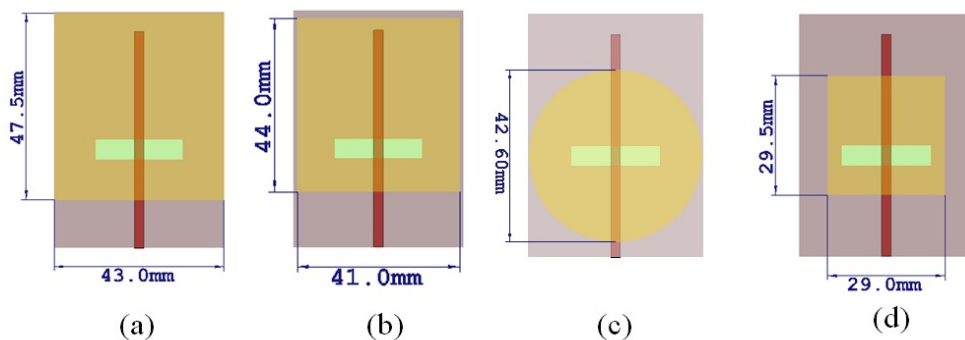


Fig. 2-40 Parameters of proposed antenna for (a) GSM 1800 MHz; (b) GSM 1900 MHz; (c) UMTS 2100 MHz; (d) WLAN 2.4 GHz

Radiation characteristics of the proposed antenna were also studied. The simulated far-field radiation pattern of the antenna with four frequency bands is shown in Fig. 2-41. The radiation patterns of the antenna are directional and the maximum simulated gain is 4.5 dBi at 2.4 GHz, the simulated efficiency is around 80%.

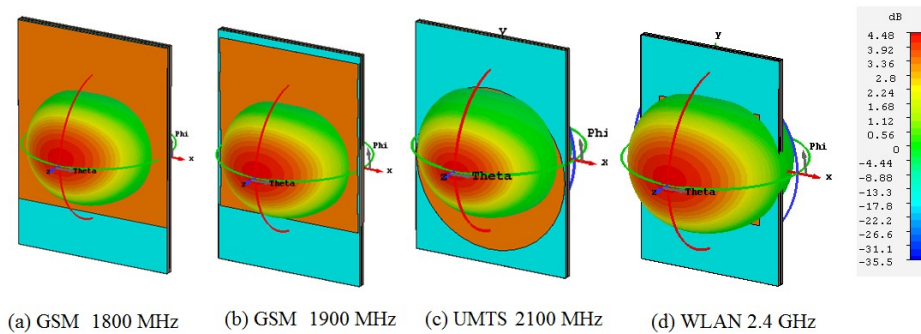


Fig. 2-41 Simulated far-field pattern of the antenna at four frequency bands

The antenna with optimal dimensions was then realized using R04003 substrate for the inside component and using PET substrate for the outside component. Fig. 2-42 presents photos of the prototypes.

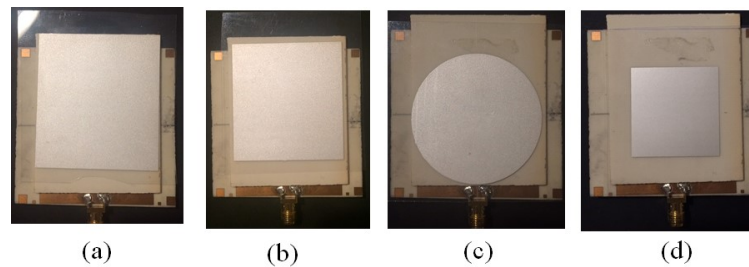


Fig. 2-42 Fabricated antenna with removable patch antenna for frequency of (a) 1800 MHz; (b) 1900 MHz; (c) 2100 MHz; (d) 2.4 GHz

The measurement of reflection coefficient was performed by using an Agilent Vector Network Analyzer (VNA) 8720ES over the frequency range 1 GHz to 3 GHz. Fig. 2-43a presents the simulated and measured reflection coefficient in dB of the proposed antenna for each working frequency. A good agreement is observed for all the resonant frequencies. The radiation characteristic was characterized in an anechoic chamber. The E-plane radiation is presented in Fig. 2-43b. The simulated and measured gain is also provided in Table 2-10.

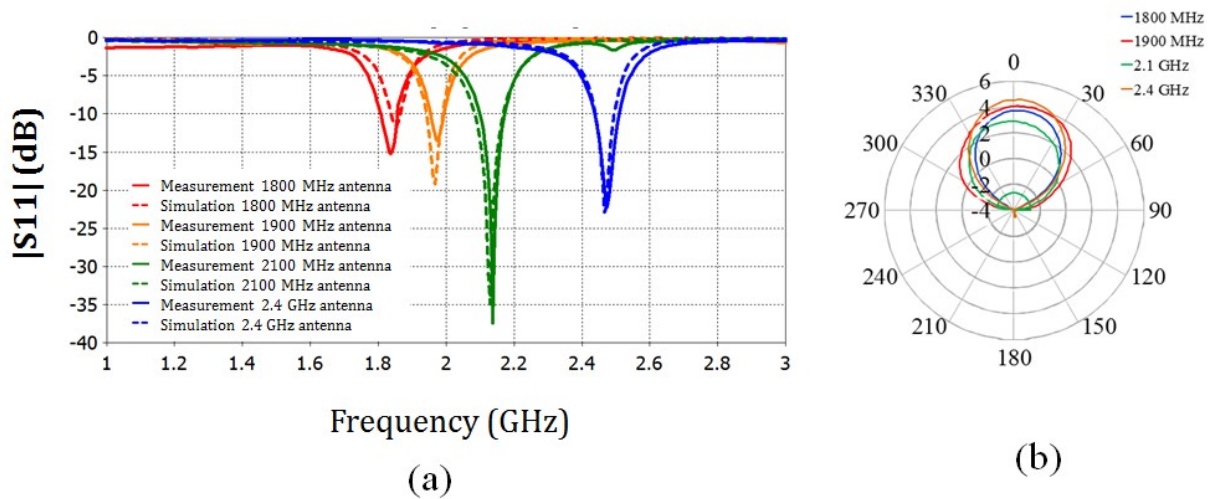


Fig. 2-43 (a) Simulation and measurement of the reflection coefficient at four working frequencies; (b) E-plane radiation pattern at four frequencies.

Table 2-10 Simulated and measured gain (dBi) at each frequency

Gain (dBi)	1800 MHz	1900 MHz	2100 MHz	2.4 GHz
Simulation	3.72	4.32	2.78	4.48
Measured	3.52	4.09	2.87	4.12

2.4.3 Conclusion

The design and development of a novel antenna with adjustable frequency is presented. The addressed frequency bands for RF energy harvesting applications are GSM 1800 MHz to GSM 1900 MHz, UMTS 2100 MHz and WLAN 2.4 GHz. The test results correlate well with initial simulation results. The proposed structure has the advantages of compactness, lightweight, adjustability and convenient to use in different radiated frequency environments.

2.5 High gain flexible antenna

2.5.1 Target of design

Instead of using an omnidirectional antenna, combining several directional antennas in multi-direction is another notable solution for ambient electromagnetic energy harvesting. Moreover, this solution provides higher gain antenna and can receive higher energy in each direction of antenna's propagation. This section aims to design a high gain flexible antenna based on PET substrate for this purpose. The fabricated antenna will be characterized in this section. The further application involves this high gain antenna on a flexible substrate will be developed later in Chapter 4.

2.5.2 Antenna configuration

The design based on the planar-printed quasi-Yagi structure and the geometry antenna is depicted in Fig. 2-44. This is a common concept and has been presented in previous researches [109]. The substrate used in this study is PET, which has a permittivity of 3.21, a loss tangent of 0.0049 and a thickness of 0.175 mm.

The antenna consists of two driven element and three director elements. The partial ground acts as a reflector of the antenna. The antenna's size is 61 x 61 mm² and the resonant frequency is 2.45 GHz.

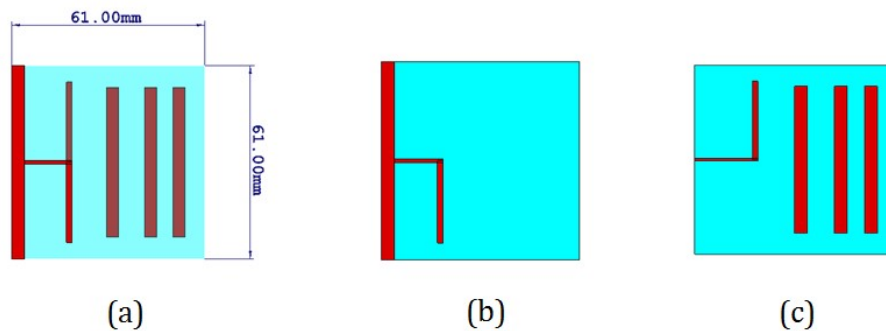


Fig. 2-44 (a) Configuration of basic planar-printed quasi-Yagi structure; (b) Top view; (c) Bottom view

The study used a transient solver within CST Microwave Studio for simulation. The basic quasi-Yagi on PET substrate has a directivity of 9.448 dBi and simulated gain of 8.1 dB at 2.45 GHz. The radiation efficiency of this antenna is 83.5% and total efficiency is 77%.

2.5.3 Fabrication and measurement

The antenna was fabricated using screen-printing technology to create a conducting ink layer made of silver nanoparticles with a thickness of 0.01 mm. Fig. 2-45 presents the photo of the fabricated antenna. The measured gain of the fabricated antenna is 6.93 dBi. The comparison of the simulated and measured reflection coefficient and E-plane radiation is depicted in Fig. 2-46.

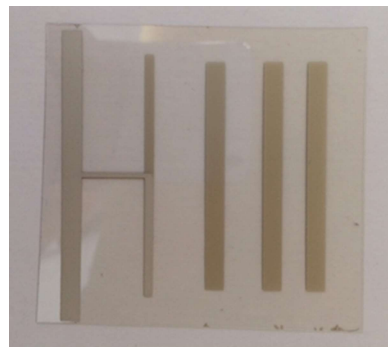


Fig. 2-45 Fabricated high gain antenna on flexible substrate

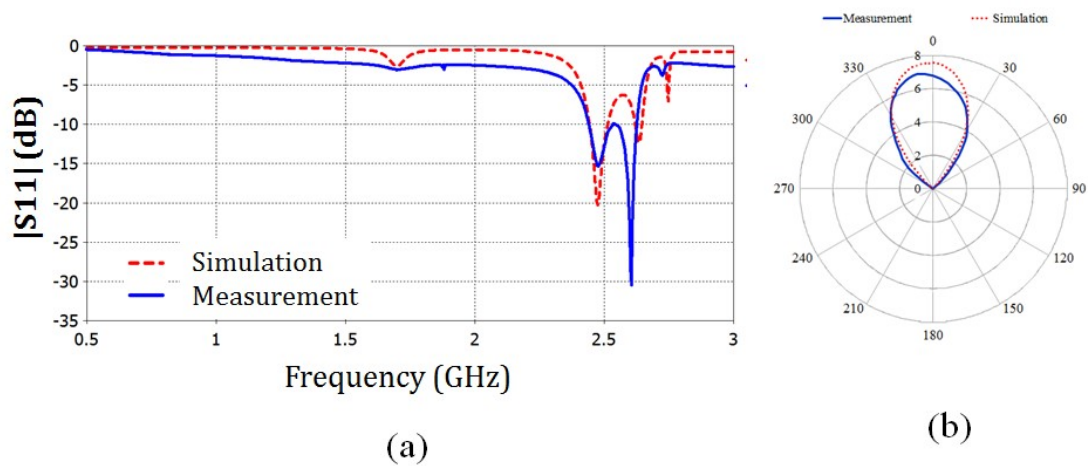


Fig. 2-46 E-plane radiation pattern of fabricated planar quasi-Yagi antenna

The design and results of this antenna will be applied in Chapter 4 of this thesis.

2.6 Conclusion

In this chapter, three different antenna configurations corresponding to different approaches of combination sources in RF energy harvesting was presented. Moreover, two antennas were developed based on a suspended technique to overcome the high-loss characteristic of the paper substrate. The antennas were designed by the CST Microwave studio and then were characterized in the anechoic chamber.

The first design aims to multi-frequency rectenna in which multi-band antenna was used. The 3D design in addition to the performance at the desired bands (1800 MHz, 2100 MHz, 2450 MHz and 5200 MHz), has the possibility to be adapted to different dimensions of packaging. The first dipole-based antenna was completely emerged in the form of a rectangular box and has omnidirectional radiation pattern. This allows the system receiving incident power from an unspecified source in ambient. However, due to the loss of paper substrate, the gain of the antenna was degraded comparing to a rigid substrate. The second coplanar-based antenna targeted the mobile telephone frequencies GSM 900 MHz, 1800 MHz and 2600 MHz, This antenna also has the flexibility feature as the first antenna but achieved a higher gain and more directional radiation pattern.

The technique targeted the problem of high loss substrate was mentioned following the first design. To overcome very high-loss of the substrate, the suspended technique was proposed. This technique allows an increase of about 10 dB of gain of a conventional patch antenna and can be applied to an antenna with broadband radiation pattern and their variations. A miniaturization of this antenna was also presented. This technique has been applied to multi-band antennas on a paper substrate. The antenna was fabricated and was tested and good results were achieved.

The next design serves the application in which the frequency of ambient source changes and depends on location. This design has one removable part outside of the packaging which allows changing the frequency of the antenna. The addressed frequency bands for RF energy harvesting applications are GSM 1800 MHz to GSM 1900 MHz, UMTS 2100 and WLAN 2.4 GHz. The test results correlate well with simulation results. The proposed structure has the advantages of compactness, lightweight, adjustability and convenient to use in different radiated frequency environments.

The last design targets the diversity antenna concept, in which high gain antenna was used in a 3D antenna system. The design based on the printed quasi-Yagi antenna and has high of 6.93 dBi. This design will be used in Chapter 4 for the development of the diversity antenna consists of four antennas that can be folded along the rectangular or cube box shape.

3. Rectifier

As introduced in Chapter 1, the rectifier is the key element of the receiver part in an RF energy harvesting system. The basic rectifier architecture consists of a matching circuit, a rectifier device, and a DC low pass filter (Fig. 3-1).



Fig. 3-1 Basic architecture of rectifier

The roles of each element are described as follows:

- The matching network such as a LC-circuit, is placed between the antenna and the rectifier circuit to ensure impedance matching and preserve maximum captured energy. The low-pass RF filter has the role of blocking the higher harmonics generated by the rectifier device such as diode from radiating through the antenna.
- The function of the rectifier is to convert the RF signals into a direct current by using rectifier devices such as Schottky diode.
- The DC side filter is also a low-pass filter and its role is to block the RF signal that has not been rectified by the diode and to pass only the DC signal. This low-pass output filter rejects higher order harmonics that are generated during the nonlinear rectification process.
- The terminal resistive load generally represents the input impedance of the device that consumes power.

The rectifier circuit discussed in this section is Schottky diode based rectifier, which is the preferred component for low-power RF applications, due to well-established and reliable technology process of the device. The advantages of the Schottky diode are a low forward voltage (threshold voltage) drop and high switching speed, thus they are convenient with the range of working frequencies defined above. This is also the most important component of the rectifier and therefore decides the overall conversion efficiency. The analysis in [35] has shown that diode SMS 7630 is the most commonly used low barrier Schottky diode for the development of RF energy harvesting.

In our research, we will analyze several models of low barrier Schottky diode including SMS 7630 and other models such as HSMS 2860, HSMS 2850 in order to propose a more precise diode model for low power energy harvesting system design.

3.1 Diode modeling

The design and development of Schottky diode based rectifier require precise data of parameters that define the diode performance. This information is crucial for the correct nonlinear simulation.

In literature, the SPICE model has been used for modeling diodes in circuit simulation. Normally, manufacturers provide SPICE models in the product datasheet. These documents, which will be examined in more detail below, list the main parameters of the diodes. However, those parameters could be altered due to the manufacturing process and could vary from every manufacturer. Due to the sensitivity of the rectifier efficiency in low-power application, it is necessary to take the measurement of actual devices and to extract real parameters. These extraction processes are greatly developed in the literature based on the basic equation of the diode. This section will present the extracting process for several samples and a discussion is given comparing nominal parameters and experimental results.

3.1.1 Diode characterization

a. Parameters of a Schottky diode

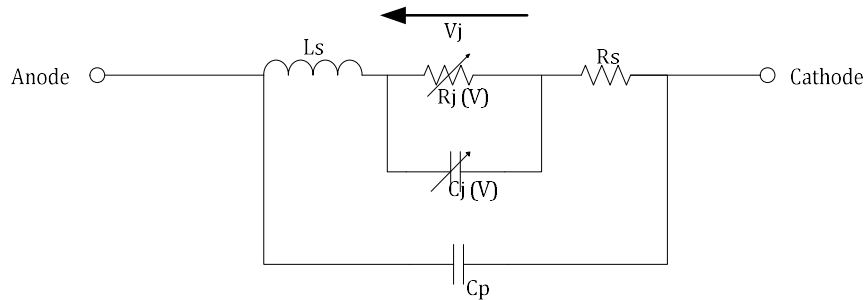


Fig. 3-2 Equivalent circuit of the zero-bias Schottky diode

Fig. 3-2 represents an equivalent circuit of the zero-bias Schottky diode: the junction capacitance C_j , junction resistance R_j , series resistance R_s , series inductance L_s and parallel capacitance C_p .

The current-voltage (I-V) static characteristic of a classic Schottky diode is given by Shockley diode equation:

$$I_D = I_S \left(e^{\frac{q}{nkT} V_j} - 1 \right) = I_S \left(e^{\frac{q}{nkT} (V_D - R_s I_D)} - 1 \right) \quad (3.1)$$

Where I_D : Current through the diode (A)

V_D : Voltage across the diode (V)

V_j : Bias voltage (external voltage across the depletion layer = $V_D - R_s I_D$)

I_S : Saturation leakage current in reverse bias (A)

n : Ideality factor. When the ideal diffusion current dominates, $n=1$; whereas when the combination current in the space-charge region dominates, $n=2$; generally, n has the value of between 1 and 2 when both currents are comparable [110].

kT : thermal energy at the absolute temperature (Kelvin), k is Boltzmann's constant = $138 \cdot 10^{-23}$ J/K

T : temperature (K)

q : electronic elementary charge = 1.6×10^{-19} C

With $\alpha = \frac{q}{nkT}$ is approximately $1/(25\text{mV})$ for $T=290\text{K}$ and $n=1$ at ambient temperature [111] the junction resistance of the diode R_j can be expressed as:

$$R_j = \frac{nkT/q}{I_D + I_S} = \frac{1}{\alpha(I_D + I_S)} \quad (3.2)$$

In addition, the junction capacitance of the diode C_j can be expressed as [112][113],:

$$C_j = \frac{dQ}{dV_D} = \frac{C_{j0}}{\left(1 - \frac{V_j}{\phi}\right)^M} \quad (3.3)$$

Where C_{j0} : zero-bias value

ϕ : Junction barrier potential

M : grading coefficient that varies ($\frac{1}{2}$ is used for step junction and $\frac{1}{3}$ is used for linearly graded junctions and most junctions are somewhere in between).

It is necessary to select a diode having high-speed switching characteristics in order to follow a high-frequency input signal and have a low cut-off voltage to operate at a low RF input power, which means a low biasing voltage V_j . Apart from this important parameter, the power conversion efficiency of a rectifier is mainly determined by three parameters [114]:

- Series resistance (R_s) which limits the output current and efficiency of the circuit.
- Zero-bias junction capacitor (C_{j0}) and C_p which affect low harmonic currents to oscillate through the diode
- Breakdown voltage (V_{br}) which limits the power handling capability of the rectifier circuit.

These parameters will be extracted from measurements.

b. Parameter extraction of equivalent circuit model

Curve-fitting method, which obtains parameters by fitting the simulated data to the measured data, is widely used in the literature based on diode equation (3.1). The main parameters such as I_S , n and R_S can be extracted from the I-V characteristic. The parameters C_{j0} , R_{j0} , V_j and M can be deduced from the capacitance-voltage (C-V) characteristics. The next section will present extraction method and its application.

In [115], the I-V response in (3.1) is proved invalid because the diode barrier height is not constant but is a function of the depletion layer electric field, thus the junction voltage. It depends on image force lowering the barrier and the effect of the interfacial oxide layer between metal and semiconductor, among others, that alter the I-V characteristic into:

$$I = I_S e^{\frac{qV_j}{nkT}} \left(1 - e^{-\frac{qV_j}{kT}} \right) \quad (3.4)$$

The threshold voltage is known as the gate voltage necessary to induce a conducting channel at the surface of the semiconductor under inversion [116]. When V_{in} is very small compared to this voltage, the series resistance R_S can be neglected due to the high resistivity of the Schottky barrier. Therefore equation (3.1) can be expressed as [117]:

$$I = I_S e^{\frac{qV_{in}}{nkT}} \left(1 - e^{-\frac{qV_{in}}{kT}} \right) \quad (3.5)$$

So we can deduce from (3.5) :

$$\ln \left(\frac{I}{1 - e^{-\frac{qV_{in}}{kT}}} \right) = \frac{qV_{in}}{nkT} + \ln(I_S) \quad (3.6)$$

The left-hand side of (3.6) can be obtained from the measurement and the right-hand side of this equation exhibits a linear function of V_{in} with the slope equals to $\frac{q}{nkT}$ and the intercept equals to I_S . After measuring the I-V characteristic of a Schottky diode, the ideality factor n and the reverse saturation current I_S can be determined from this curve.

There also exist many methods for identification of the series resistance from I-V characteristics. In [118], the series resistance is considered in the relation with the conductance of the diode. Let G_d be the conductance of the diode, so

$$G_d = \frac{dI}{dV} = \frac{q(1 - R_S \frac{dI}{dV})}{nkT} I = \frac{qI(1 - R_S G_d)}{nkT} \quad (3.7)$$

We can write (3.7) as:

$$\frac{I}{G_d} = \frac{nkT}{q} + I \cdot R_s \quad (3.8)$$

In the region where R_s is important, in accordance with higher V_{in} , we can deduce R_s from this equation.

To define the optimum impedance of the diode, we need to know all the parameters that have an influence on the input impedance of a diode. To estimate the input impedance, the voltage across the junction of the diode is the most important parameter since the impedance of the diode depends on R_j and C_j which change as functions of frequency, incident power and the voltage across the junction of the diode (V_{in}). By considering parasitic capacitance as the parallel capacitance, combining with (3.3), the total capacitance of a reverse-biased Schottky diode is given by [111]:

$$C_{tot} = C_{j0} \left(1 - \frac{V}{V_{j0}}\right)^{-M} + C_p \quad (3.9)$$

Using (3.9), the parameters C_{j0} , C_p , V_j and M can be deduced from the C-V measurements.

3.1.2 Measurements and results

a. Extraction of I_s and n

Fig. 3-3 shows the measured and analytical curve of a diode HSMS-2860 at small V_{in} . Extracted parameters: $I_s=2.4e-8$ A and $n=1.08$.

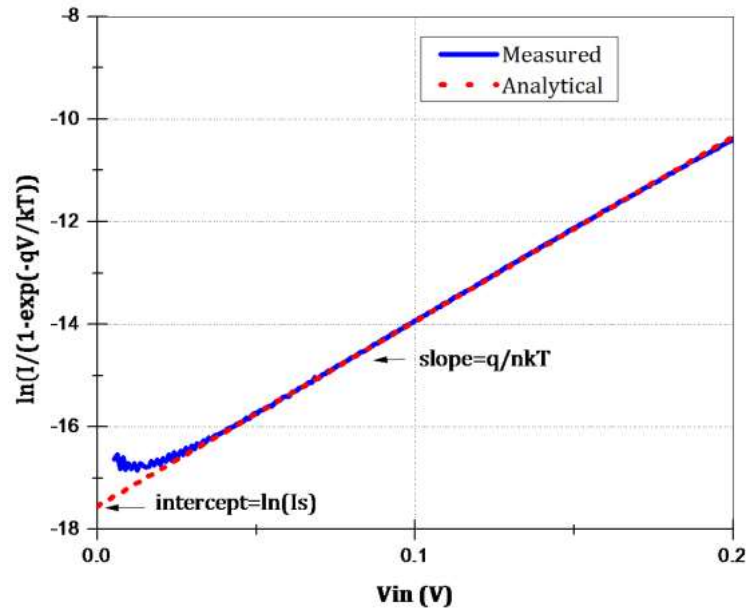


Fig. 3-3 $\ln\left(\frac{I}{1 - e^{-qV/kT}}\right)$ versus V_{in} for diode HSMS-2860

b. **Extraction of R_s**

Fig. 3-4 shows the measured and analytical curve of the diode HSMS-2860 at higher V_{in} . The extracted R_s is 4.9Ω .

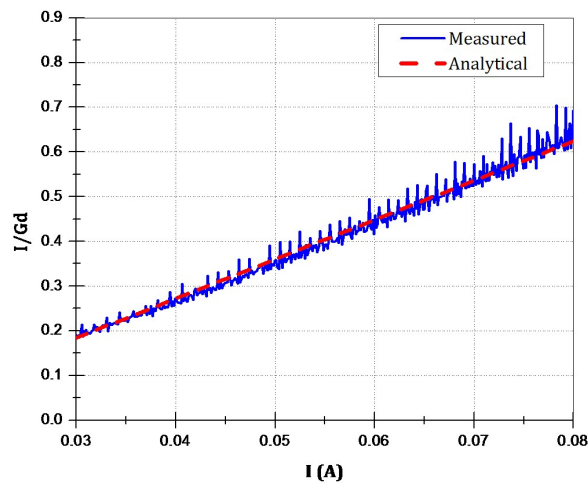


Fig. 3-4 $\frac{I}{G_d}$ versus current I for diode HSMS-2860

c. **Extraction of R_j**

The junction resistance R_j can be determined by (3.2), so from the I-V curve of the diode, we obtain Fig. 3-5.

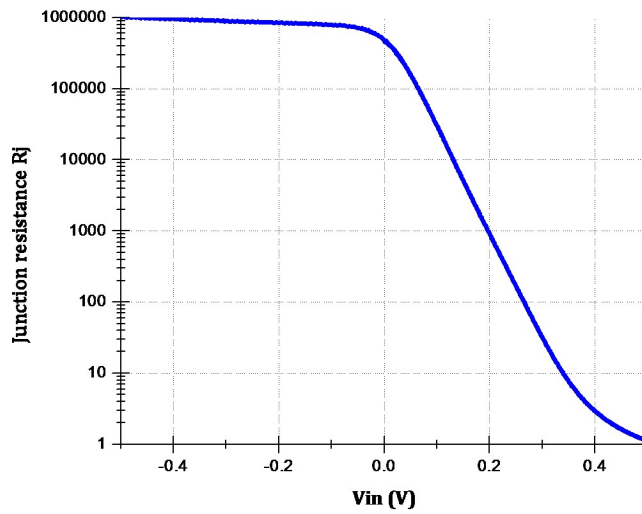


Fig. 3-5 Junction resistance R_j versus voltage bias V_{in} for diode HSMS-2860 (from measured data).

Three Schottky diodes used to extract the parameters are SMS-7630, HSMS-2860 and HSMS-285C. The extracted parameters of three diodes are provided in Table 3-1.

Table 3-1 Extracted parameters from the measurement in comparison with nominal values provided in the device's datasheet

Parameters		SMS 7630 079LF		HSMS 2860		HSMS 285C	
		Nominal	Extracted	Nominal	Extracted	Nominal	Extracted
Reverse saturation current	$I_S(A)$	5e-6	4.2e-6	5e-8	2.63e-8	3e-6	3.2e-6
Series resistance	$R_S(\Omega)$	20	36.5	6	4.9	25	45
Ideality factor	n	1.05	1.15	1.08	1.145	1.06	1.14
Junction resistance (zero bias)	$R_{j0}(\Omega)$		6922		466039		9044
Zero bias junction capacitance	C_{j0} (pF)	0.14		0.18		0.18	
Bias voltage	$V_{j0}(V)$	0.34		0.65		0.35	
Typical capacitance	C_p (pF)	0.3		0.3		0.3	
Series inductance	L_s (nH)	0.7		-		-	
Reverse resistance	$R_{rev}(\Omega)$	5000		-		-	
Transit time	$TT(s)$	1e-11		-		-	
Grading coefficient	M	0.4		-		0.5	
Breakdown voltage	Bv (V)	2		7		3.8	
Current at breakdown voltage	I_{bv} (A)	1e-4		1e-5		3e-4	

d. Discussion

Using the extracted parameters to simulate the diode model, we compare the provided I-V characteristics with the measured one (Fig. 3-6 and Fig. 3-7).

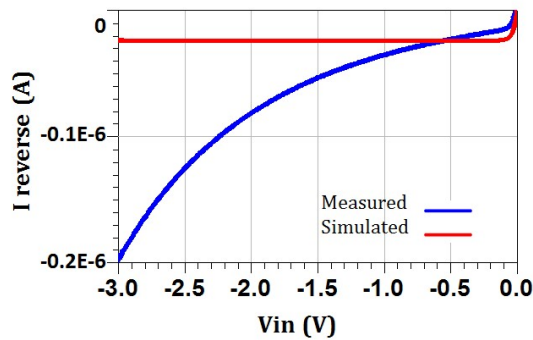


Fig. 3-6 Measured and simulated current in reverse bias of diode HSMS 2860

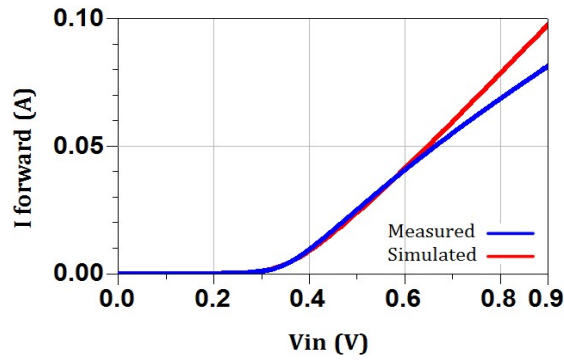


Fig. 3-7 Measured and simulated current in forward bias of diode HSMS 2860

A clear difference between model and experiment is observed. All the parameters have been extracted by analytical methods, based on diode law equation (3.1) and its derivation. However, this equation says nothing about the possibility of a reverse bias breakdown as well as the parasitic parameters of the device packages. There are effects that have not been covered by this standard SPICE diode model such as recombination effects at low forward bias and reverse off-state current between 0 V and breakdown voltage. In some cases, too many parameters are determined simultaneously, which can cause erroneous values. In fact, the parasitic parameters of the devices from packaging and mounting position in the circuit have a vital role and may significantly affect the performances. Therefore, it is necessary to develop a parameter extraction method that can describe all the important physical parameters and can be used for physical model based simulation.

3.1.3 Proposed physical-based model

In order to have an accurate diode model, we applied the model developed by Franz Sischka [119] by cascading the basic model into a sub-circuit.

a. DC forward modeling

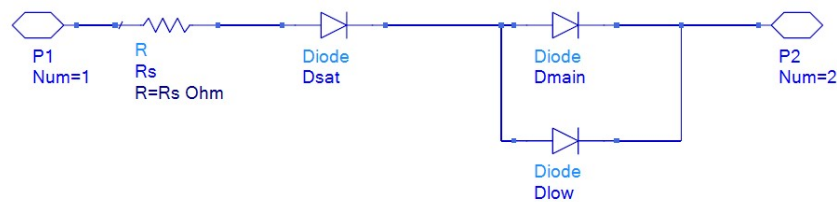


Fig. 3-8 Diode model after step #1, “DC forward bias modeling”

The DC forward modeling of the diode is presented in Fig. 3-8. This modeling process can be explained as follow. When applying the DC forward bias, the current of the diode has three different behaviors at different levels of applied voltages: At lowest DC bias, modeling by a low-voltage diode, D_{low} , I_S value and ideality factor n of this diode is defined by (3.6) as described above. The semi-log scale of current is linear as function of the low DC bias.

- At higher DC bias, the diode D_{low} cannot predict enough current through the diode. At the same bias voltage, the current is considerably larger than the current predicted by the previous linear equation. The semi-log scale of current is once again linear as function of DC bias and therefore can be modeled by a main diode, D_{main} , with particular I_S and ideality factor n . This main diode D_{main} is placed in parallel to D_{low} . In case the current of D_{main} is smaller than the current in the previous linear equation, the main diode is placed in series with D_{low} .
- Beyond diode threshold voltage, the diode functions in the ohmic diode region. There is an additional voltage drop at the same bias current, which means the presence of ohmic series resistor R_s .
- At the transition range between square-law region and saturation region, another saturation diode, D_{sat} , is added in order to improve the curve fitting.

Each diode (D_{low} , D_{main} , D_{sat}) is defined only by its independent saturation current I_S and ideality factor n . By measuring I-V characteristics in DC forward bias, we can extract these parameters for the model. Fig. 3-9 shows the results of simulated and measured current in DC forward bias using the proposed model. Results show a better fitting and the deviation is very small at a lower voltage.

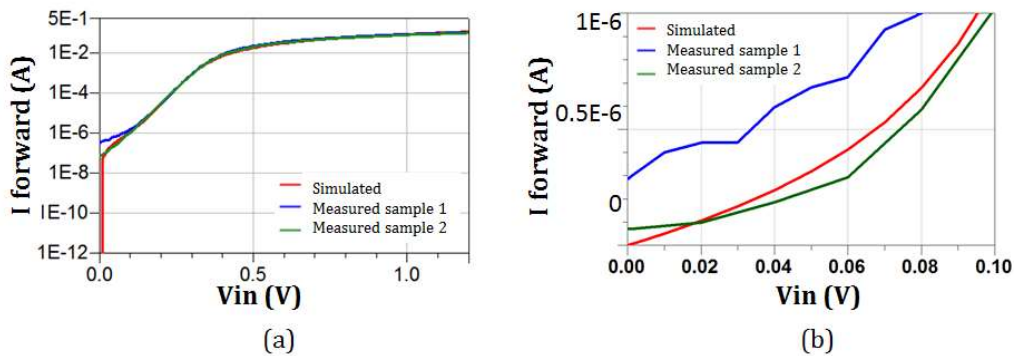


Fig. 3-9 Simulated and measured current in DC forward bias of diode HSMS 2860 (a) from 0 to 1.2V; (b) zooming from 0 to 0.1 V

b. DC reverse modeling

When applying the DC reverse bias, the current of the diode is limited by the constant reverse leakage current I_S and the reverse breakdown. Therefore, to model the reverse leakage more precisely, a reverse diode, D_{rev} and a reverse resistor, R_{rev} are added to the model sub-circuit (Fig. 3-10). The reverse resistor R_{rev} limits the current at the higher reverse voltage.

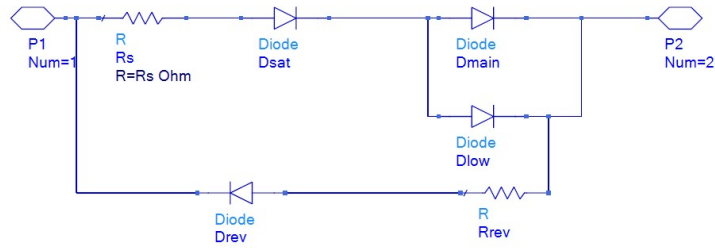


Fig. 3-10 Diode model after step #2, "DC reverse model"

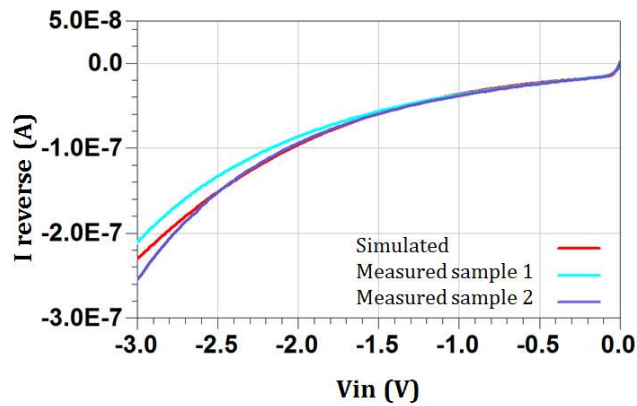


Fig. 3-11 Simulated and measured current in DC reverse bias of diode HSMS 2860

Fig. 3-11 shows the results of simulated and measured current in DC reverse bias using the proposed model, which is more accurate than the previous one. The measured current at reverse voltage has the same order of magnitude (about $2e-7$ A) in both simulated and different measured samples. It can be noted that the measurements were realized by HP4156B Precision Semiconductor Parameter Analyzer whose resolution is 1 fA and 0.2 mV.

Repeated DC forward and reverse measurements were conducted for 10 diodes and the statistical distribution measurements of for 10 diodes gives the very similar results and variance of samples is negligible.

c. C-V modeling

The capacitance of the Schottky diode is the key factor for evaluation of the performance of the rectifier. In order to model the capacitive effect of the diode, the C-V measurements need to be carried out. By increasing the DC bias from negative to positive, the diode schematic change from a mainly parallel schematic (R_j with C_j) to series resistor R_S alone.

An Impedance Analyzer delivers the measured C-V characteristics, normally by conversion into an "RC in parallel" or "RC in series" model. Then all the parameters C_{j0} , C_p , V_j and M are defined by (3.9). This assumption neglects the series resistor R_S and neglects capacitor loss (tangents-delta) represented by R_{tanD} . This can be surpassed by measuring the impedance of the device at low frequency and using Spice schematic to extract all the parameters.

To model the capacitance effect and the capacitor loss, the C-V model of a diode D_{C_V} in series with R_{tanD} is added to the model, in parallel with main static diode model (Fig. 3-12). D_{C_V} diode represents the parameters C_{j0} , V_{j0} and M .

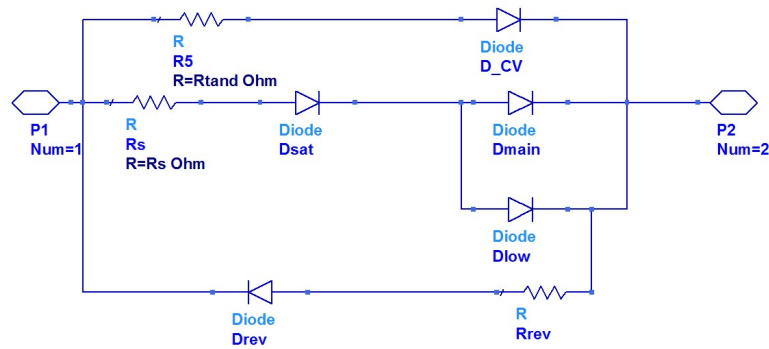


Fig. 3-12 Diode model after step #3, "C-V model"

While increasing DC bias voltage, R_j drops from infinity to 0Ω and C_j is negligible in the forward-biased case. The resistance when the diode is fully ON is the series resistor R_s .

C-V characteristics measurements involve the application of DC bias voltage across the capacitor while making the measurements with an AC signal. The AC frequencies normally vary from 10 kHz to 10 MHz. The bias voltage drives the device from its accumulation region into the depletion region and then inversion [120]. The detail test set-up is described in [120]. The total capacitance of the DUT is calculated by measuring AC current, AC voltage, and the impedance phase angle between them. However, the test is not accurate in the case of low capacitance measurements (range of femtofarads, which is the case of the diode total capacitance). That was not to mention the instrument connections, leaky capacitance measurement, and parameter extraction itself.

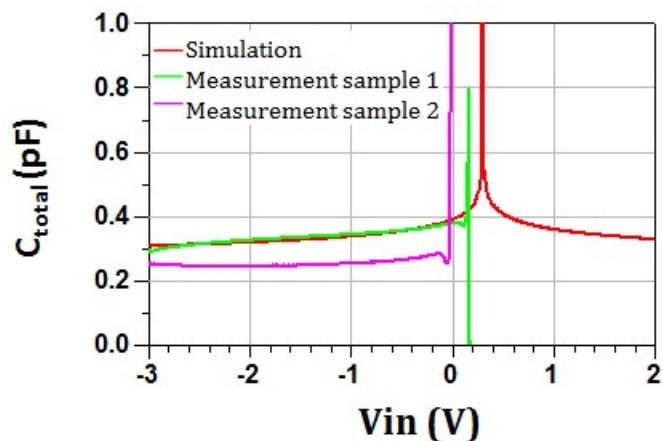


Fig. 3-13 Total capacitance versus input voltage of diode HSMS2860

The measurements were realized by LCR meter Agilent E4980A, with C resolution under 25 fF. Using a parallel R-C circuit model, we are able to measure the parallel capacitance, considered as

the total capacitance of the diode. The measured results (Fig. 3-13) show a rapid increase in the apparent total capacitance around 0-0.1 V, instead of the junction threshold voltage of the diode as stated in theory, based on (3.9). This can be explained as when a forward bias is applied to the diode, the junction conductance will begin to shunt the junction capacitance and reduce the overall quality factor. Both package inductance L_s and package capacitance C_p will also affect the 'Q' factor [111]. Therefore, the diode model does not fall into either parallel or series R-L-C circuit model as used in conventional measurement and C_{total} can be obtained only at low or negative bias since the junction is fully depleted at zero bias.

Observing and comparing measurements, other issues are involved as the fabrication variability and the experimental accuracy. Accuracy comes from many factors such as soldering or calibration. The variation of C_{total} has the variation of 15% throughout 10 diodes measurements. This parameter has the important role for rectifier design, which will be analyzed in more detail below.

d. *S-parameter modeling*

After extracting parameters from C-V characteristics, the capacitance between anode and cathode of diode including package capacitance has been measured. However, the parasitic capacitances from pad edge of anode to ground (C_{ga}) and cathode to ground (C_{gc}) have not been taken into account (Fig. 3-14). The S-parameter modeling is hence used to consider these parameters.

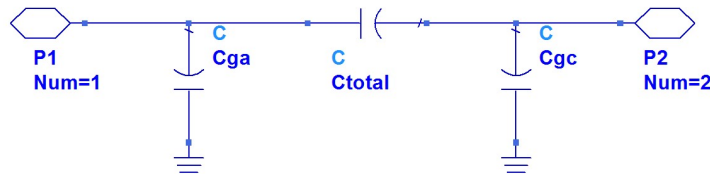


Fig. 3-14 Diode model at DC-OFF State (unbiased)

Two types of measurements are available: DC-Off state to extract parasitic capacitance and DC-On state to extract the series inductor.

DC-OFF State: At lower microwave frequencies from 0.5 to 4 GHz, and when the diode is not yet conducting (low power, zero-bias), the equivalent circuit of the diode can be reduced as a π -network (Fig. 3-14) [121]. The magnitude of the transmission coefficient S_{21} is dependent only on the value of the C_{total} . By fitting the measured values of the S-parameters to calculated ones, an accurate estimate for C_{total} , C_{ga} and C_{gc} can be extracted (Fig. 3-15).

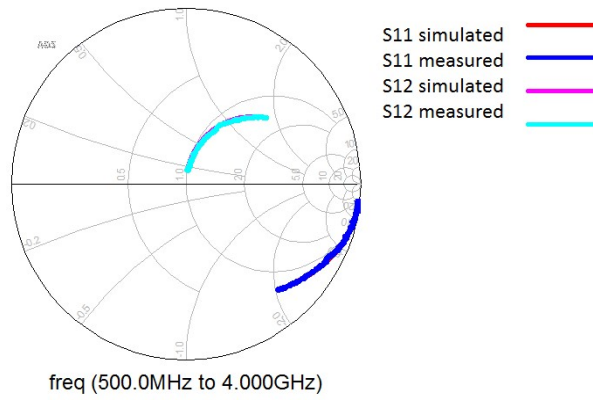


Fig. 3-15 Simulated and measured S-parameters DC-Off state of diode HSMS2850

DC-ON State: Applying a reverse-biased voltage, the value of C_{total} as a function of the input voltage can be determined and then compared to C-V modeling. C_{total} obtained from S-parameters exhibits an increased value versus frequency. This can be explained by the presence of a series inductor. This inductor L_s in series with the resistor R_s represents the parasitic inductance of packaging. Let the S-parameters trespass the x-axis in the Smith chart, hence L_s can be deduced from the measurement of S-parameters (Fig. 3-16).

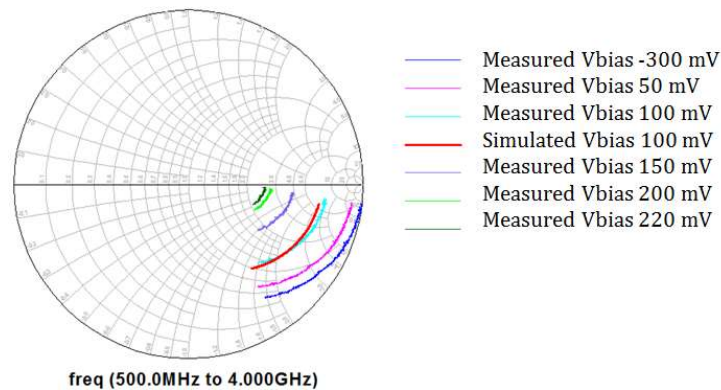


Fig. 3-16 Simulated and measured S-parameters (S11) DC-ON State of diode HSMS2850

e. **Proposed model**

In this section, the characterization and parameter extraction of a zero-bias Schottky diode over 0.5-4 GHz are presented. This procedure extracts the parameters in a step-by-step process by using analytical model together with the physical-based model (Fig. 3-18). The physical parameters in the model of three different types of the diode (Fig. 3-17) are extracted (Table 3-2).

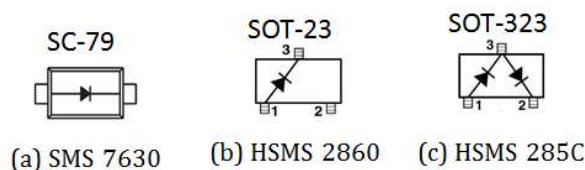


Fig. 3-17 Three different types of diode packaging

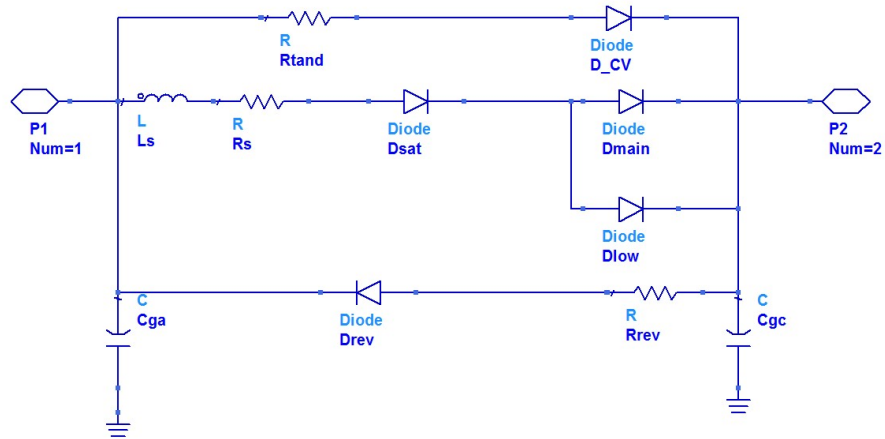


Fig. 3-18 Physical-based diode model, compatible with ADS

Table 3-2 Extracted parameters of 3 different diodes

Element	Parameter	SMS 7630	HSMS 2860	HSMS 285C
Dmain	Is (A)	4.06e-6	1.5e-8	3.51e-6
	n	1.06	1.05	1.1
Dlow	Is (A)		1e-6	2.5e-7
	n		1	5.3
Dsat	Is (A)	6.1e-3	0.85	0.02
	n	0.1	0.89	0.5
Drev	Is (A)	9.6e-6	1.01e-8	3.8e-6
	n	59	33	33
D_CV	Cj0 (pF)	0.14	0.15	0.20
	Vj0 (V)	0.35	0.45	0.35
	M	0.06	0.04	0.06
	Is	1e-25	1e-25	1e-25
	n	2.22	1.8	2.20
Cp (pF)		0.12-0.16	0.11-0.17	0.05-0.10
Rs (Ω)		36.8	7	42
Ls (nH)		0.7	0.7	0.6
Rrev(Ω)		1.3e4	1.7e6	9e4
Rtand(Ω)		0.3	0.65	0.3
Cga (pF)		0.020	0.29	0.11
Cgc (pF)		0.17	0.29	0.09

Using this proposed model with extracted parameters, the rectifier circuit will be designed in the next section.

3.2 Rectifier to combine different sources of energy

The level of electromagnetic power available in ambience is very low and it is necessary to increase the overall RF energy harvested efficiency. In order to harvest simultaneously energy from separated frequency bands and sources, solutions of the rectifier to combine different sources have been analyzed. There are two types of source combination: energy addition at RF level and/or energy addition at DC level.

3.2.1 Energy addition at RF level using a diplexer

A diplexer is a key component in an RF front end of multi-band communication systems. Consequently, a great number of studies have been carried out specifically to improve a high isolation between bands of frequency for improving the performances of communication[122]–[128]. Diplexers are generally designed by combining two filters with an additional matching circuit such as T-junction or Y-junction[122], [123]. Many methods have been explored to eliminate this matching circuit, allowing a reduction in size, like a short strip in conjunction with mutual loading effect in [124][125], stepped-impedance cross-structure (SICS)[126] or composite right/left handed (CRLH) quarter-wave resonators [127]. However, from an energy harvesting perspective, the most important specification of a diplexer is a low insertion loss in order to maximize the energy received at each frequency. The previously mentioned diplexers do not provide sufficiently low insertion loss (less than 0.5 dB) at the desired frequency within a compact size.

To eliminate the high loss in microstrip line, some studies have introduced other techniques using low-loss mediums such as the suspended strip line (SSL) [128]. Although this technique requires an increased fabrication effort, it is not compliant for integration into compact rectenna circuits, not to talk about embedding in packaging.

We propose a novel compact and very low loss, high selectivity microstrip diplexer based on the combination of two matching band-stop filters, designed for the most available frequency bands for RF energy harvesting applications: Global System for 1800 MHz Mobile communications (GSM) frequency and 2.45 GHz Wireless local area network (WLAN) frequency. By matching the pass-through frequency in each filter, the insertion loss becomes very low, thus enhancing the performances of the diplexer. The method for matching and miniaturizing the T-junction is also presented.

a. *Band-stop filter design*

The diplexer is a three ports circuit with two band-stop filters at two center frequencies, 1800 MHz (f_1) and 2.45 GHz (f_2). A junction joins both filters to a common port. Each filter stops one frequency band and allows the other band to pass through. The Rogers 4003 substrate with a

thickness of 0.813 mm, a relative permittivity of 3.55 and a loss tangent of 0.0027 is used for the design and the fabrication. The proposed band-stop filter (Fig. 3-19) consists of a microstrip feeding line and the stepped impedance circuit coupled by an interdigital capacitor. The principle of this rejection filter is to place the resonator in parallel with the main transmission line. When the resonator enters the appropriate resonance, it is equivalent to a short circuit for the signals at the desired rejection frequency.

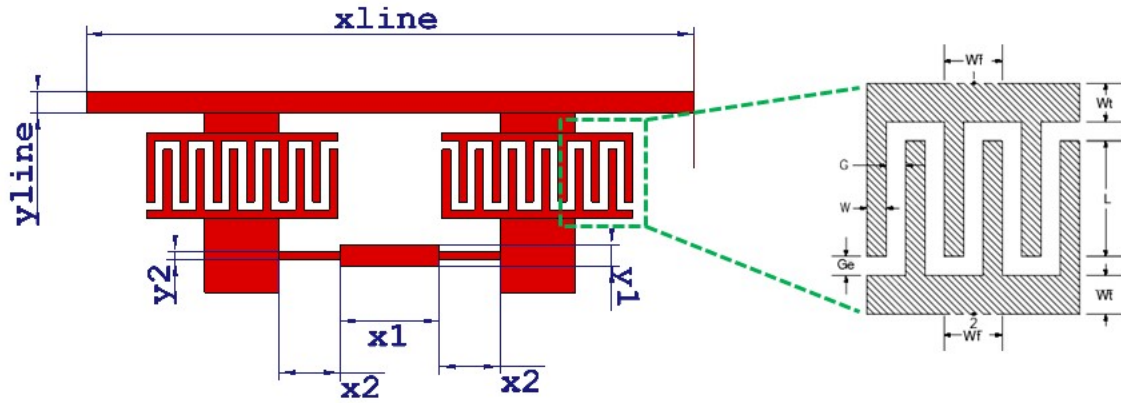


Fig. 3-19 Proposed matching band-stop filter

Table 3-3 Parameters of two filters

	Filter 1	Filter 2		Filter 1	Filter 2
Symbol	Value (mm)	Value (mm)	Symbol	Value (mm)	Value (mm)
xline	20	25	G	0.3	0.3
yline	0.7	0.3	Ge	0.3	0.3
x1	3.9	3.1	W	0.3	0.3
x2	2.2	3.3	Wf	2.8	4.6
y1	0.7	0.6	Wt	0.3	0.3
y2	0.3	0.9	N	6	6

The filter uses interdigital-coupled lines instead of gap-capacitor or quarter-wave coupling in order to achieve size reduction, low leakage, and suppression of filtering harmonic resonance [129]. The interdigital capacitor is controlled by the dimension parameters (G , Ge , W , Wf , Wt) and number of finger pairs (N). The required zeros transmission are introduced using a stepped-impedance circuit formed by a high impedance line along with low-impedance lines, realizing a parallel resonant circuit. The cut-off frequency is obtained by tuning the dimensions of these lines, namely ($x1$, $x2$, $y1$, $y2$) and the size of the interdigital capacitor.

The matching frequency, in which energy passes, can be adjusted by changing the width ($yline$) and the length ($xline$) of the transmission line between the input and the output of the filter,

without changing the stop-band frequency of the filter. As a result, the rejection frequency and resonant frequency can be controlled independently.

After applying the design and optimization process, the simulation results are pictured in Fig. 3-20. Filter 1 has a stopband centered at 1800 MHz, a matching frequency at 2.45 GHz and filter 2 has the stopband centered at 2.45 GHz and a matching frequency at 1800 MHz. The design parameters of these two filters are described in Table 3-3.

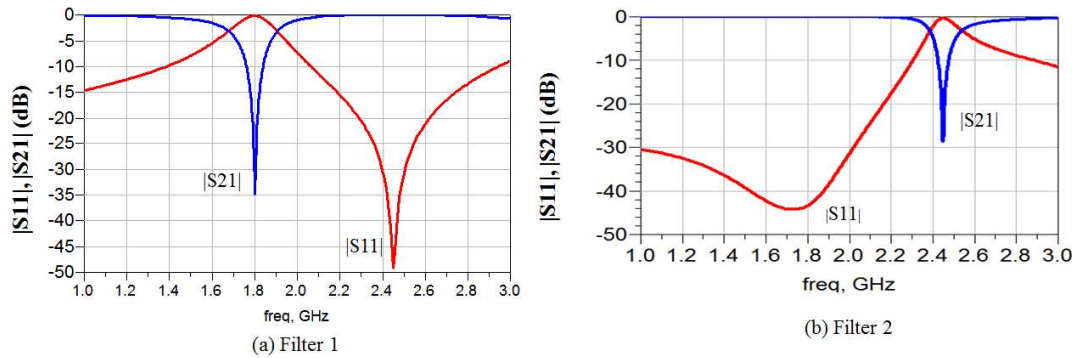


Fig. 3-20 Simulation results of both filters as described in Fig. 3-19

b. **Diplexer design:**

To form the diplexer, a transmission line T-junction has been placed to connect both proposed filters. Since the filter 2 is equivalent to a short-circuit at the frequency f_2 (Fig. 3-21), the length of the transmission line from the common input port to filter 2 (t_2) corresponds to a quarter-wave at f_2 in order to ensure an open circuit at the frequency f_2 at common port. On the other hand, the length of the transmission line from the common port to filter 1 (t_1) corresponds to a quarter-wave at f_1 .

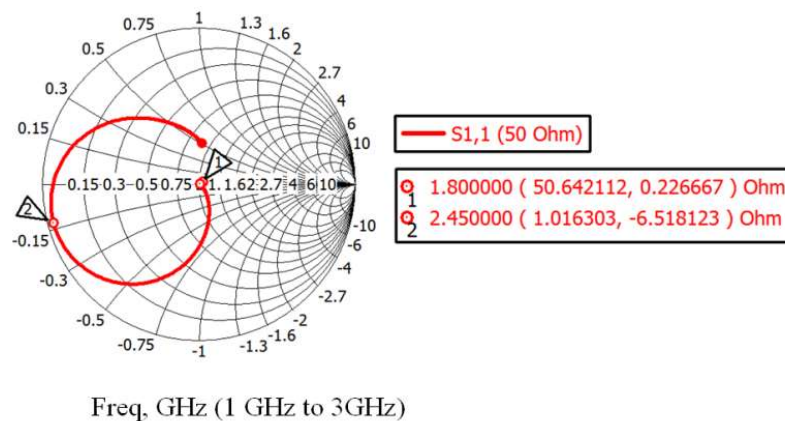


Fig. 3-21 Simulated impedance of Filter 2

After joining the two filters via the junction (Fig. 3-22a), under the influences of the other filter and the T-junction itself, the cut-off frequencies and the desired matching frequencies of both filters are altered. Some minor modifications of the filter dimensions are introduced to

compensate these effects. c as in Fig. 3-22b, while maintaining the necessary distance between elements for normal operation of the diplexer.

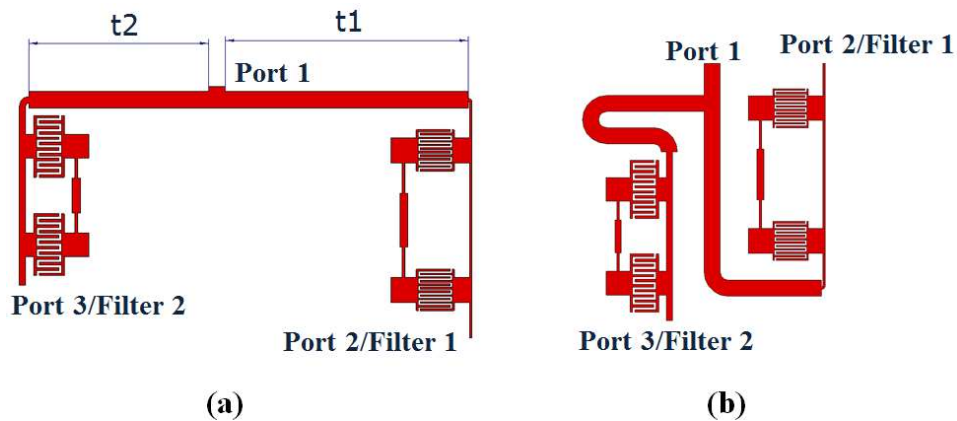


Fig. 3-22 Geometry of the diplexer: (a) Straight topology; (b) Meander topology

The circuit model simulation and full-wave simulation are performed using Agilent ADS software and Momentum 2D simulation in RF mode. In the circuit model simulation, the electric and magnetic coupling between the physical elements was not considered. Results suggest these influences are rather significant and the insertion loss at the two desired frequency bands increases compared to single filters due to losses in the transmission line from the common port.

c. Fabrication and measurement

The two filters and the diplexer are fabricated on Rogers 4003 substrate. Fig. 3-23 shows the picture of the prototype filters and diplexer. The total size of the diplexer is $26 \times 30 \text{ mm}^2$, equivalent to $0.29 \lambda_g \times 0.33 \lambda_g$ where λ_g is the guided wavelength at the lowest frequency (f_1).

Input and output lines of the diplexer are soldered to subminiature A (SMA) connectors. They are characterized using VNA Agilent 8510C. The measured results for the filters are confronted to the simulated ones. Good agreement is obtained between simulation and measurement results for the diplexer.

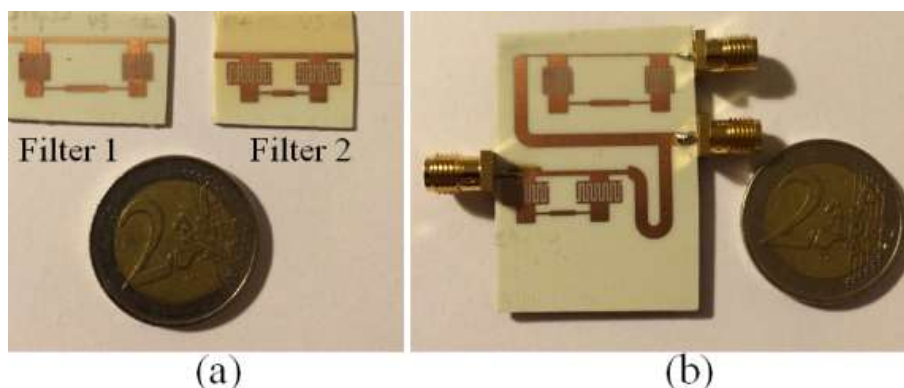


Fig. 3-23 Pictures of the fabricated circuits: (a) Filters; (b) Diplexer

Fig. 3-24 shows the simulated and measured reflection coefficient of the diplexer at the common port (Port 1). This port will be connected to a multiband antenna that is operated at frequency bands f_1 and f_2 . The results show good impedance matching for these two bands.

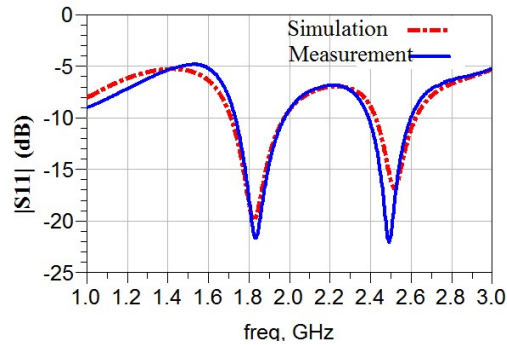


Fig. 3-24 Simulated and measured reflection coefficient at common port

The simulated and measured insertion losses (magnitude of S_{21} and S_{31}) for the two bands around 1.8 GHz and 2.45 GHz are 0.40 dB and 0.42 dB respectively, what include the losses from the SMA connectors (Fig. 3-25).

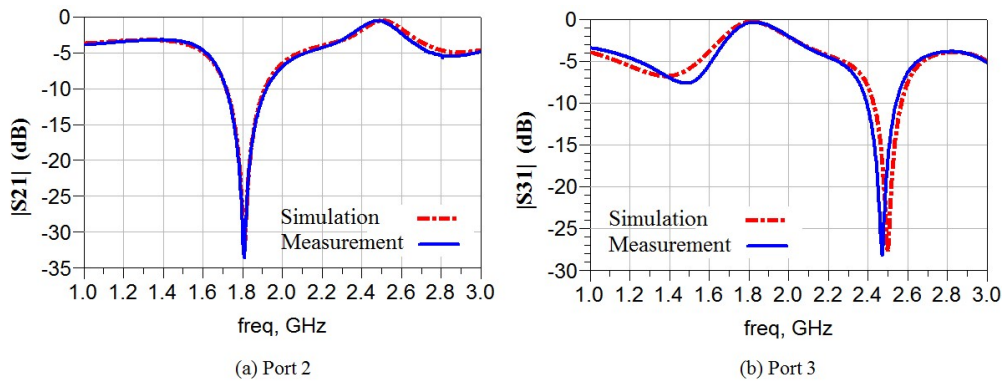


Fig. 3-25 Simulated and measured transmission coefficient at Port 2 and Port 3

The rejected band of each channel filter is better than 25 dB. The measured return losses in both frequency bands are better than 20 dB and agree well with simulation (Fig. 3-26).

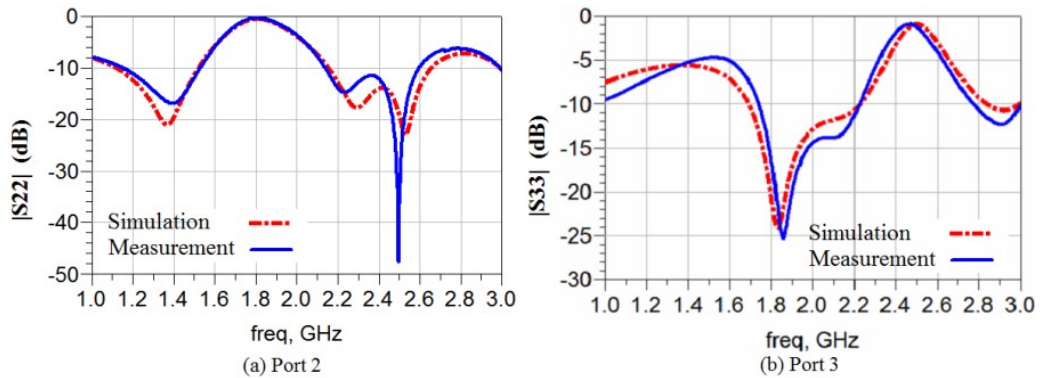


Fig. 3-26 Simulated and measured reflection coefficient at Port 2 and Port 3

Table 3-4 provides a comparison of performance between the proposed diplexer and other designs in literature. It is found that the proposed diplexer offers a better trade-off between insertion losses and size in comparison with similar published studies. These specifications are very important especially in the case of RF energy harvesting.

Table 3-4 Comparison between proposed diplexer and references

	Insertion loss (dB)		Size ($\lambda_g \times \lambda_g$)
	Channel 1	Channel 2	
This work	0.40 at 1.8 GHz	0.42 at 2.45 GHz	0.29 x 0.33
[126]	0.32 at 2.9 GHz	0.33 at 5.8 GHz	0.64 x 0.38
[128]	0.4 at 0.9 GHz	0.5 at 1.8 GHz	0.29 x 0.29
[124]	0.5 at 1.575 GHz	0.5 at 4 GHz	0.156 x 0.107
[125]	0.25 at 1.5 GHz	2.42 at 2.4 GHz	1.69 x 1.03
[127]	1.34 at 1.8 GHz	1.44 at 2.35 GHz	0.12 x 0.23
[122]	1.95 at 3.5 GHz	1.97 at 4 GHz	1.13 x 0.92
[123]	2.15 at 1.8 GHz	2.17 at 2.45 GHz	0.13x 0.2

d. Conclusion

This diplexer forms by matching two band-stop filters, using an interdigital capacitor and stepped impedance resonator has been explored. The advantages of the proposed microstrip diplexer are a reduced insertion loss of 0.4 dB, an improved selectivity, further compact sizing, and a simplified fabrication and integration in the circuit for energy harvesting.

3.2.2 Energy addition at DC level

The advantage of energy addition at DC level is the possibility to combine signals of different frequencies, different power levels and not necessarily in phase without complicating the combining circuit. In this section, we will present the design of simple rectifier at 2.45 GHz and then the design of 2-rectifiers, which are combined at DC level. For all the rectifiers developed in this part, the proposed Schottky diode model in the previous section is used in order to verify the extracted parameters.

The rectifiers have been designed using Agilent ADS software and Momentum in RF mode. The substrate for fabrication is Rogers 4003 with a thickness of 0.830 mm and loss tangent of 0.0027. The selection of the microwave substrate is done in such a way that the power losses are minimized. Usually, very thin substrates exhibit more losses than thicker ones when the dielectric constant remains the same [118].

a. Design of rectifier with 1-input at 2.45GHz

A single stage voltage-doubler rectifier is developed using Schottky diode HSMS-2850. In this topology, two diodes are mounted one in series and one in parallel, allowing producing a larger

voltage at the output (Fig. 3-27). During the first half-cycle of the input voltage, D1 will be forward bias and C1 will be charged to the peak voltage. During the following positive half cycle of the input voltage, D1 will be reversed biased and will not conduct current, the voltage across C1 will remain unchanged and will add on to the input voltage during this half cycle. Since D2 is forward biased, C2 will be charged to double voltage [37].

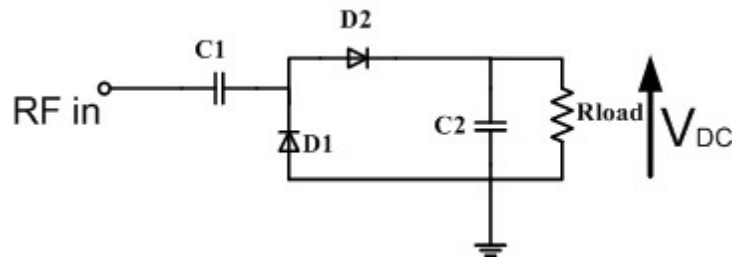


Fig. 3-27 Schematic of single stage voltage-doubler rectifier

Diodes have been simulated using the proposed non-linear models. The design has also used passive components (capacitors and resistors) and these components have parasitic elements that affect their behavior at high frequencies. These components are typically available as surface-mount technology (SMD) (Fig. 3-28). We found in literature many suggestions of modeling these components, which do take into account their temperature-dependence, their variation as function of frequency, and their parasitic components.

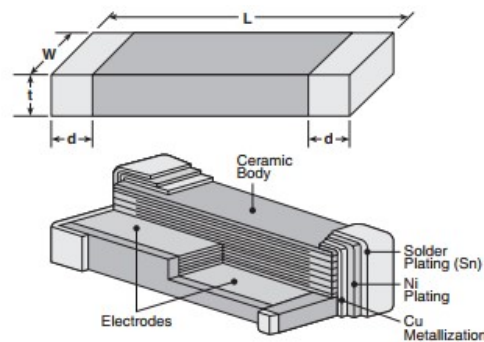


Fig. 3-28 Dimensions and construction of an ceramic chip capacitor extracted from [130]

Fig. 3-29 shows the equivalent model of capacitor C described in [131], where ESR is the equivalent series resistor, ESL is the equivalent series inductor, R_p represents the insulation resistance or leakage resistance.

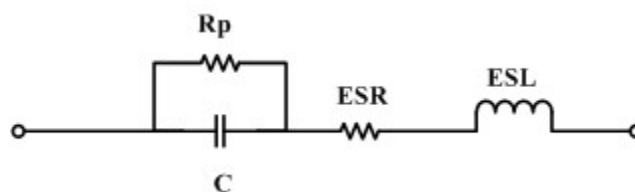


Fig. 3-29 Equivalent model of an SMD capacitor

The typical values of these parasitic elements for common packages are given in Table 3-5. The value of R_p is extremely high so it can be neglected in the following simulation. In general, while comparing between technologies, the ESR of NPO capacitor is smaller than the one of X7R capacitor. A difference of a factor of 4 to 10 is observed between these technologies for the same manufacturer. Nevertheless, there is no difference of ESR between components with the same electric value but different packaging. On the other hand, the typical ESL is provided by the manufacturer, and varies with different packaging.

Table 3-5 Typical values of parasitic elements of SMD capacitor ($C=1$ pF) at 25°C , 2.45 GHz

Package	Typical ESR (Ω)		Typical ESL (nH)	Typical R_p ($M\Omega$)	
	NPO	X7R		NPO	X7R
0402	0.06	0.4	0.5	10^7	10^6
0603	0.06	0.4	0.6	10^7	10^6
0805	0.06	0.4	0.8	10^7	10^6
1206	0.06	0.4	1.2	10^7	10^6

There exist many technologies for resistor component, but the component using thick film technology is widely used in printed circuit board. The resistive load utilized in this application operates at DC level; therefore, it is not affected by high-frequency factor. The simple but complete model of the resistor is given in Fig. 3-30 [131]. This model has a parasite capacitor, C_{pa} , which short-circuit the resistor R at high frequencies and a parasite inductor, L_{pa} . The typical values of these parasitic elements are given in Table 3-6.

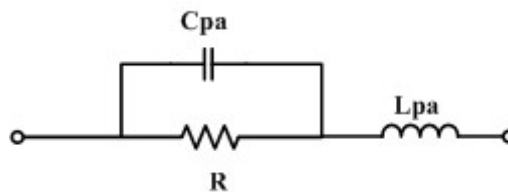


Fig. 3-30 Equivalent model of a thick film resistor

Table 3-6 Typical value of parasitic elements in thick film resistor

Package	Typical L_{pa} (nH)	Typical C_{pa} (pF)
0603	0.8	0.09
0805	0.8	0.05

The harmonic balance (HB) simulation tool from Agilent ADS was used to simulate the rectifier at different frequencies and input power levels. In this simulation, the source impedance represents the antenna's impedance, assuming 50Ω . The rectifying circuit, therefore, has to match with this impedance in order to deliver maximum power to the load.

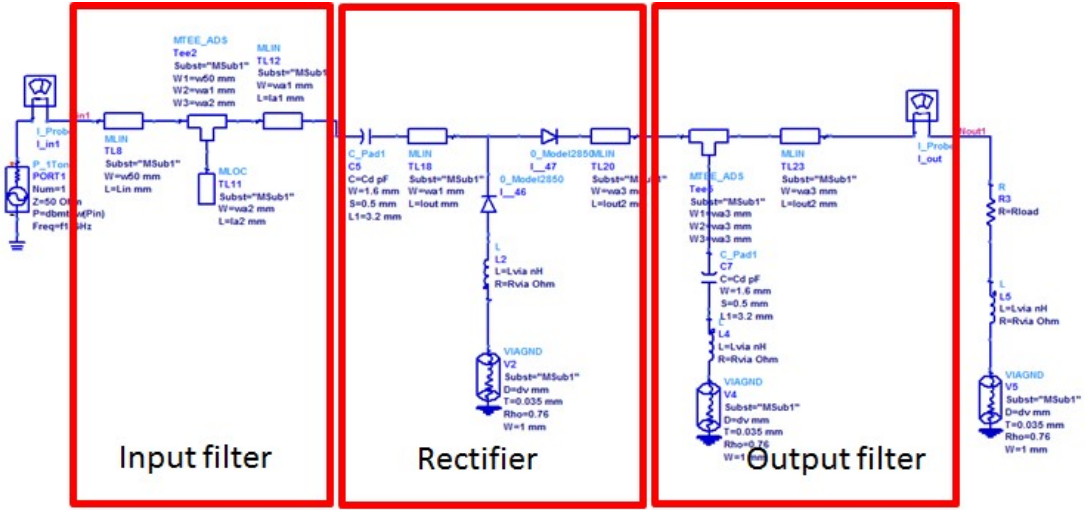


Fig. 3-31 Rectifier schematic for HB simulation

The impedance matching is realized by employing a simple open stub of microstrip with the length of $\lambda_g/4$, as shown in Fig. 3-31.

This circuit has three via holes in the substrate. The electrical behavior of these cylindrical via holes is purely inductive and resistive. In literature, authors present different methods to calculate the inductance and resistance values. In[132], the inductance L_{via} of a cylindrical via hole can be represented as the following equation:

$$L_{via} = \frac{\mu_0}{2\pi} \left[h \cdot \ln \left(\frac{h + \sqrt{r^2 + h^2}}{r} \right) + \frac{3}{2} \left(r - \sqrt{r^2 + h^2} \right) \right] \quad (3.10)$$

Where h is substrate thickness

r is the radius of the via hole

Calculating L_{via} using (3.10) with $r=0.4\text{mm}$ gives 0.03 nH . This value is taken into account when simulating the circuit.

The via resistance is highly dependent on fabrication processes and may be approximated as follows, taking into account the skin effect:

$$R_{via} = R_{DC} \sqrt{1 + \frac{f}{f_\delta}} \quad (3.11)$$

Where

$$f_\delta = \frac{1}{\pi \mu_0 \sigma t^2} \quad (3.12)$$

σ is conductivity in S/m

μ_0 is the permeability of free space = $4\pi \times 10^{-7} \text{NA}^{-2}$

f is frequency in Hz

t is the thickness of the conductor (m)

R_{DC} is the resistance at DC, around 0Ω and may be measured directly from the circuit.

At the frequency range from 0.5 GHz to 4 GHz, we can calculate $R_{\text{via}} \sim 10 \times R_{DC}$. With R_{DC} is very small and is proximity to 0, R_{via} can be considered equal to 0.

The rectifier is then optimized at an input power of -15 dBm and the co-simulation is realized by 2D Momentum simulation in order to take into account the coupling of microstrip lines. The load R_{load} has the value of 6800Ω . The circuit is fabricated using substrate Roger 4003 (Fig. 3-32).

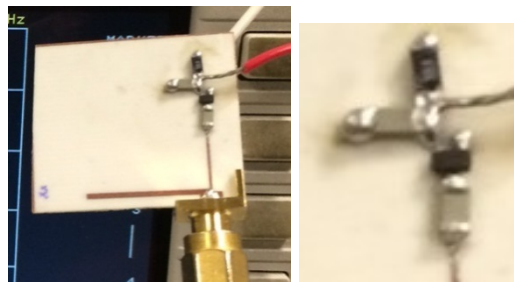


Fig. 3-32 Fabricated 1-input rectifier using diode HSMS 2850

Fig. 3-33 shows the comparison of efficiency between simulation and measurement. As noticed in section 3.1.3, while extracting the parasitic capacitance C_p of the diode, their values have varied about 15% around the average value. The variation of C_p between measurements can be observed and this value has significantly affected the RF-to-DC efficiency of the circuit. This leads to the difficulty of optimization process while taking into account the value of parasitic capacitance C_p .

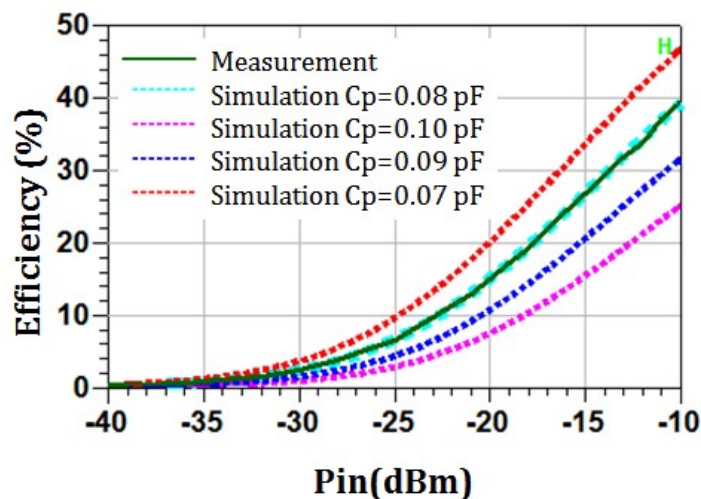


Fig. 3-33 Simulated and measured efficiencies of 1-input rectifier using diode HSMS2850 versus input power with $R_{\text{load}}=6800k\Omega$

b. Design of rectifier with two inputs at 2.45 GHz

Harvesting from multiple sources can be achieved by stacking several rectenna and adding the DC output voltages to the same load. In this approach, several rectifier topologies exist to combine DC voltage such as series connection, parallel connection and cascade connection [133].

In the case of only two inputs, the parallel configuration can be easily implemented (Fig. 3-34)

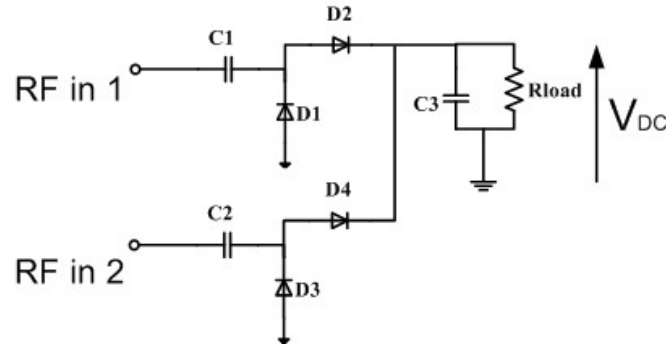


Fig. 3-34 Schematic of the two-input rectifier

The efficiency of each port η is calculated when there is only one source at one port with other source neutralized.

$$\eta_{1port} = \frac{P_{DC}}{P_{RF\ 1port}} \quad (3.13)$$

The total efficiency of the two-input rectifier when there are two sources simultaneously is calculated as follows:

$$\eta_{2port} = \frac{P_{DC}}{P_{RF\ port1} + P_{RF\ port2}} \quad (3.14)$$

The rectifier is optimized similarly to the 1-input rectifier and fabricated using substrate Rogers 4003 (Fig. 3-35), considering the two ports have the same level of input power and using parasitic capacitance $C_p=0.08$ pF. The efficiency of the circuit is shown in Fig. 3-36. The efficiency while two ports are excited similarly is equivalent to the efficiency while one port is excited. This means the topology is more effective compared to a one-input rectifier. However, the C_p value used for optimization process ($C_p=0.08$ pF) did not match the real C_p measured (about 0.06 pF). Therefore, the fabricated circuit did not reach the higher efficiency as simulated.

These results show that the parasitic capacitance has an important role in the diode model and the measurement of this value is needed when working with rectifier at very low incident input power.

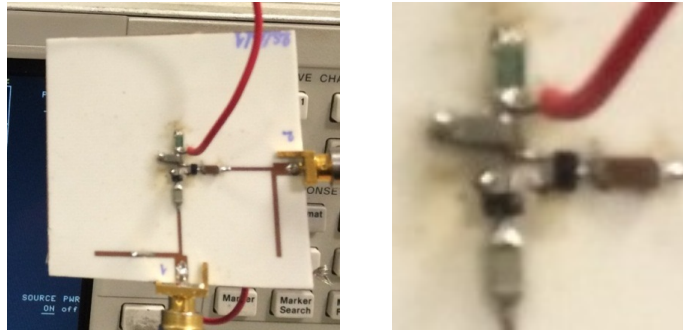


Fig. 3-35 Fabricated two-input rectifier

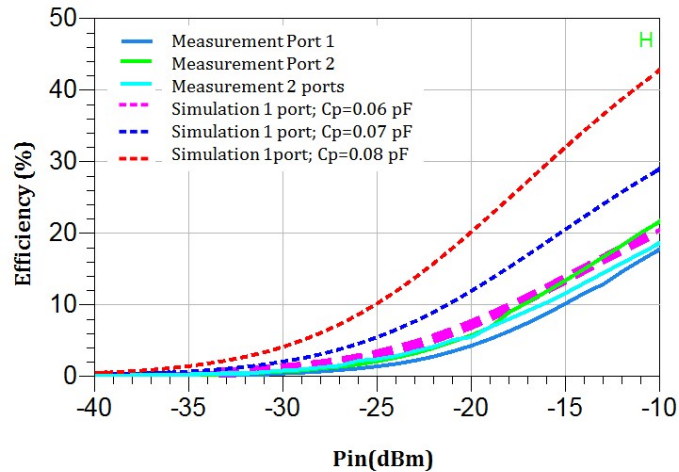


Fig. 3-36 Simulation and measurement efficiencies of rectifier versus input power using diode HSMS 2850

3.3 Conclusion

We have presented in this chapter the principle and the role of a rectifier circuit in energy harvesting system. The study focuses on the most important component of rectifying circuit at RF frequency, the Schottky diode. The methods of extracting parameters are discussed, by dissociating each element and their roles. Measurements have been performed in order to compare different models of the diode, also to take into account the real impact of the fabrication process and measurement process.

The behavior of the Schottky diode from 0.5 GHz to 4 GHz for several diode samples is analyzed. The simulation model as well as extracted parameters for three diodes: SMS7630, HSMS2850 and HSMS2860 are presented. This diode model is then utilized in designing rectifier circuit. Different configurations of the multi-source rectifier are proposed and developed in this chapter. In order to combine several sources into one circuit, two topologies of energy addition are presented, with the addition at RF level and DC level. In the effort of combining sources at RF level in order to increase the harvested power, a low loss diplexer that operates at 1800 MHz and 2.45 GHz was designed. The experimental results show that this diplexer has the best performance compared to others developed in the literature.

4. Global system and measurements

In the previous section, the antenna for RF energy harvesting and the rectifier circuit have been discussed. In this section, the complete circuit of rectenna will be discussed and characterized.

There are many challenges that the design process has to face, including the antenna requirement, rectifier requirement and the co-design of these two circuits as described in Fig. 4-1.

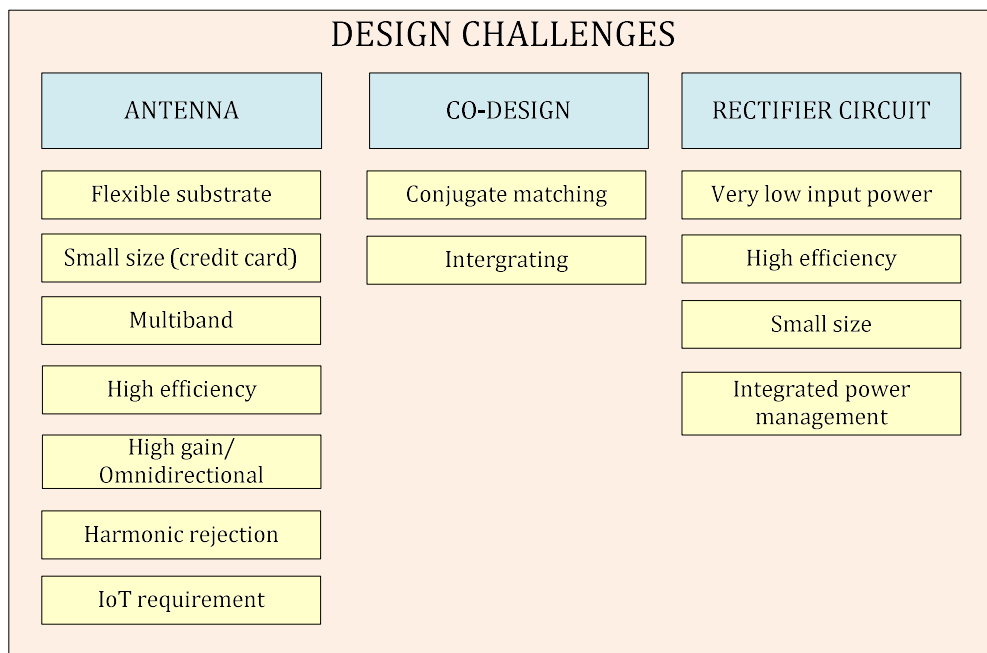


Fig. 4-1 Design challenges of the system.

This section will concentrate on the interface between antenna and rectifier in the condition of ambient RF energy (very low incident power). The complete solutions of combining sources for increasing harvested power on the flexible substrate are also proposed.

4.1 Co-design

In rectenna, the matching impedance is essential to assure the maximum power transfer between antenna and rectifier. The traditional 50- Ω impedance interface is not always optimal. Co-design allows reaching the complex conjugate matching without the need of a reference-matching network because the antenna is close to the rectifier and there is no wave propagation between the two elements, therefore it eliminates the loss and the noise that may occur in this network.

The objective of co-design is to define the optimum impedance in matching that provides the highest total efficiency, what completely depends on incident power, type of rectifier component

and operating frequency. Another issue is to choose the appropriate architecture of power management block to archive maximum harvested energy, corresponding to their architecture.

4.1.1 Impedance matching in co-design rectenna

By co-designing antenna-electronics interface, both parts share a common optimization target to improve the overall system performances. The choice of interface impedance plays an important role in the optimization of antenna systems in the receiving mode. The interface between antenna and rectifier circuit is shown in Fig. 4-2.

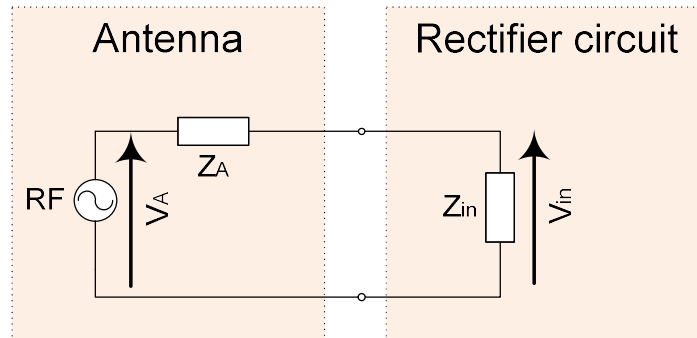


Fig. 4-2 Antenna- Rectifier circuit interface

Where Z_A : Impedance of antenna (Ω)

Z_{in} : Impedance of load (rectifier circuit) (Ω)

V_A : Induced voltage of antenna (V)

V_{in} : Input voltage of load circuit (V)

Fig. 4-2 shows a circuit with arbitrary source and load impedance, Z_A and Z_{in} , which may be complex.

The power delivered to the load is:

$$P_{\text{deliver}} = \frac{1}{2} \text{Re}\{V_{in} I_{in}^*\} = \frac{1}{2} |V_{in}|^2 \text{Re}\left\{\frac{1}{Z_{in}}\right\} = \frac{1}{2} |V_A|^2 \left|\frac{Z_{in}}{Z_{in} + Z_A}\right|^2 \text{Re}\left\{\frac{1}{Z_{in}}\right\} \quad (4.1)$$

Now let $Z_A = R_A + jX_A$ and $Z_{in} = R_{in} + jX_{in}$. (4.1) can be reduced to:

$$P_{\text{deliver}} = \frac{1}{2} |V_A|^2 \frac{R_{in}}{(R_{in} + R_A)^2 + (X_{in} + X_A)^2} \quad (4.2)$$

Where:

$$V_{in} = V_A \left|\frac{Z_{in}}{Z_{in} + Z_A}\right| \quad (4.3)$$

So

$$P_{\text{deliver}} = \frac{1}{2} |V_{\text{in}}|^2 \frac{R_{\text{in}}}{R_{\text{in}}^2 + X_{\text{in}}^2} \quad (4.4)$$

To maximize P_{deliver} , while assuming that V_A and Z_A are fixed, we differentiate (4.2) with respect to the real and imaginary parts of Z_{in} and we have:

$$R_A = R_{\text{in}} \text{ and } X_A = X_{\text{in}} \text{ or } Z_A = Z_{\text{in}}^*$$

According to the maximum power theorem, to achieve maximum power delivered to the load, we need have conjugate matching condition between the antenna and the circuit, and it's crucial that the reactive components cancel each other.

To calculate the P_{deliver} , we need to consider the antenna model in the receiving mode under conjugate matching. The power delivered to the load of an antenna depends on the effective antenna aperture, A_e , and is defined as:

$$A_e = \frac{\lambda^2 G}{4\pi} \quad (4.5)$$

where λ is the free-space wavelength of the radiation (m)

G is realized gain of the antenna (dBi).

In the condition of conjugate matching, the power delivered to the load, P_{deliver} , is related to the free-space power density, P_{av} , by the effective antenna aperture A_e through equation (4.6).

$$P_{\text{deliver}} = P_{\text{av}} A_e = P_{\text{av}} \frac{\lambda^2 G}{4\pi} \quad (4.6)$$

The two figures P_{av} and P_{deliver} are the incident power density and the power transferred to the load, respectively. From the study of the available power density of electromagnetic waves at the mobile phone and Wi-Fi frequencies in Chapter 1, we can estimate the power delivered to the rectifier circuit as given in Table 4-1, and considering the antenna gain is from 2 to 3 dBi.

Table 4-1 Calculated power delivered to the input of rectifier circuit

$f(\text{MHz})$	Median Power			Maximal Power		
	$P_{\text{av}} (\text{dBm}/\text{m}^2)$	$G(\text{dBi})$	$P_{\text{deliver}}(\mu\text{W})$	$P_{\text{av}} (\text{dBm}/\text{m}^2)$	$G(\text{dBi})$	$P_{\text{deliver}}(\mu\text{W})$
900	-15	2	0.44	4	4	44.34
1800	-15	2	0.11	4	4	11.08
2100	-15	2	0.08	4	4	8.14
2450	-10	2	0.32	5.8	4	9.06
2600	-12	2	0.11	4	4	5.31

Not all the power that is captured by the antenna is delivered to the load but it includes the part which is scattered and dissipated as heat by the antenna. The most that can be delivered to the

load is only half of the one captured and that is only under a conjugate matching and lossless transmission condition [88].

Using (4.2), the power delivered to the rectifier circuit is given by:

$$P_{\text{deliver}} = \frac{|V_A|^2}{8R_{\text{in}}} \quad (4.7)$$

While the captured power is:

$$P_{\text{captured}} = \frac{1}{2} V_A I_A^* = \frac{|V_A|^2}{4R_A} \quad (4.8)$$

Therefore, under conjugate matching, half of power captured by the antenna is delivered to the load R_{in} (rectifier circuit) and the other half is reradiated through R_r and dissipated as heat through R_l .

From (4.4), we can estimate the input voltage V_{in} for a given P_{deliver} calculated from Table 4-1

$$|V_{\text{in}}| = \sqrt{\frac{2P_{\text{deliver}}(R_{\text{in}}^2 + X_{\text{in}}^2)}{R_{\text{in}}}} \quad (4.9)$$

From (4.9), in order to increase V_{in} to overcome the threshold voltage of the rectifier circuit, we have to choose the appropriate value of the conjugate impedance $R_{\text{in}} + jX_{\text{in}}(\Omega)$.

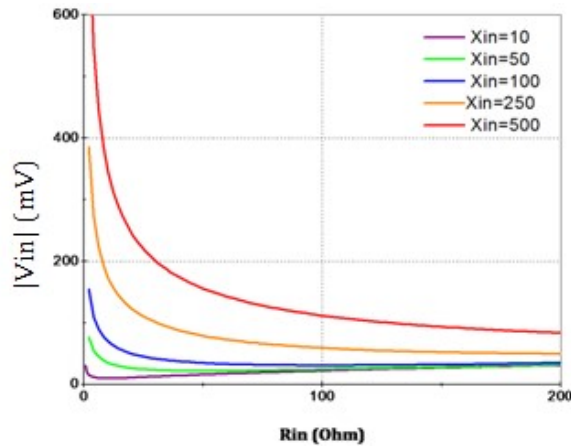


Fig. 4-3 Input voltage versus resistance R_{in} with $P_{\text{deliver}} = 2.4 \mu W$

4.1.2 Choosing matching impedance

Observing the plot of V_{in} in function of R_{in} for a given P_{deliver} (Fig. 4-3), we can note that the voltage can be maximized by either decreasing or increasing R_{in} and it reaches its minimum when $R_{\text{in}} = X_{\text{in}}$. In [43] the authors have proposed a method to choose the matching impedance by determining the required ratio of the real and imaginary part of the load impedance. The region where $R_{\text{in}} \ll X_{\text{in}}$ has high-quality factor Q at the expense of bandwidth. Voltages increase at a higher rate and the output voltage can be passively boosted by the presence of the reactance. In

contrast in the region where $R_{in} \gg X_{in}$ or the antenna impedance is purely real, the antenna has a very low Q and then can be exploited in the design of the wideband application.

If the conjugate impedance was chosen as matching impedance, the matching circuit can be eliminated in the final circuit. The input impedance can be estimated from the diode impedance at the desired frequency and input power.

Using the diode model, which was created in Chapter 3, the input impedance of one of the studied diode can be evaluated using ADS (Fig. 4-4).

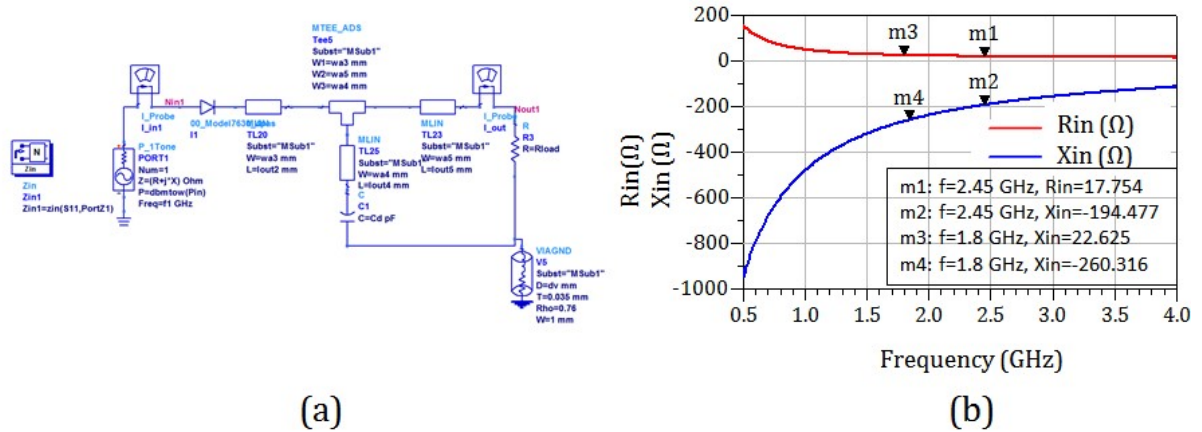


Fig. 4-4 (a) Schematic model of the rectifier using diode SMS 7630; (b) Input impedance of diode SMS 7630 at $P_{in}=0.32 \mu W$; $f=2.45$ GHz; Load is optimized at maximum power point

Fig. 4-5 shows the input voltage versus R_{in} and X_{in} . From this estimation, compared with the impedance of the diode, the input voltage of the diode is about 35 mV at conjugate impedance and 8 mV at 50- Ω matching.

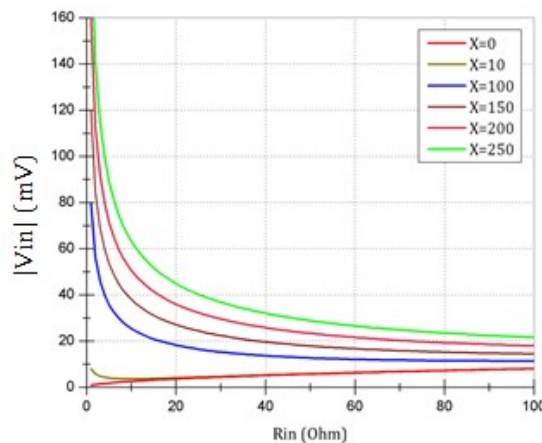


Fig. 4-5 Input voltage versus resistance R_{in} with $P_{delivered} = 0.32 \mu W$ ($f=2.45$ GHz)

In very low incident power, both calculated input voltages stay in the Off-State region of the diode and therefore deliver the same effect on the efficiency of the rectifier circuit. From there, it is possible to conclude that even the antenna and the rectifier have the conjugate matching or 50- Ω matching; the efficiency has the same order of magnitude.

The conjugate matching has the advantage of eliminating of the matching circuit but the design process of antenna and rectifier are closely linked. The 50- Ω matching, on the other hand, has to take into account the matching circuit, but design processes are independent and easily integrated into the external system outside of the working scope.

4.2 Operation of spatial diversity rectenna in realistic environment

Numerous studies on rectenna design have been carried out, aiming to achieve a high efficiency and to increase the output power from very low input power [51], [55], [57], [134]. In a realistic environment, there is seldom a stationary position with a clear line-of-sight (LOS) between sources and scavenging systems. Further indoor ambiance creates a multipath environment where signals may be reflected, diffracted or scattered. Therefore, the received power depends on environmental obstructions as well as the source power and distance. This creates a design challenge for energy scavenging antenna, requiring robust versatility to accommodate an unknown location and unknown polarization of incident waves as long as a faded location. To overcome these difficulties, mobile communication technology integrates simultaneous multi-antenna in a multiple-input-multiple-output (MIMO) approach into a single design. However, this approach of multi-antenna in RF energy scavenging has not been broadly studied. Authors in [51] presented a 3x3 planar array antenna connected directly with 3x3 rectifier array in order to increase the harvested power and avoid complex feeds. As this design is planar, it can only capture energy in one direction. In [134] a multi-direction RF energy harvester was developed but there are only two directions involved and no realistic measurement was conducted to verify the effectiveness of the principle. In current literature, some designs were validated by measurement in realistic indoor and outdoor environments but no details of the direction setup and analysis of the design's influence on random locations were presented, especially no multi-direction antenna harvester system operating in realistic scenarios was realized [55], [57], [135].

This section proposes measurements of a multi-direction spatial diversity antenna system in an office-like environment for energy harvesting from the Wi-Fi access point of WLAN sources, at the frequency of 2.45 GHz. The objective of this study is to confirm the performance of the diversity antenna, under precise conditions with supportive results. The methodology used to achieve the high isolation across multiple antennas system is presented. Measurements will focus on comparing probability density functions of harvested power in different scenarios and the experimental results will be analyzed.

4.2.1 Diversity antenna concept

In mobile communication domain, multipath environments have been extensively studied in order to determine algorithms allowing for improvement of the performance of the decoding process.

Within these studies, various propagation models were proposed for both indoor and outdoor environments including models for Path Loss, models for Small-scale Fading such as Ricean distribution, Rayleigh distribution, Suzuki model and Nakagami model [136]. These probabilistic models of received RF power have offered more representative models.

It can be noted that the WLAN sources are dynamic and use time-varying transmitted power and depend on the number of users on the network. Additionally, in typical office environments, there are often several Wi-Fi access points with the same characteristic of transmitter antenna, which operate at the same time, so interference might also occur at the receiver location.

The probability of accessing the highest power source in a non-fixed location improves with the number of transmitters. However, this increase is nonlinear due to the constructive and destructive combinations over space: varying amounts of received energy are expected at each receiver point [137]. Several studies are related to the propagation measurement in indoor multipath environments [138] and the obtained results for mean signal power levels were around 50 dB and 60 dB less than the signal power at the source. That means with a Wi-Fi source transmitting approximately 50 mW, the power level in the ambient is estimated at about -34 dBm. This rather low power availability considerably reduces potential voltage input of the rectifier circuit and decreases the overall efficiency. Therefore, the antenna gain and radiation characteristics play an important role in the system's ability to amplify the signal level.

The maximum directivity of antenna D_0 is calculated as [88]:

$$D_0 = \frac{4\pi}{\Omega_A} \quad (4.10)$$

where Ω_A represents the beam solid angle of the antenna.

Observing (4.10) there is always a trade-off between the directivity aspect and the beam solid angle of the antenna.

Due to the unpredictable characteristics of the incident wave, an omnidirectional antenna is preferable on the one hand to increase the probability of receiving the highest power. On the other hand, to achieve a very high gain, the antenna must be directional. Linear and planar antenna arrays are common solutions for this issue. The limitation here is that this usually has a higher gain and narrower beam solid angle, which is not the objective of this study.

Diversity antenna technique, however, is established as an effective solution to improve the performance of wireless service operating in a multipath fading environment. This study proposes a multi-antenna system using multi-direction spatial diversity in order to increase the probability of harvesting energy by using a basic linear polarization microstrip patch antenna where the direction of maximum gain is normal to the patch [88]. In order to take advantage of high gain and omnidirectional patterns at the same time, multiple directional antennas are used and are arranged in the environment space to maximize the chance of capturing ambient energy.

4.2.2 Rectenna design

a. *Antenna arrangement*

It is clear that the spatial output voltage distribution of the rectenna primarily depends on the radiation pattern of the antenna itself. In [139], authors have distributed a 3D voltage pattern measurement of rectenna and then compared it with the radiation pattern of the antenna. The results show that both distributions have similar tendencies and the main lobe is also situated in the same direction.

A typical array antenna widely used in literature was the planar arrangement that receives an incident wave from azimuth plane in one direction [51]. Besides this setup, the 3D arrangement has been studied also as a promising technique to increase the probability of receiving energy from multiple directions [140], [141].

We have conducted a study in order to compare the performance of these arrangements in function of gain and occupied area. Four identical patch antennas were placed in two forms: planar array antenna as presented in Fig. 4-6a and 3D array antenna as presented in Fig. 4-7a. The antenna element was designed to operate at frequency 2.45 GHz, which is the central frequency of WLAN service. The substrate used for this design is Rogers 4003 with a thickness of 0.830 mm, a relative permittivity of 3.55 and a loss tangent of 0.0027. Antenna dimensions are 32 mm×31.5 mm. Each antenna has a gain of about 5 dBi and a beam solid angle about 90°.

The simulation results of the radiation pattern of these two arrangements suggest that with the same element size, the 3D has smaller occupied space and has the highest gain (5.23 dBi instead of 4 dBi in the planar array). The radiation pattern of each antenna in the 3D arrangement has also not been affected by other antennas (Fig. 4-6b, Fig. 4-7b). This aspect can be explained below by the mutual coupling.

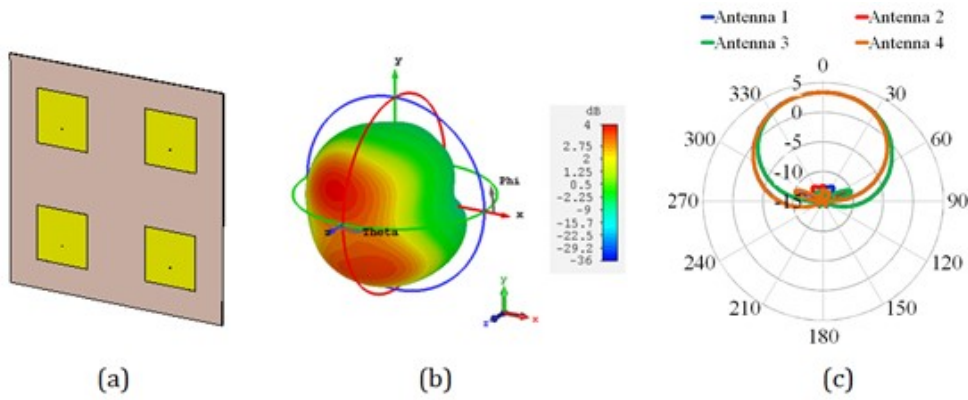


Fig. 4-6 (a) Planar array antenna; (b) Simulated radiation pattern of each antenna at 2.45 GHz; (c) E-plane of both four antennas at 2.45 GHz

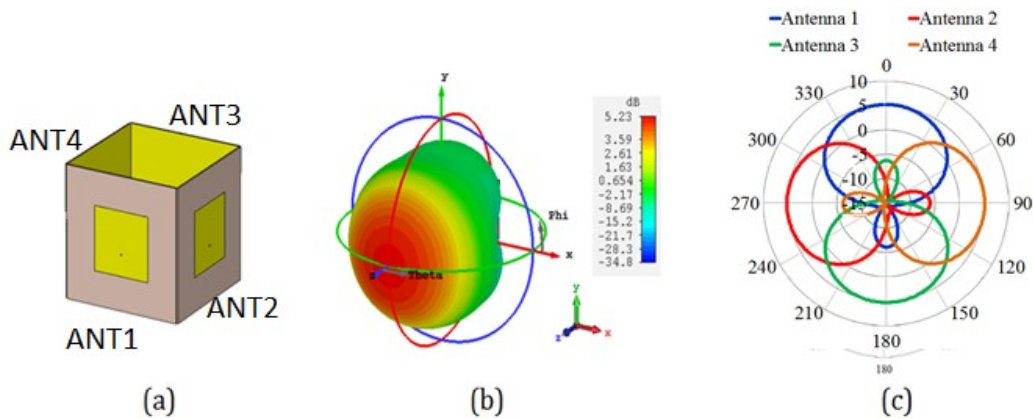


Fig. 4-7 (a) 3D array antenna; (b) Simulated radiation pattern of each antenna at 2.45 GHz ; (c) E-plane of both four antennas at 2.45 GHz.

For this reason, four microstrip patch antennas were used and were arranged in a way that their main lobes and beam solid angle can cover the maximum space; therefore, the spatial output voltage distribution increases (Fig. 4-8). The antennas were faced in opposite and perpendicular directions to take geometrical advantage of the packaging box.

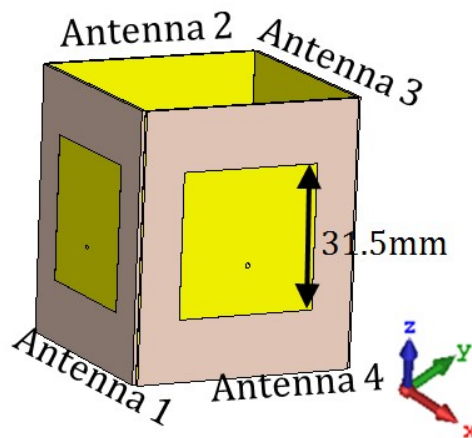


Fig. 4-8 Structure of proposed antenna diversity

The antennas have vertical polarization with E-plane vector along the z-axis. The system thus has the quasi-omnidirectional pattern and maximum directivity, which is the same for each element.

The essential challenge of packed multi-antennas is to decrease the mutual coupling effects between antennas, which can affect the input impedance and radiation pattern of each element. Since these four antennas are not positioned collinearly along the E-plane or the H-plane, their simulated isolation is already about -25 dB, what is acceptable for the application covered in this work. Increasing the dimensions of antenna substrate can increase the antenna gain but also decrease the mutual coupling. A parametric study has been carried out and the optimized dimensions of 50 mm×50 mm were chosen in order to keep the compact size of the system.

Fig. 4-9 Mutual coupling between antenna (dB)

Another technique can be adopted is polarization diversity. By placing each linear polarized element side-by-side orthogonally oriented towards each other, the mutual coupling becoming lower [142]. Fig. 4-9 shows the mutual couplings between antennas 1-2 and 3-4 are under -50 dB that is much lower than between antennas 1-3 and 2-4 which has the same polarization. This design is called as limited sequential rotation fashion [88]. In addition, if completed sequential rotation fashion among 4 elements is used, the mutual coupling effects due to higher order modes will be suppressed. This is an advantage in the nonlinear system of energy harvesting where a nonlinear element generates higher order harmonics in the circuit and this can fatally affect the overall efficiency.

b. Rectifier structure

It is explicit in literature several architectures to combine DC power of multiple-rectifiers, at the same frequency or different frequencies. However, these architectures have drawbacks on combining rectifiers at a different level of input power. The lower energy branches play the role of passive load to others branches: therefore decreasing the efficiency of the system. In [9], a series differential structure is proposed to combine different rectifiers without having DC interferences

between them. Nevertheless, this structure has to use a voltage doubler topology, which is not suitable for very low input power [6]. The output resistance of each rectifier branch depends on input RF signals, so the maximum power point of each branch is different. Therefore it is difficult to determine the optimum load for random power density from all the directions in ambient.

In this study, we use the traditional 50- Ω impedance interface between antenna and rectifier to simplify the design. The designs of two rectennas were proposed, corresponding to each configuration of measurement: a rectifier for a single antenna (rectifier A), a rectifier for four antennas (rectifier B) (Fig. 4-10). The rectifiers were designed using Agilent ADS software. The circuit uses the substrate Rogers RO 4003 and is optimized over the power input range of -50 dBm to -20 dBm. The rectifier device is a metal-to-metal Schottky diode SMS7630. Rectifier A was designed to have a maximum power point at -35 dBm and the load is 5.6 k Ω , which is close to the junction parasitic resistance of the diode. In order to design rectifier B, which combines the DC output of four rectifiers, the parallel structure was chosen [55]. A load of 1.8 k Ω was selected in order to maximize output power, in case the rectifier only had one main source and other branches were not excited. Consequently, the efficiency of the rectifier, in this case, is expected to be degraded compared to Rectifier A since each branch would not operate at their respective maximum power point, and the lower energy branches would play the role of passive load to the main branch.

Fig. 4-11 shows the simulation of output power versus the disparity of input power between branches of rectifier B, in comparison with rectifier A and rectifier B with only one input. Parameter *DeltaP* represents the difference between the highest input level and others at the input of Rectifier B. The results show that with the difference between the highest branch and others as being less than 5 dB, the structure would deliver better output power compared to a single input rectifier. The fabricated antennas and rectifiers are shown in Fig. 4-12.

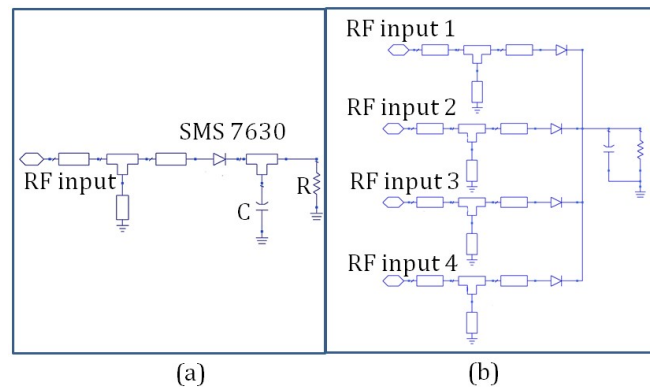


Fig. 4-10 Structure of proposed rectifiers: (a) Rectifier A- Single input rectifier schematic; (b) Rectifier B- Multi-input rectifier schematic

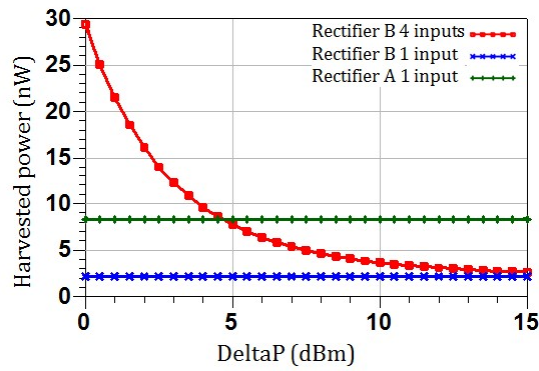


Fig. 4-11 Simulated output power versus different levels DeltaP between branches of rectifiers.

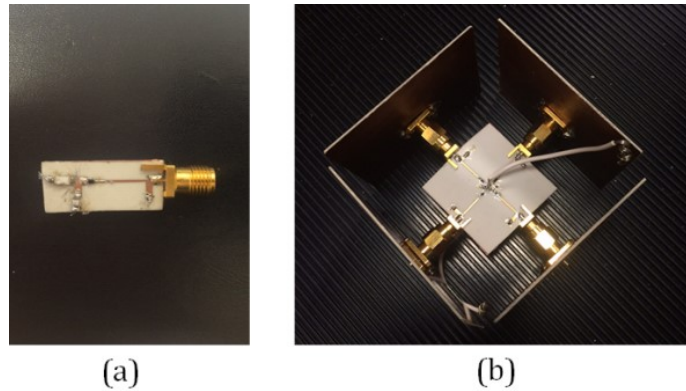


Fig. 4-12 Photo of fabricated Rectenna: (a) Rectifier A; (b) Rectifier B and 4 antennas

4.2.3 Experimental setup

The first measurement (M1) was conducted to obtain the characteristic of a designed multi-antenna system. The return loss, isolation, and radiation pattern measurements are realized by using a vector network analyzer (VNA) and an anechoic chamber.

The second measurement (M2) to evaluate the performance of the rectennas is performed in diverse scenarios listed in Table 4-2, listing different configurations of antenna combinations in a realistic environment. These configurations have performed in 98 points in a room of 4.2 m×2.1 m. As each point, 9 separated measurements have been conducted corresponding to 3 scenarios and have given 882 measurements in total. The first four measurements were conducted in order to estimate the available power in ambient at each point and each direction. These measurements allow for a performance evaluation of diversity antenna system operating in an indoor environment.

Table 4-2 Measurement scenarios

Scenario	Antenna	Rectifier	Device	Points	Number of measurements
M2.1	Each antenna	-	Power meter	98	4x98
M2.2	Each antenna	Rectifier A	Voltmeter	98	4x98
M2.3	Four antennas	Rectifier B	Voltmeter	98	98
TOTAL					882

Fig. 4-13 describes the measurement setup of the tests using two transmitter antennas in a realistic environment with office facilities around. Two identical commercial antennas for a Wi-Fi router with a gain of 5 dBi were used as transmission antennas. Transmission source A was set at 15 dBm, hence an equivalent isotropically radiated power (EIRP) of 100 mW, corresponding to the maximum transmission power of a conventional Wi-Fi router. The transmission source B was set at 12 dBm, which is equivalent to an EIRP of 50 mW. The elevation of two transmission antennas was fixed at 1.5 m and the elevation of the reception antennas was fixed at 0.8 m.

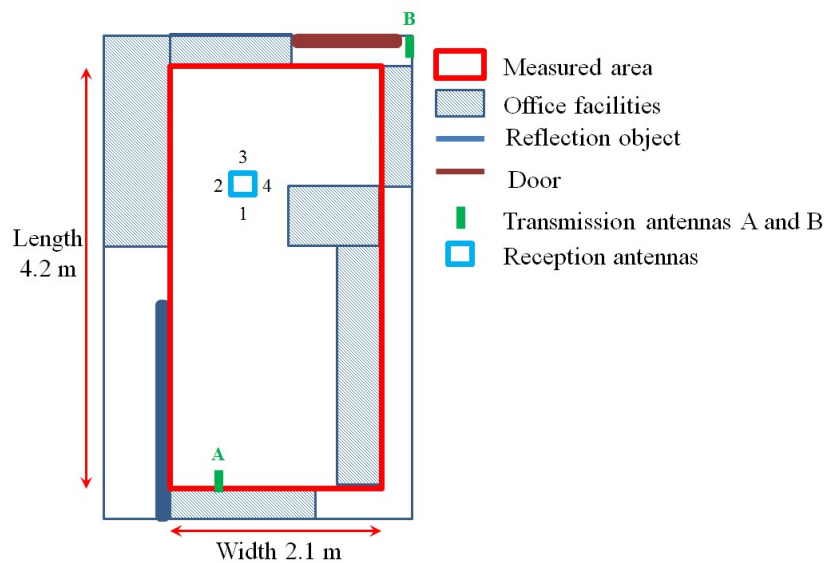


Fig. 4-13 Measurement setup

4.2.4 Measurement results

a. Antenna measurement

The four antennas have been characterized with the VNA Anritsu 37369A in the first measurement (M1). Fig. 4-14 presents the comparison of S-parameters between the simulation and experiment of fabricated antennas in vertical polarization, showing minimal coupling between antennas. The high isolations between antennas of -36 dB is observed, therefore this topology is used to conduct the scenarios of the second measurement. All four fabricated antennas have a resonant frequency around 2.45 GHz. The measured antenna gain is 4.9 dBi.

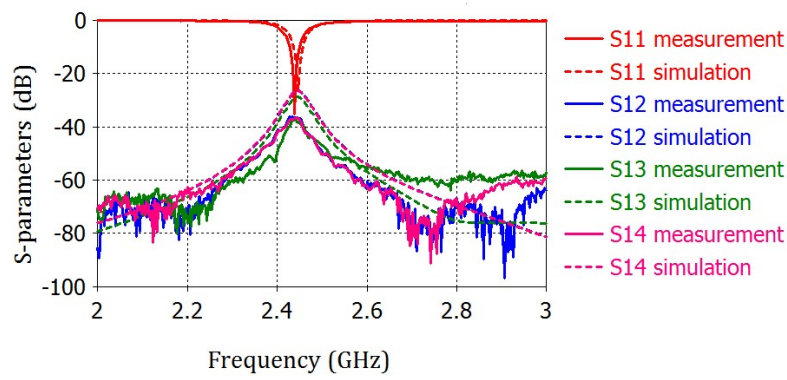


Fig. 4-14 Comparison of S-parameters between simulation and experimental results for both fabricated antennas.

b. Rectifier measurement

Fig. 4-15 presents the performance of both rectifiers, with input power from -45 dBm to -20 dBm. The RF-DC conversion efficiency of rectifier A is 3.21% at RF power of -34 dBm and 13.8% at RF power of -25 dBm. These results support the simulation observations.

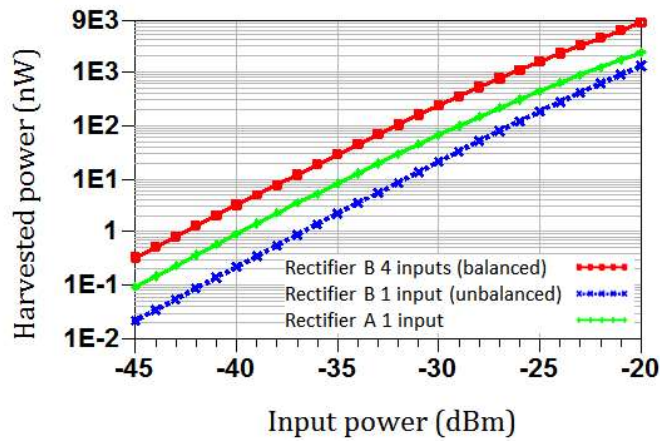


Fig. 4-15 Measured output power versus input power of rectifier A and B

c. Rectenna measurement in realistic environment

The first scenario of second measurement (M2.1) was conducted in order to estimate the available power in ambient at each point and direction. For 80% of the measurement points, power level differences (ΔP) at each direction were less than 10 dB. Kernel density estimation method was used to estimate the probability density function (PDF) and cumulative density function (CDF) of measured power values. The PDF and CDF of available power measurement results in the first scenario are presented in Fig. 4-16 and Fig. 4-17. Its median value is -34 dBm, which equivalent to a median density power of 10.5 nW/cm² or 1.05e⁻⁴ W/m².

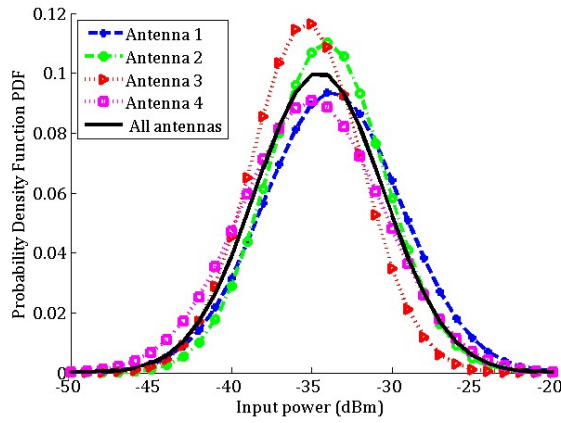


Fig. 4-16 Probability density function of input power (dBm) in different directions of antenna

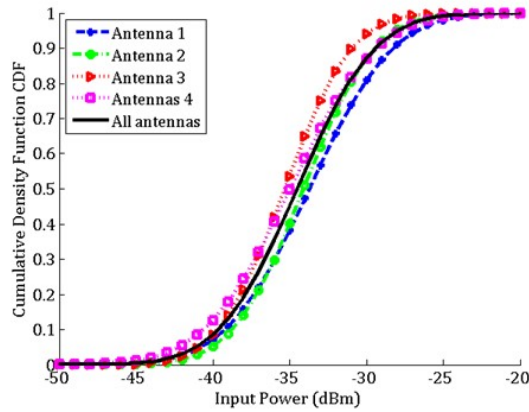


Fig. 4-17 Cumulative density function of input power (dBm) in different directions of antenna

The harvested power distributions of single rectennas in each direction of the antenna (as described in Fig. 4-13) conducted in the second scenario (M2.2) is presented in Fig. 4-18a, b, c, d respectively. The results denoted by different color gradient show a different pattern of output voltage distribution in each direction in the multipath environment. They also show the energy in space that is not harvested while using only one antenna with a limited beam solid angle. The received power is unevenly distributed in each direction. Fig. 4-18e shows the power distribution in space that can be harvested from multi-direction diversity antenna scenario (M2.3).

When there is only one input, rectifier B has a lower efficiency in comparison with rectifier A because of the losses in three other branches (Fig. 4-15). That explains the result in which with 30 points over 98 points of measurement, the harvested power of rectifier B with four antennas is lower than harvested power from rectifier A with a single antenna. Nonetheless, the level and density of harvested power from the proposed structure are much higher in overall.

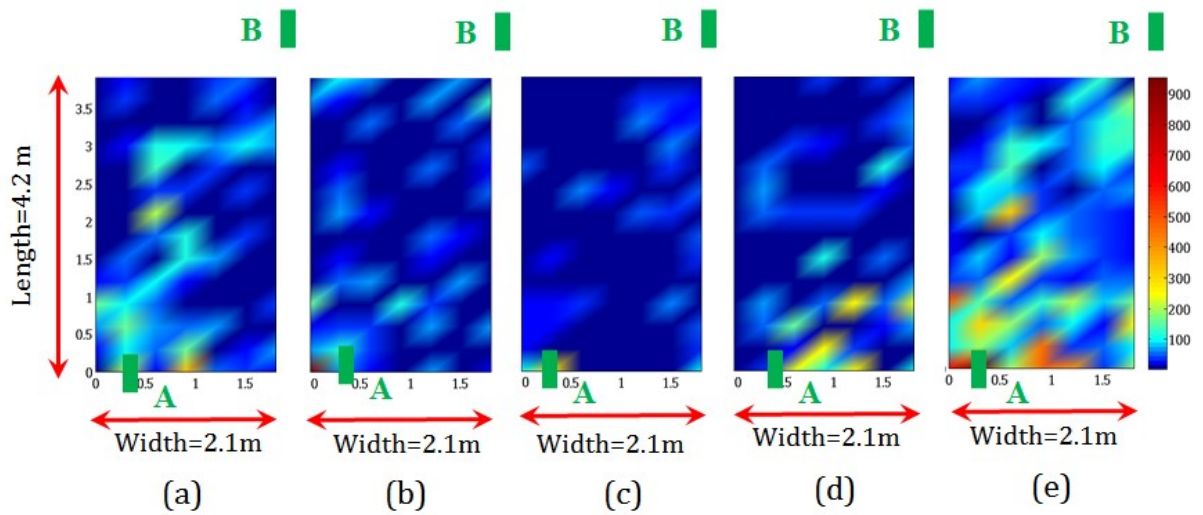


Fig. 4-18 Output voltage distribution of each antenna (mV): (a) Antenna 1; (b) Antenna 2; (c) Antenna 3 (d) Antenna 4; (e) Four Antennas

The PDF of harvested power in other scenarios is described in Fig. 4-19. It has the characteristic of Rayleigh distribution and shows different levels of possible harvested power in different directions of the antenna.

The CDF of harvested power over different scenarios is presented in Fig. 4-20. The CDF assessed at each value is the probability that the received power takes an amount less than or equal to that value.

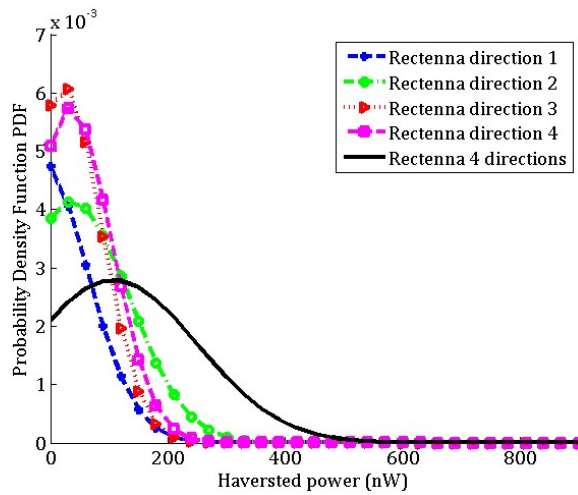


Fig. 4-19 Probability densities function of harvested power (nW) by various antennas.

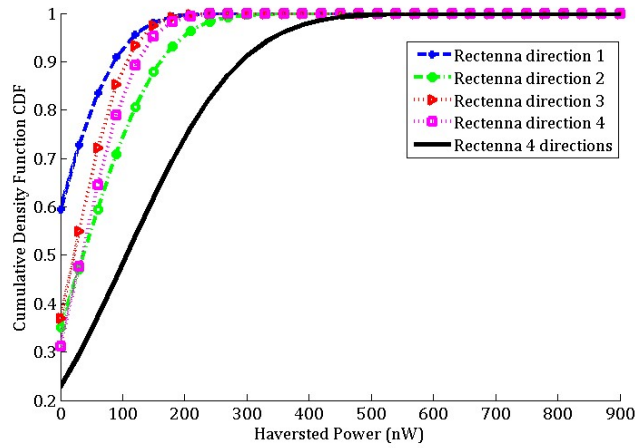


Fig. 4-20 Cumulative density function of harvested power (nW) in different scenarios of the multi-antenna system

Results strongly support that by using a diversity antenna system, the likelihood of received power greatly increases. The median harvested power of the proposed structure is 107 nW, which corresponds to a nominal RF-DC conversion efficiency η_{DC} of 6.7% at a median input power of -34 dBm. The probability that the harvested power becomes better than 100 nW is 16% when using rectifier A and 52% when using rectifier B with four antennas.

The median rectenna efficiency $\eta_{rectenna}$ is calculated as:

$$\eta_{Rectenna} = \frac{P_{DC}}{S_{RF} \times A_e} = \frac{P_{DC}}{S_{RF} \times 4 \times \frac{\lambda^2}{4\pi} \times G} \quad (4.11)$$

Where P_{DC} is the harvested power (W)

S_{RF} is the median power density (W/m^2), in this case, equals to $1.05e^{-4} W/m^2$

λ is the wavelength at 2.45 GHz, equals to 0.122 m

G is the antenna's gain, equals to 4.9 dBi

Table 4-3 shows the comparison of rectenna's performance between two configurations: one antenna associated with rectifier A (Rectenna 1A) and four antennas associated with rectifier B (Rectenna 1B).

Table 4-3 Comparison of harvested power (HP) between configurations

Rectenna	Probability of harvested power higher than 100 nW	Median HP (nW)	Median $\eta_{rectenna}$ at 0.1 mW/m ²
Rectenna 1A	16%	13	3.3%
Rectenna 1B	52%	107	6.7%

d. *Conclusion*

This section has presented a study about antenna diversity for ambient RF energy scavenging operating in a more realistic indoor environment. Results illustrate the benefits of diversity antenna systems, especially at a low input power environment. Observations strongly suggest that by using this technique, we prevent the fading of received signals across random points in space. Additionally, the probability of harvested power of more than 100 nW was drastically increased from 16% by using 1 antenna to 52% by using 4 antennas in different directions. The median efficiency of the rectenna also increases from 3.3% to 6.7% by using diversity conception.

4.3 Flexible diversity rectenna

After studying the operation and advantage of diversity antenna in RF energy harvesting context, a flexible diversity rectenna is presented in this section in order to meet all the design challenges of the RF energy harvesting as described in Fig. 4-1.

Concerning the antenna design on a flexible substrate, there were several approaches that were mentioned in the state-of-the-art, including textile-based, polymer-based and paper-based substrates. Depending on the application, each of these approaches can work under different circumstances.

Textile-based antennas are mainly planar antennas, specifically microstrip patch antennas [62][63] and dipole antennas [65]. This type of substrate offers a lowest dielectric constant due to the presence of air and can lead to the larger size of antennas. The paper-based substrate has the advantage of being recyclable, flexible and low cost. However, as mentioned in Chapter 2, their loss tangent can vary from high to very high values and can affect the radiation efficiency of the antenna.

The polymer-based substrate, in the opposite, can maintain a low loss tangent and offers a medium permittivity value. The principal drawback of this type of substrate is the small thickness, which leads to high conductor loss and radiation loss in the directional-type of the microstrip-based antenna. In this section, the proposed antenna is based on the PET substrate with permittivity $\epsilon_r=3.21$, thickness $h_{\text{sub}} = 0.175$ mm and loss tangent $\tan\delta =0.0049$. Screen printing technology is used to create a conducting ink layer, made of silver nanoparticles with a thickness of 0.01 mm. This design will propose a solution to limit those losses and provide a practical way to integrate the antennas and circuits in the diversity rectenna by taking advantage of the flexibility characteristic.

4.3.1 Flexible diversity antenna design

a. Antenna configuration

The design is based on the quasi-Yagi structure, which was presented in section 2.5, Chapter 2. The designed antenna offers a theoretical gain of 8.1 dBi, radiation efficiency of 83.5% and total efficiency of 77% at a frequency of 2.45 GHz. The basic quasi-Yagi antenna has the end-fire radiation characteristic. Thus four antennas are put together in order to have the same vertical polarization but the different direction of propagation.

It can be noted that even if the antenna is adapted to the resonant frequency, the conductor loss is still high that causes the lower total efficiency observed. In order to form the diversity antenna by combining four antennas and arranging them around the rectangular form of the system packaging, the transmission line leading to each antenna has to be oriented in the same plane.

One basic way to achieve this topology is to modify the feed line that has to be perpendicular to the end-fire radiation to avoid the conflict when connecting four antennas together (Fig. 4-21a). However, this structure has longer feed line, therefore increasing losses and decreasing the radiation efficiency of the antenna. Therefore, we propose the structure with direct line connection to the radiation arm as described in Fig. 4-21b. This design allows easier integration between antennas and common circuit. In this design, the driven element of the antenna operates like a monopole instead of a dipole as in original design. Thus, the second arm of the driven element is not necessary.

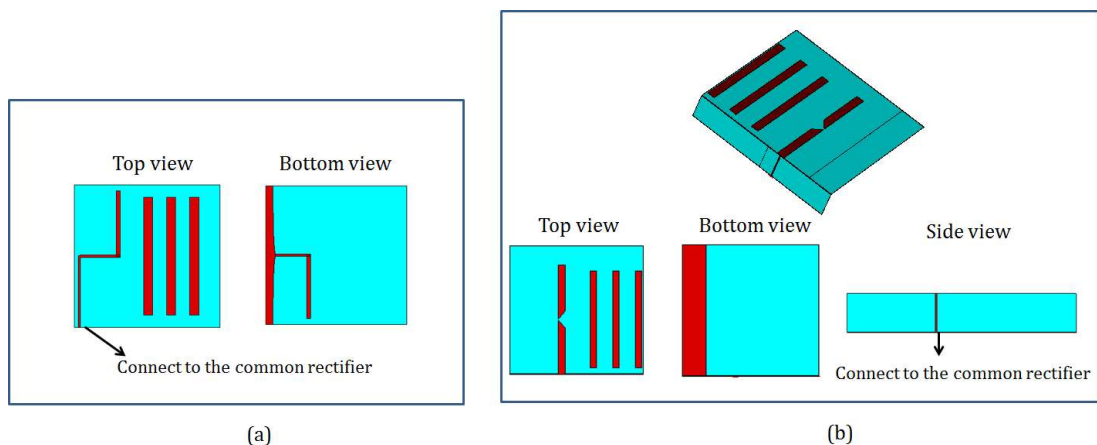


Fig. 4-21 Design of feed-line to connect to common circuit (a) original solution; (b) Proposed configuration

Besides, the design of one antenna has to take into account the influence of the rectifier's ground. The simulated reflection coefficient and radiation pattern of this antenna are presented in Fig. 4-22. The antenna has the radiation efficiency of 98.4% and total efficiency of 97.9%. This design has increased the radiation efficiency of the antenna of more than 20%.

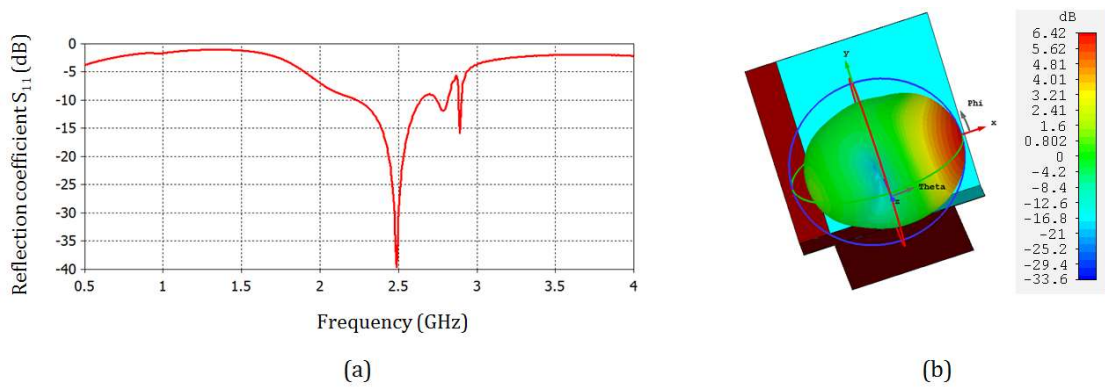


Fig. 4-22 (a) Simulated reflection coefficient; (b) Radiation pattern of proposed antenna

b. Technique to reduce mutual coupling and enhance the antenna gain

The arrangement of four antennas into one antenna diversity system has a great significance to the radiation pattern of the system. If four antennas are arranged in the cascade topology, the radiation pattern of each antenna will be degraded notably because of the placement of the ground in the direction of propagation. Therefore, four antennas have been arranged in two pairs with same ground and placed one pair opposite to the other.

Nevertheless, while placing four antennas together in system packaging (Fig. 4-23a), the mutual coupling appears, especially between the two pairs ANT1- ANT2, and ANT3- ANT4. The mutual coupling is only serious and noteworthy between two antennas that lie on propagation direction of each other. The S-parameters are presented in Fig. 4-23b showing the mutual coupling of about -6 dB between these antennas and therefore degrading the total efficiency. The total efficiency of four antennas is lower down to 71% compared to 97.9% of only one antenna.

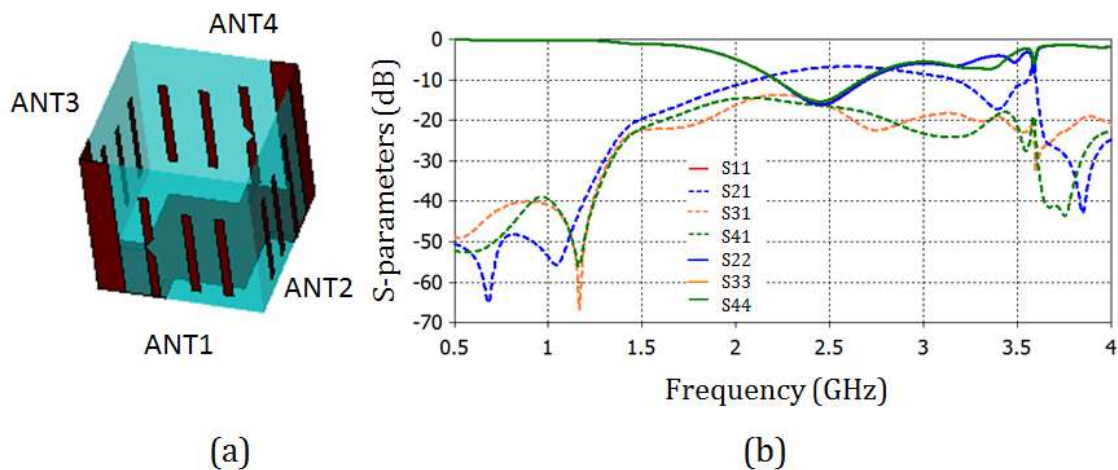


Fig. 4-23 (a) Configuration of four antennas in the system packaging; (b) S-parameters of four antennas

The techniques to reduce mutual coupling between antennas is necessary to ensure the operation of the diversity antenna. Several decoupling methods for multiple antenna system were

presented in literature, including defected ground structure (DGS), current localization, collocated orthogonal polarization, decoupling networks, neutralization line, parasitic elements, etc [143].

In this design, all the antennas have the same vertical polarization. Hence, the technique for reducing mutual coupling is proposed by slightly changes the polarization of each antenna. The direction of the driven element along the director element is adjusted in order to not match the others' polarization as described in Fig. 4-24a. The parameter da is a function of the angle α between the original position and inclined position. Fig. 4-24b shows the simulated mutual coupling between ANT1 and ANT2 in function of da . It can be seen that the longer da , the bigger $\sin(\alpha)$ and the more of isolation between ports.

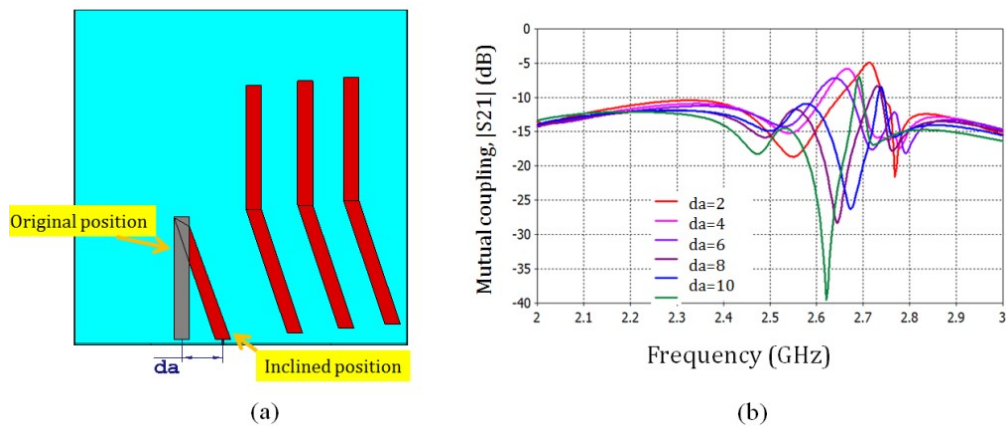


Fig. 4-24 (a) Detail of inclined position of driven and director element; (b) Mutual coupling in function of da

The driven element then has been optimized to have the tilt of about 15° compared to the original direction. By changing this parameter, the decoupling frequency can be controlled and therefore the performance of the diversity can be assured. The final design is presented in Fig. 4-25. The simulated mutual coupling between two antennas ANT1 and ANT2 is presented in Fig. 4-26. Applying the polarization changing technique, the mutual coupling between antennas is reduced from -6 dB to -33 dB.

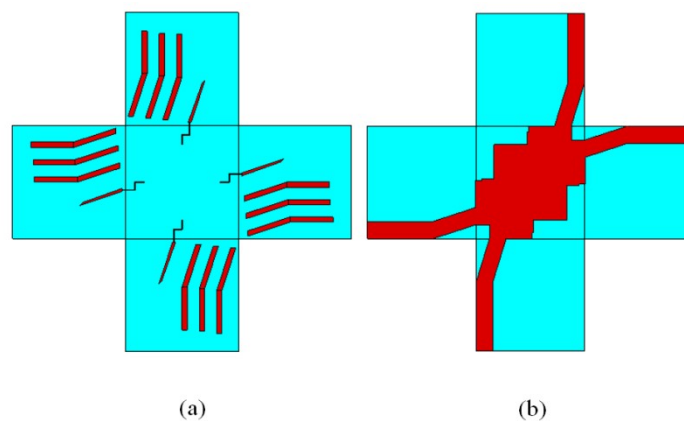


Fig. 4-25 Configuration of flat structure: (a) Top view; (b) Bottom view

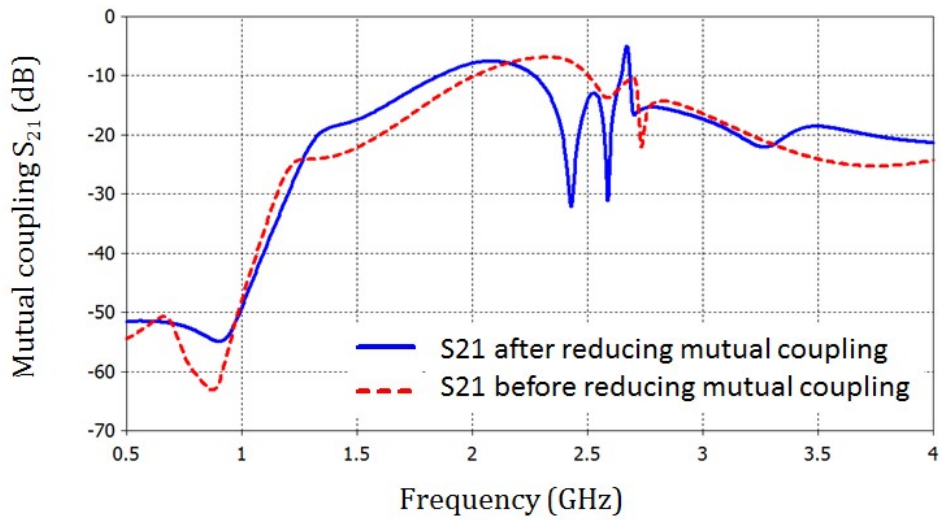


Fig. 4-26 Mutual coupling between two antennas ANT1 and ANT2 in system

The overall system in the system packaging is presented in Fig. 4-27. The simulated reflection coefficient and radiation pattern of the proposed diversity antenna are shown in Fig. 4-28. The optimized design has the size of 65 x 65 x 65 mm³. The calculated radiation efficiency is 91 % for the adjusted antenna compared to 71% without decoupling technique. The antenna system has the simulated gain of 6.2 dBi in each direction, in quasi-vertical polarization.

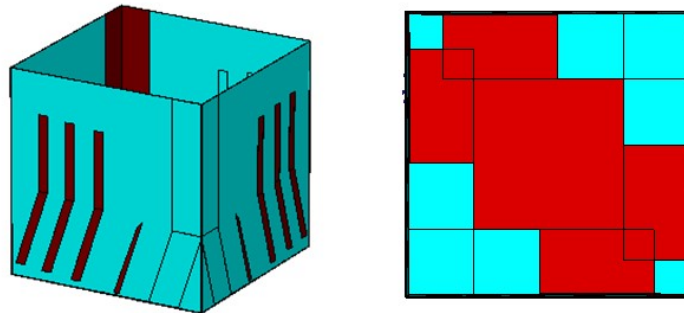


Fig. 4-27 Structure of proposed diversity antenna: (a) Perspective view; (b) Bottom view

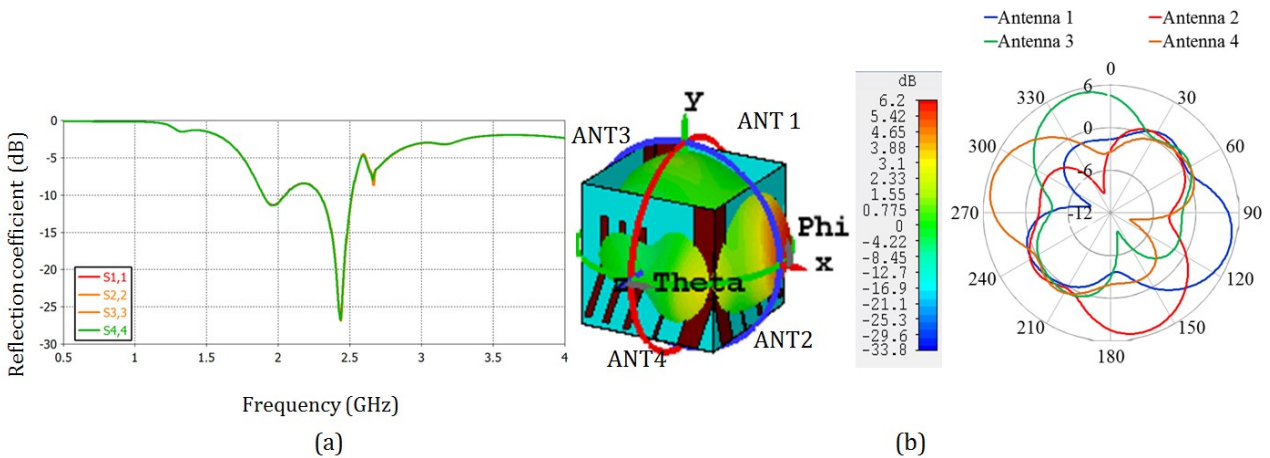


Fig. 4-28 (a) Simulated reflection coefficient; (b) Radiation pattern of the proposed diversity antenna

4.3.2 Interface between antenna and rectifier

The rectenna diversity is composed of four antennas and a circuit board whose inputs are the microstrip lines. The circuit is a four-port rectifier, which consists of four identical rectifiers and harvested power is combined at the DC level. All can be directly implemented on the same flexible substrate of the antennas and therefore it is not necessary to build the transition part between antennas and rectifiers. However, due to the very small thickness of the (PET) flexible substrate, the conductor loss will be significantly large and can reduce the efficiency of the rectifier. As a result, using a separate circuit with another substrate (like Rogers) could be one of the solutions.

a. *On flexible-substrate rectifier*

The same principle of four rectifiers in parallel as described in section 4.2.2 was used, on the same PET substrate of the antenna. The circuit is based on microstrip technology, which has three loss mechanisms: conductor loss, dielectric loss and radiation loss. Due to the small thickness of 0.175 mm, the conductor loss will dominate and therefore increase the insertion loss of the circuit. As a result, the same circuit developed in PET flexible substrate has significantly lower efficiency compared to Rogers substrate based circuit.

In addition, with lower permittivity, the guided wavelength in the circuit is longer and the circuit has a larger size as compared to the designed with circuit Rogers substrate. In order to fit into the reserved area of the designed antennas, the miniaturization of the circuit is necessary and the meander design technique was applied. The matching circuit consists of an open circuit, better than a short-circuit, which will complicate the fabrication process.

Fig. 4-29 describes the rectifier circuit in details and its implementation in the antenna diversity.

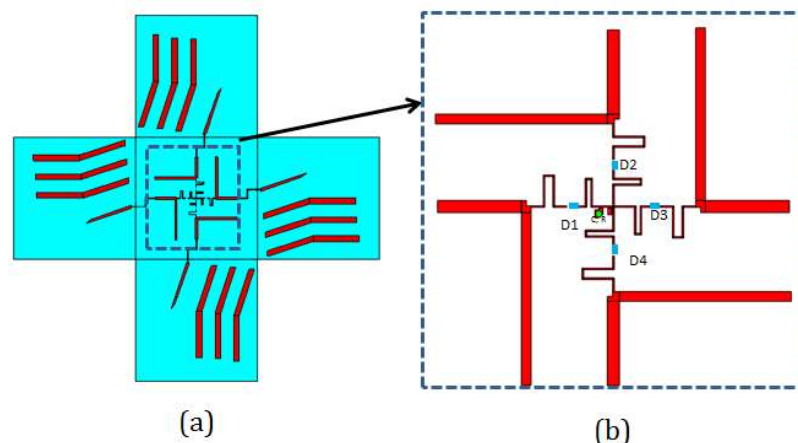


Fig. 4-29 (a) On-flexible-substrate rectifier with the antenna diversity; (b) Details of the rectifier circuit

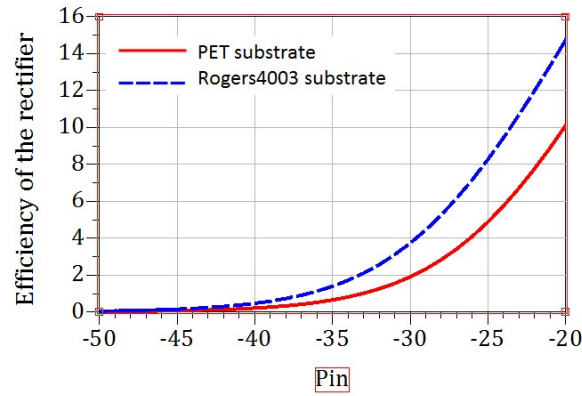


Fig. 4-30 Simulated efficiency of the rectifiers using PET and Rogers 4003 substrate depending on input power with ΔP between ports is 5 dB.

Fig. 4-30 shows the comparison between two rectifier circuits using two substrates with different thickness. The results show that with the very thin substrate, the efficiency of the rectifier is actually degraded and therefore the harvested power will be decreased. However, the advantage of this solution is in the easy fabrication process: the whole rectenna system can be printed in one time, at the same time limiting the insertion loss in transition parts between two substrates.

b. *Separate rectifier*

The rectifier circuit designed in section 4.2.2 was used to be connected the antenna diversity. Instead of using a board-to-board connector [144], which is expensive and not suitable to hold the flexible antenna, this study proposes to add a transition part between the antennas and the circuit.

Each antenna has a transition part, which is folded of 90 degrees from the antenna plane and consists of two segments of the line. One segment is the feed line of the antenna and the other is the common line with the circuit.

The circuit is placed in coincidence with four transition parts and is connected to them by eight screw connectors (Fig. 4-31). The common transmission lines are then affixed together by silver solder. The holes created for screw connectors have also the role of alignment guide between circuits.

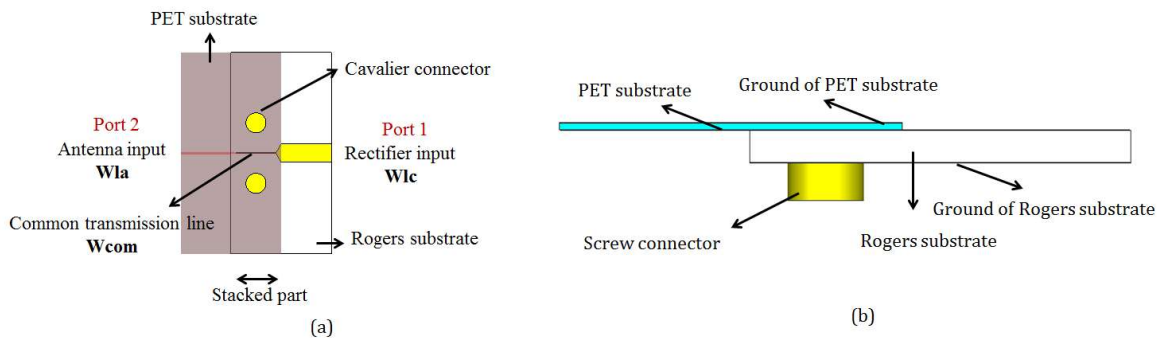


Fig. 4-31 Transition part between antenna and circuit: (a) Top view; (b) Side view

The impedance of transmission line of each segment is now decided by the permittivity effective formed by the combination of two substrates. In order to calculate the transmission line width, the permittivity effective of each segment was calculated. The width of the common line is then optimized in order to have the characteristic impedance of 50Ω , and is described in Table 4-4. Simulated S-parameters of the transition part are shown in Fig. 4-32. The insertion loss of the connection at 2.45 GHz is about 0.2 dB. This structure allows the low-loss connection between antennas and the rectifier circuits and therefore maximizes the harvested energy.

Table 4-4 Optimized width of the transmission line in the transition part

Substrate	Value	Parameter	Value (mm)
PET	$\epsilon_r = 3.21$; thickness=0.175 mm	W _{la}	0.4
Rogers 4003	$\epsilon_r = 3.55$; thickness=0.83 mm	W _{lc}	1.7
Transition		W _{com}	0.3

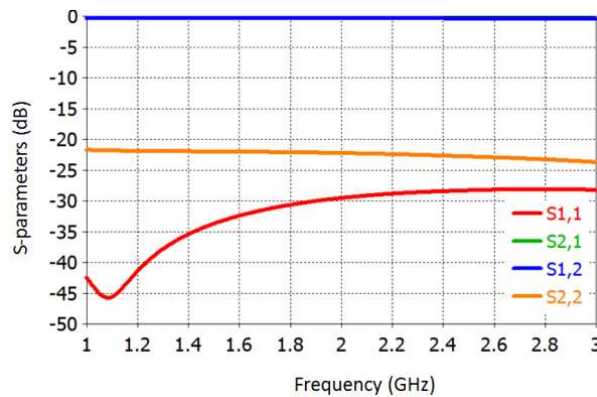


Fig. 4-32 Simulated S-parameters of the transition part

This structure has the advantage of keeping low substrate loss, thus rectifier's high efficiency at low power while connecting the rectifiers to the flexible antennas. In addition, this design of transition allows the antenna structure to keep flexibility when connecting with different circuits, not only the circuit used in this design.

4.3.3 Fabrication and measurement

a. *Fabrication*

The prototype of one antenna attached to the ground plane of the rectifier circuit and the flat structure of the proposed diversity design were fabricated by screen printing technology on the PET substrate. The used ink was silver conductive ink Electrodag PF-410 and the impression was performed using manual screen printer Svecia Semimatic SSM.

b. **Antenna measurement**

Fig. 4-33a shows the photo of the prototype of one antenna attached to the ground plane. The comparison of simulation and experimental reflection coefficients of this prototype is shown in Fig. 4-33b. The two resonance frequencies obtained in the simulation can be observed in measurement results. However, their levels of reflection are different. This difference can be explained by the way of using the end-launch connector in order to conduct the measurement as described in Fig. 4-34.

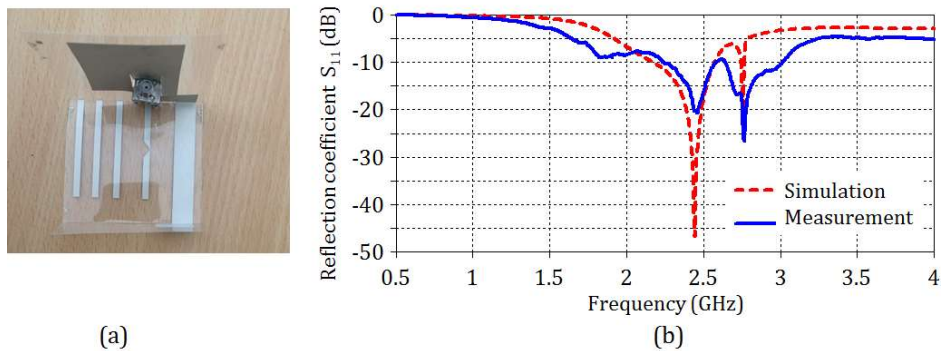


Fig. 4-33 (a) Prototype of one antenna attached to the ground plane: (b) Simulation and experimental of reflection coefficient

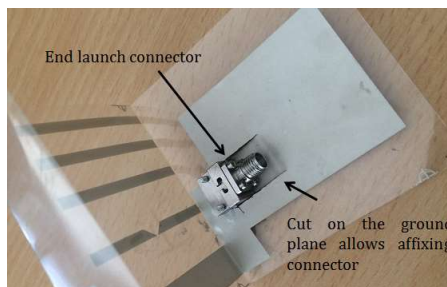


Fig. 4-34 Details of the end-launch connector in order to perform the measurement

The flat structure before folding of the proposed diversity rectenna (with rectifiers in the center) is shown in Fig. 4-35.

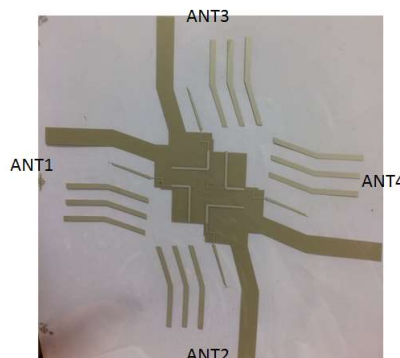


Fig. 4-35 Photo of fabricated rectenna before folding

The 3D rectenna in the form of system packaging was formed by folding the flat structure in four edges. There are two ways to fold the proposed circuit, where the rectifier circuit can be inside or outside the cube depending on the application needs. The end-launch connectors were also used in order to perform the S-parameters at each port of the diversity antenna. Fig. 4-36a describes the 3D form of the circuit and the connectors using for the antenna measurement.

Fig. 4-36b presents the comparison between simulation and experimental reflection coefficients at four ports. The results show the good matching for four antennas at the resonant frequency 2.45 GHz. The -10 dB impedance bandwidths of four antennas, which covers the band of WLAN 2.4 GHz, are provided in Table 4-5.

Table 4-5 Measured bandwidth of four antennas at 2.4 GHz

Bandwidth	Antenna 1	Antenna 2	Antenna 3	Antenna 4
Frequency (GHz)	2.35 – 2.48	2.24-2.48	2.28-2.49	2.33-2.51
MHz	130	240	210	180
%	5.4	10	8.7	7.5

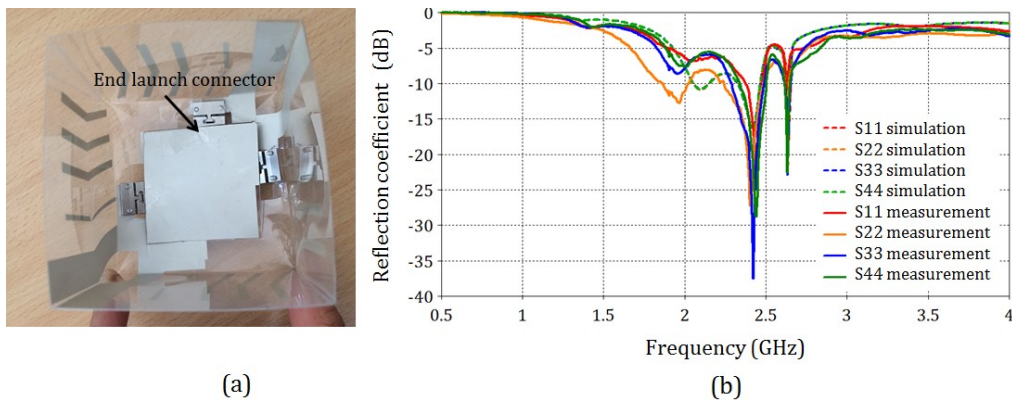


Fig. 4-36 (a) Details of the end launch connector in order to perform the measurement; (b) Simulation and measurement of reflection coefficient of four antennas in the diversity antenna system

The photo of the 3D diversity antenna with end-launch connectors while keeping the rectifier circuit together are shown in Fig. 4-37a. The presence of the ground plane ensures the operating conditions of the system as described in simulation section. The isolation between ports is presented in Fig. 4-37b. Table 4-6 shows the comparison of results for S-parameters between simulation and measurement for the diversity antenna at frequency 2.45 GHz. It can be seen that results agreement between simulation and measurement is correct for both impedance matching and the isolation between ports. The coupling between the most sensible pair ANT1 and ANT2, and ANT3 and ANT4 has been eliminated by the proposed technique.

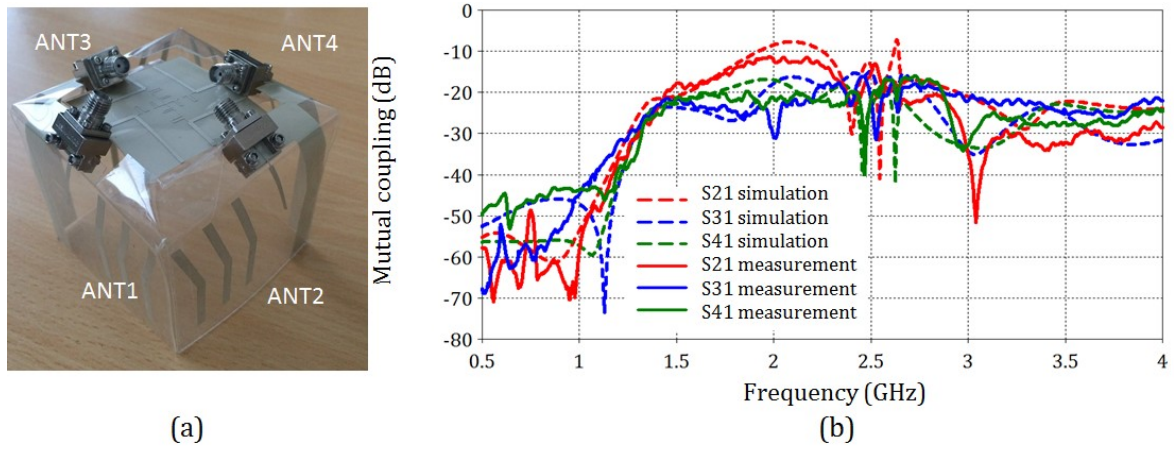


Fig. 4-37 (a) Photo of 3D diversity antenna with end-launch connectors; (b) Mutual coupling between antenna ANT1 and others antennas (in dB)

The measurement of radiation pattern was performed in an anechoic chamber and the E-plane measurement of each antenna at $\varphi=0$ is shown in Fig. 4-38. The maximum measured gain in each direction is 5.96 dBi, which is quite close to the simulated result.

Table 4-6 Comparison of S-parameters between simulation and measurement at 2.45 GHz

Reflection coefficient (dB)	Simulation	Measurement	Isolation (dB)	Simulation	Measurement
S11	-16.1	-24.1	S21	-21.5	-28.2
S22	-16.2	-19.4	S31	-15.3	-19.5
S33	-16	-31.3	S41	-23	-20.0
S44	-16.1	-17.9			

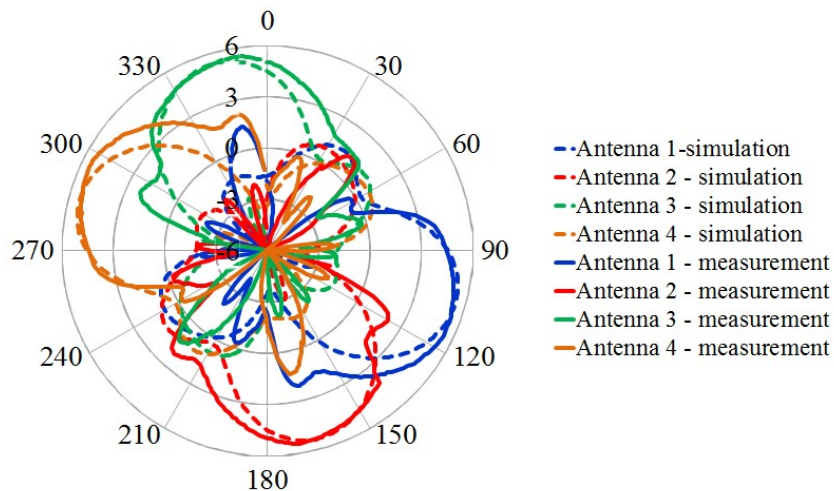


Fig. 4-38 Simulation and measurement of E-plane radiation pattern of four antennas

This diversity antenna features a quasi-omni radiation pattern and therefore can lead to quasi-omni voltage pattern at the output of the rectenna.

c. Diversity rectenna measurement in realistic environment

Two interfaces between antenna and rectifier were tested, one with on-flexible substrate rectifier and another with a separate rectifier (on Rogers 4003). The rectifier B in section 4.2.2 is used and the transition part is added to the circuit (Fig. 4-39a). The rectifier then connected with the diversity antenna to form the diversity rectenna as designed (Fig. 4-39b,c).

At the end, two prototypes of diversity rectenna in 3D-form, one with a separate rectifier (Rectenna 2) and one with on-flexible substrate rectifier (Rectenna 3) (Fig. 4-40) were measured in the realistic scenario of ambient indoor energy harvesting. The same setup measurement as mentioned in section 4.2.3 was used. However, only scenario M2.3 that involves the measurement of the completed circuit over 98 points in location was realized.

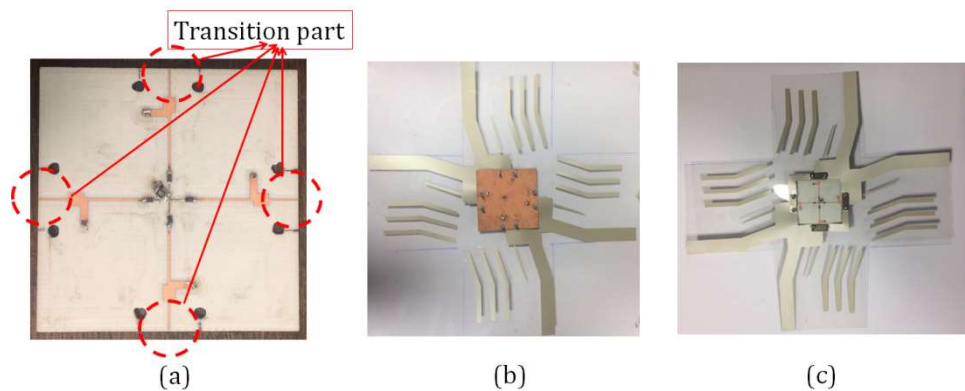


Fig. 4-39 (a) fabricated 4-port rectifiers with transition part; (b) connected diversity rectenna (bottom view); (c) connected diversity rectenna (top view)

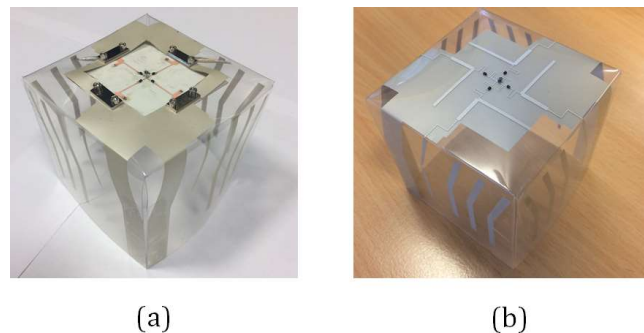


Fig. 4-40 Two completed diversity rectenna (a) With separated rectifier (Rectenna 2); (b) With on-flexible substrate rectifier (Rectenna 3)

The compared results of probability density function PDF and cumulative density function CDF between four rectennas are presented in Fig. 4-41 and Fig. 4-42.

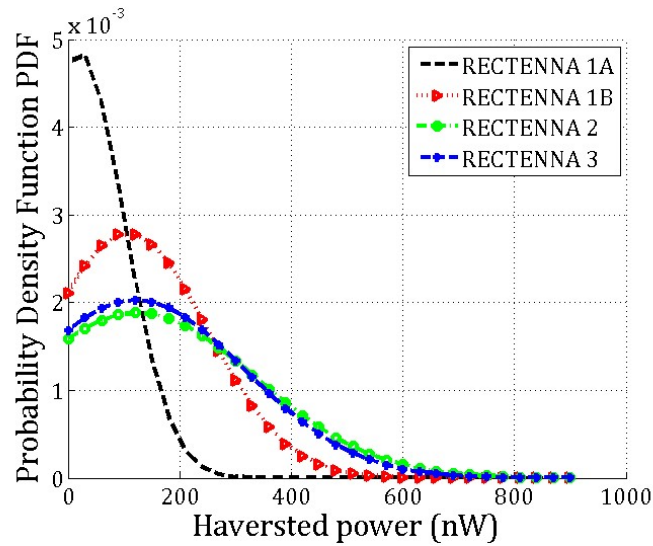


Fig. 4-41 Probability density function (PDF) of harvested power (nW) from four rectennas

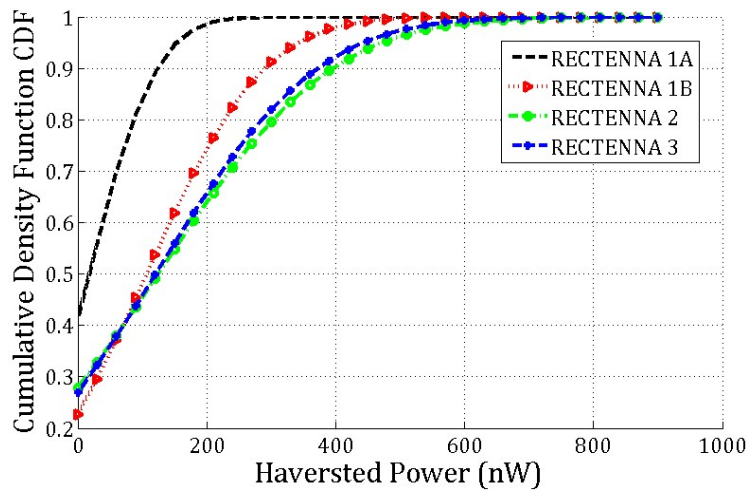


Fig. 4-42 Cumulative density function (CDF) of harvested power (nW) from four rectennas

The results support that by using the proposed flexible antenna, the probability of receiving higher power increases because the proposed antennas have higher gain compared to the patch antenna. However, the Rectenna 3 with integrated circuit has lower performance than the Rectenna 2 due to the loss of the flexible substrate. The median harvested power increases to 125 nW by using Rectenna 2 and 121 nW by using Rectenna 3. The probability of harvested power larger than 200 nW increases from 26% when using conventional patch diversity rectenna (Rectenna 1) to 37% when using a flexible antenna with a separate rectifier (Rectenna 2) and 35% when using proposed flexible rectenna (Rectenna 3). The rectenna efficiency is calculated using equation (4.11). The comparison of performance between configurations is provided in Table 4-7.

Though the Rectenna 3 has slightly lower performance compared to the separated one; the ease of fabrication, simplicity and the lightweight are still strong advantages of this diversity rectenna.

Table 4-7 Comparison of performance between configurations

Rectenna	Probability of harvested power (HP) higher than 200 nW @ 0.1 mW/m ²	Median HP (nW)	Median η_{rectenna} at 0.1 mW/m ²
Rectenna 1A	1.5%	13	3.3%
Rectenna 1B	26%	107	6.7%
Rectenna 2	37%	125	6.3%
Rectenna 3	35%	121	6.1%

4.4 Conclusion

This chapter has presented the global system of the RF energy harvesting for IoT application.

The matching impedance between antenna and rectifier has been analyzed. In case of very low incident power, the conjugate matching and the 50- Ω matching impedance impose the same effect on the input voltage of the Schottky diode. The diode will still operate in off-state and lead to very low-efficiency RF-to-DC conversion. As a result, the 50- Ω matching interface was chosen in order to ease the design and the characterization process.

However, the low efficiency of each rectifier requires combining sources in order to increase harvested power. The diversity rectenna is one of the solutions that can boost not only the harvested power but also the probability of receiving high power. Different topologies of diversity antenna were analyzed and were compared. The spatial diversity

technique has demonstrated its superiority in a more realistic indoor environment. Measurement results of patch antenna diversity strongly suggest that by using this technique, we prevent the fading of received signals across random points in space. Additionally, the probability of harvested power larger than 100 nW was drastically increased, from 16% by using 1 antenna to 52% by using 4 antennas in different directions in the ambient environment.

To meet the requirement of one high gain antenna diversity on the flexible substrate, the design process of flexible diversity rectenna was presented. In addition, to overcome the drawbacks of the substrate itself, a technique to decrease mutual coupling was also proposed. The mutual coupling between antennas decreases from -6 dB to about -30 dB with minor adjustment and the gain in each direction reaches about 6 dBi. The connection with rectifier circuits was investigated with two configurations: on the same PET substrate or on a separate Rogers substrate. The simulation and measurement results are in good agreement. The flexible rectenna in diversity conception increased the probability of harvested power higher than 200 nW from 1.5% in the conventional patch with one antenna to 35%. The results have shown the effectiveness of the proposed system in term of received power and practicableness of its form as a system packaging.

5. Conclusion and perspectives

5.1 Conclusion

This work focused on the antenna design on flexible substrates in regards to the integrated electronic and the efficiency in a realistic environment. The main contributions of this thesis are conformable antennas design to adapt to various situations of system packaging as long as various applications. In the approach of designing an antenna suitable for various dimensions of packaging, two types of the antenna were investigated: dipole-based antenna and coplanar-based antenna. Both designed antennas are multi-band antennas, operated at suitable frequencies for ambient energy harvesting. The dipole-based antenna was designed on the high-loss paper substrate and can be suitable for sticking on packaging with size varying from $76 \times 4 \times 25 \text{ mm}^3$ to $48 \times 18 \times 2 \text{ mm}^3$. This antenna has omnidirectional radiation pattern and operates at GSM frequency 1800 MHz, UMTS frequency 2100 MHz and Wi-Fi frequencies 2.45 GHz and 5.2 GHz. The gain varies from 1 dBi to 3 dBi and can be degraded from 0.1 dB to 1.2 dB up to the folding configuration.

In order to increase the antenna gain, a version of the coplanar-based antenna has been developed on PET substrate. This antenna also operates in multi-frequency bands: GSM 900 MHz, GSM 1800 MHz, and LTE 2.6 GHz. The realized gain varies from 1.37 dBi at lowest frequency to 6.15 dBi at the highest frequency. The bending and folding affection have been analyzed. The antenna can be folded from the flat position to a configuration of $77 \times 30 \times 28.5 \text{ mm}^3$ or can be bent toward a cylindrical form with radius down to 14 mm, without changing the resonant frequencies. The flat size of this antenna is $87 \times 77 \text{ mm}^2$, which corresponds to $0.37 \lambda_g \times 0.33 \lambda_g$. A study to compare this proposed antenna with other multi-band, flexible coplanar antenna in recent literature shows that our antenna has the best performance in term of the trade-off between antenna gain and size.

While engaging with a flexible substrate, the high-loss characteristic of the paper substrate is one of the major problems to take into account in order to enhance antenna performances. We discussed this problem and a solution based on suspended plate technique was used to design the antennas on high loss paper substrate, a loss tangent of 0.125 was observed for the paper. Two prototypes have been designed, fabricated and characterized. The miniature version of the suspended patch antenna has a gain increase of about 10 dB compared to conventional patch antenna at Wi-Fi frequency 2.45 GHz. The suspended multi-band antenna was designed and has similar performance with a realized gain of about 7 dBi.

Another primary challenge to ambient energy harvesting approach is a multitude of different power levels and frequencies used in wireless systems. Indoor ambient and outdoor ambiances already encounter different dominant frequencies in term of power density, not taken into account the fact that mobile phone frequencies are not the same all around the world. In resolving this problem, an adjustable frequency antenna has been proposed. The antenna is designed to be used in the presence of the circuit case or system packaging. It includes one removable part based on flexible substrate and can be easily removed to change with others. The configuration with four antennas operates on four frequency bands: GSM 1800 MHz, GSM 1900 MHz, UMTS 2100 MHz and WLAN 2.4 GHz. The maximum gain is 4.12 dBi and the total size of the antenna is 60 x 43 mm².

Concerning the interface between antenna and rectifier circuits, several Schottky diodes were characterized and realistic values of their parameters have been extracted in the frame of the new physical-based model. This diode model is the core of the RF-to-DC conversion and it helps to build more accurate rectenna circuits, especially the interface between antennas and integrated electronics. The detailed analysis of co-design has proved that with very low input power in the range of -40 dBm to -20 dBm, the interface impedance of 50- Ω has almost the same effect on RF-to-DC circuit efficiency of conjugate matching. Therefore, depending on the application, the appropriate impedance is chosen.

In order to combine sources at RF level, a low loss diplexer that operates at 1800 MHz and 2.45 GHz was designed. The diplexer has the size of 26 x 30 mm² and achieves a low insertion loss of 0.4 dB at working frequencies. This performance is proved better than other diplexer presented in the literature.

At the end, we have demonstrated a new approach for the design of combination rectenna in the very low power-density environment. The concept of diversity rectenna using basic patch antenna was tested and the experimental results prove that it has a superior effect on enhancing the probability of higher harvested power. The median harvested power while using a diversity of 4 antennas increased by 8 times compared to the use of a single antenna. The probability of harvested power larger than 100 nW in indoor ambient field drastically increases from 16% to 52%.

We have successfully designed this concept of diversity rectenna on PET flexible substrate, the thickness of 0.175 mm. The design using screen printing technology and allows printing at one time the whole diversity rectenna, which consists of 4 high gain antennas and 4-ports rectifier circuits. By using the folding technique, the final system has 3D-form and can easily immerse itself into system packaging. It occupies a volume of 65 x 65 x 65 mm³ and allows having a gain of about 6 dBi for four perpendicular directions in space in a quasi-omnidirectional radiation pattern. The performance of this diversity rectenna was tested in a realistic environment and the results were presented in comparison with the conventional configuration. At the end, the median harvested

power increases from 13 nW of the first design of rectenna with the conventional patch in one direction to 121 nW of the diversity on-flexible rectenna.

5.2 Perspectives

In this thesis, all the antenna designs concentrated on using system packaging to rely on and the study of bending and folding those antennas has been conducted. In the continuation of this work, many perspectives can be envisaged.

The support or system packaging material can be taken into account in the design. These materials/supports can alter the performances of the antenna but at the same time can decrease the size of the antenna because of the presence of material, which has permittivity higher than air in surrounding environment.

The support will be the subject of studies to select the most appropriate one not only from the point of view of a single layer but also in terms of structuration. It is indeed possible to find flexible materials made up of several layers, which opens possibilities that are more extensive to obtain the optimal operation of the antenna.

For the antenna design, the miniaturization of the proposed 3D antenna with the volume-efficient design is necessary for IoT applications.

For the rectifier design on a flexible substrate, that has thin substrate and high-loss, the alternative solution to increase the RF-to-DC efficiency needs to be considered. In addition, the integration of Power management systems for unbalanced rectifier on the flexible substrate can also be developed.

References

- [1] J. Li, H. Y. Zhou, D. C. Zuo, K. M. Hou, H. P. Xie, and P. Zhou, "Energy consumption evaluation for wireless sensor network nodes based on queuing petri net," *Int. J. Distrib. Sens. Networks*, vol. 2014, 2014.
- [2] W. C. Brown, "The History of Power Transmission by Radio Waves," *IEEE Trans. Microw. Theory Tech.*, vol. 32, no. 9, pp. 1230–1242, 1984.
- [3] A. Traille, A. Georgiadis, A. Collado, Y. Kawahara, H. Aubert, and M. M. Tentzeris, "Inkjet-printed 'Zero-Power' wireless sensor and power management nodes for IoT and 'Smart Skin' applications," *2014 31th URSI Gen. Assem. Sci. Symp. URSI GASS 2014*, 2014.
- [4] F. Yildiz, "Potential Ambient Energy-Harvesting Sources and Techniques," *J. Technol. Stud.*, pp. 40–48, 2007.
- [5] E. Yeatman, "Advances in power sources for wireless sensor nodes," ... *Implant. Body Sens. Networks*, pp. 6–7, 2004.
- [6] V. Marian, "Transmission d'énergie sans fil . Application au réveil à distance de récepteurs en veille zéro consommation," *Diss. Univ. Lyon*, 2012.
- [7] V. Kuhn, "Capture opportuniste d'énergie micro-onde pour l'autonomie des objets communicants," Telecom Bretagne, 2016.
- [8] B. R. Franciscatto, "Conception et réalisation d'un nouveau transpondeur DSRC à faible consommation," Université de Grenoble Alpes, 2014.
- [9] I. Kharrat, "Modélisation et réalisation d ' un système de récupération d'énergie imprimé Caractérisation hyperfréquence des matériaux papiers utilisés," Université Grenoble Alpes, 2014.
- [10] S. Adami, "Optimisation de la récupération d ' énergie dans les applications de rectenna," Ecole Centrale de Lyon, 2013.
- [11] T. Starner, "Human-powered wearable computing," *IBM Syst. J.*, vol. 35, no. 3.4, pp. 618–629, 1996.
- [12] N. S. Shenck and J. A. Paradiso, "Energy scavenging with shoe-mounted piezoelectrics," *IEEE Micro*, vol. 21, no. 3, pp. 30–42, 2001.
- [13] R. Morais *et al.*, "Sun, wind and water flow as energy supply for small stationary data acquisition platforms," *Comput. Electron. Agric.*, vol. 64, no. 2, pp. 120–132, 2008.
- [14] a Muetze and J. G. Vining, "Ocean Wave Energy Conversion - A Survey," *Ind. Appl. Conf. 2006. 41st IAS Annu. Meet. Conf. Rec. 2006 IEEE*, vol. 3, no. c, pp. 1410–1417, 2006.

- [15] S. Roundy, P. K. Wright, and K. S. J. Pister, "Micro-electrostatic vibration-to-electricity converters," *Proc. ASME Int. Mech. Eng. Congr. Expo.*, pp. 1–10, 2002.
- [16] S. Chalasani and J. M. Conrad, "A survey of energy harvesting sources for embedded systems," *Conf. Proc. - IEEE Southeastcon*, pp. 442–447, 2008.
- [17] A. Kurs, A. Karalis, R. Moffatt, J. D. Joannopoulos, P. Fisher, and M. Soljac, "Wireless Power Transfer via Strongly Coupled Magnetic Resonances," no. July, pp. 83–87, 2007.
- [18] Y. K. Tan, *Energy Harvesting Autonomous Sensor Systems: Design, Analysis and Practical Implementation*. 2012.
- [19] ICNIRP, "Icnirp Guidelines for Limiting Exposure To Time - Varying Guidelines for Limiting Exposure To Time-Varying," 2010.
- [20] IEEE Standards Coordinating Committee 28, *IEEE C95. 1-1992: IEEE Standard for Safety Levels with Respect to Human Exposure to Radio Frequency Electromagnetic Fields, 3 kHz to 300 GHz*, vol. 2005, no. April. 2006.
- [21] E. Union, "DIRECTIVE 2013/35/UE DU PARLEMENT EUROPÉEN ET DU CONSEIL du 26 juin 2013 concernant les prescriptions minimales de sécurité et de santé relatives à l'exposition des travailleurs aux risques dus aux agents physiques (champs électromagnétiques) (vingtième d," *Dir. 2013/35/UE*, vol. 2013, no. 3, pp. 1–21, 2013.
- [22] Agence National de Frequence, "Tableau national de repartition des bandes des frequences," 2013.
- [23] IM2NP *et al.*, "L3.1.1 : Etat de l'art des sources d'énergie," *ANR Program. ARPEGE*, pp. 1–38, 2010.
- [24] COPIC, "Diminution de l'exposition aux ondes électromagnétiques émises par les antennes relais de téléphonie mobile," 2013.
- [25] ANFR, "Etude de l' exposition du public aux ondes radioélectriques," pp. 1–18, 2015.
- [26] M. Pinuela, D. C. Yates, S. Lucyszyn, and P. D. Mitcheson, "Current State of Research at Imperial College London in RF Harvesting and Inductive Power Transfer," *2nd Int. Work. Wirel. Energy Transp. Harvest.*, p. 4, 2012.
- [27] D. BOUCHOUICHA, "Etude de faisabilité de la récupération d'énergie électromagnétique ambiante," Université François - Rabelais de Tours, 2010.
- [28] S. Mann, T. G. Cooper, S. G. Allen, R. P. Blackwell, and a J. Lowe, "Exposure to Radio Waves near Mobile Phone Base Stations," *Nrpb-R321*, no. June, 2000.
- [29] E. A. Kadir, A. P. Hu, M. Biglari-Abhari, and K. C. Aw, "Indoor WiFi energy harvester with multiple antenna for low-power wireless applications," *IEEE Int. Symp. Ind. Electron.*, pp. 526–

530, 2014.

- [30] U. Olgun, C. C. Chen, and J. L. Volakis, "Efficient ambient WiFi energy harvesting technology and its applications," *IEEE Antennas Propag. Soc. AP-S Int. Symp.*, pp. 2–3, 2012.
- [31] H. J. Visser, A. C. F. Reniers, and J. A. C. Theeuwes, "Ambient RF energy scavenging: GSM and WLAN power density measurements," *Proc. 38th Eur. Microw. Conf. EuMC 2008*, no. October, pp. 721–724, 2008.
- [32] C. R. Valenta and G. D. Durgin, "Harvesting wireless power: Survey of energy-harvester conversion efficiency in far-field, wireless power transfer systems," *IEEE Microw. Mag.*, vol. 15, no. 4, pp. 108–120, 2014.
- [33] T. W. Yoo and K. Chang, "Theoretical and Experimental Development of 10 and 35 GHz Rectennas," *IEEE Trans. Microw. Theory Tech.*, vol. 40, no. 6, pp. 1259–1266, 1992.
- [34] S. Hemour *et al.*, "Towards low-power high-efficiency RF and microwave energy harvesting," *IEEE Trans. Microw. Theory Tech.*, vol. 62, no. 4, pp. 965–976, 2014.
- [35] S. Hemour and K. Wu, "Radio-frequency rectifier for electromagnetic energy harvesting: Development path and future outlook," *Proc. IEEE*, vol. 102, no. 11, pp. 1667–1691, 2014.
- [36] I. Lyon and I. Rony, "Thèse présentée par : Focalisation des ondes électromagnétiques pour la transmission d'€™ énergie sans l Table des matières."
- [37] F. Yuan, *CMOS circuits for passive wireless microsystems*. 2011.
- [38] M. Roberg, E. Falkenstein, and Z. Popovic, "High-efficiency harmonically-terminated rectifier for wireless powering applications," *IEEE MTT-S Int. Microw. Symp. Dig.*, no. 1, pp. 0–2, 2012.
- [39] J. A. Hagerty, "Nonlinear Circuits and Antennas for Microwave Energy Conversion," 2003.
- [40] J. Guo, H. Zhang, S. Member, and X. Zhu, "Theoretical Analysis of RF-DC Conversion Efficiency for Class-F Rectifiers," vol. 62, no. 1, pp. 1–9, 2014.
- [41] A. Noda and H. Shinoda, "Compact class-F RF-DC converter with antisymmetric dual-diode configuration," *IEEE MTT-S Int. Microw. Symp. Dig.*, pp. 8–10, 2012.
- [42] H. Takhedmit and B. Merabet, "A 2.45-GHz Dual-Diode RF-to-dc Rectifier for Rectenna Applications," *Microw. ...*, no. September, pp. 37–40, 2010.
- [43] M. Stoopman, Y. Liu, H. J. Visser, K. Philips, and W. A. Serdijn, "Codesign of Electrically Short Antenna-Electronics Interfaces in the Receiving Mode," *IEEE Trans. Circuits Syst. II Express Briefs*, vol. 62, no. 7, pp. 711–715, 2015.
- [44] T. Lee, H. R. B. Kennedy, R. A. Bodnar, and W. Redman-White, "A CMOS MF Energy Harvesting and Data Demodulator Receiver for Wide Area Low Duty Cycle Applications with 230 mV Start-

- Up Voltage,” in *2016 IEEE Nordic Circuits and Systems Conference (NORCAS)*, 2016, pp. 1–4.
- [45] T. Lee, R. B. Kennedy, R. A. Bodnar, J. Scott, and W. Redman-White, “Wireless Power and Network Synchronisation for Agricultural and Industrial Remote Sensors using Low Voltage CMOS Harvesting and Data Demodulator IC,” in *the 22nd Electronics New Zealand Conference*, 2016, pp. 1–5.
- [46] D. Briand, E. Yeatman, and S. Roundy, *Micro Energy Harvesting*, vol. XXXIII, no. 2. Wiley VCH, 2012.
- [47] M. Stoopman, “Circuit Design for Highly Sensitive RF-Powered Wireless Sensor Nodes,” Delft University of Technology, 2016.
- [48] D. Briand, E. Yeatman, and S. Roundy, *Micro Energy Harvesting*, vol. XXXIII, no. 2. Wiley VCH, 2012.
- [49] U. Olgun, C. C. Chen, and J. L. Volakis, “Investigation of rectenna array configurations for enhanced RF power harvesting,” *IEEE Antennas Wirel. Propag. Lett.*, vol. 10, no. 2, pp. 262–265, 2011.
- [50] A. Mavaddat, S. H. M. Armaki, and A. R. Erfanian, “Millimeter-Wave Energy Harvesting Using 4x4 Microstrip Patch Antenna Array,” *IEEE Antennas Wirel. Propag. Lett.*, vol. 14, no. c, pp. 515–518, 2015.
- [51] U. Olgun, C.-C. Chen, and J. L. Volakis, “Design of an efficient ambient WiFi energy harvesting system,” *IET Microwaves, Antennas Propag.*, vol. 6, no. May, p. 1200, 2012.
- [52] STMicroelectronics, “STM32F205xx STM32F207xx,” 2016.
- [53] D. Ferreira, L. Sismeiro, A. Ferreira, R. F. S. Caldeirinha, T. R. Fernandes, and I. Cui??as, “Hybrid FSS and Rectenna Design for Wireless Power Harvesting,” *IEEE Trans. Antennas Propag.*, vol. 64, no. 5, pp. 2038–2042, 2016.
- [54] A. Georgiadis, G. Andia, and A. Collado, “Rectenna design and optimization using reciprocity theory and harmonic balance analysis for electromagnetic (EM) energy harvesting,” *IEEE Antennas Wirel. Propag. Lett.*, vol. 9, pp. 444–446, 2010.
- [55] M. Pinuela, P. D. Mitcheson, and S. Lucyszyn, “Ambient RF energy harvesting in urban and semi-urban environments,” *IEEE Trans. Microw. Theory Tech.*, vol. 61, no. 7, pp. 2715–2726, 2013.
- [56] V. Kuhn, C. Lahuec, F. Seguin, and C. Person, “A multi-band stacked RF energy harvester with RF-to-DC efficiency up to 84%,” *IEEE Trans. Microw. Theory Tech.*, vol. 63, no. 5, pp. 1768–1778, 2015.
- [57] C. Song *et al.*, “A Novel Six-Band Dual CP Rectenna Using Improved Impedance Matching Technique for Ambient RF Energy Harvesting,” *IEEE Trans. Antennas Propag.*, vol. 64, no. 7, pp.

3160–3171, Jul. 2016.

- [58] H. Sun, Y. X. Guo, M. He, and Z. Zhong, “A dual-band rectenna using broadband yagi antenna array for ambient rf power harvesting,” *IEEE Antennas Wirel. Propag. Lett.*, vol. 12, pp. 918–921, 2013.
- [59] Z. Liu, Z. Zhong, and Y. Guo, “Enhanced Dual-Band Ambient RF Energy Harvesting With Ultra-Wide Power Range,” *IEEE Microw. Wirel. Components Lett.*, vol. 25, no. 9, pp. 630–632, 2015.
- [60] R. Salvado, C. Loss, Gon, and P. Pinho, “Textile materials for the design of wearable antennas: A survey,” *Sensors (Switzerland)*, vol. 12, no. 11, pp. 15841–15857, 2012.
- [61] L. Zhang, Z. Wang, and J. L. Volakis, “Textile antennas and sensors for body-worn applications,” *IEEE Antennas Wirel. Propag. Lett.*, vol. 11, pp. 1690–1693, 2012.
- [62] M. Stoppa and A. Chiolerio, “Wearable electronics and smart textiles: A critical review,” *Sensors (Switzerland)*, vol. 14, no. 7, pp. 11957–11992, 2014.
- [63] I. Locher *et al.*, “Design and Characterization of Purely Textile Patch Antennas,” vol. 29, no. 4, pp. 777–788, 2006.
- [64] M. L. Scarpello, I. Kazani, C. Hertleer, H. Rogier, and D. Vande Ginste, “Stability and efficiency of screen-printed wearable and washable antennas,” *IEEE Antennas Wirel. Propag. Lett.*, vol. 11, pp. 838–841, 2012.
- [65] Z. Wang, L. Zhang, D. Psychoudakis, and J. L. Volakis, “Flexible textile antennas for body-worn communication,” *2012 IEEE Int. Work. Antenna Technol. iWAT 2012*, vol. 4, pp. 205–208, 2012.
- [66] M. L. Scarpello, L. Vallozzi, H. Rogier, and D. Vande Ginste, “High-gain textile antenna array system for off-body communication,” *Int. J. Antennas Propag.*, vol. 2012, 2012.
- [67] C. Ferández-Prades, H. Rogier, A. Collado, and M. M. Tentzeris, “Flexible substrate antennas,” *Int. J. Antennas Propag.*, vol. 2012, pp. 1–2, 2012.
- [68] T. Kaufmann, A. Verma, V. T. Truong, B. Weng, R. Shepherd, and C. Fumeaux, “Efficiency of a compact elliptical planar ultra-wideband antenna based on conductive polymers,” *Int. J. Antennas Propag.*, vol. 2012, 2012.
- [69] V. Radonić, K. Palmer, G. Stojanović, and V. Crnojević-Bengin, “Flexible Sierpinski carpet fractal antenna on a Hilbert slot patterned ground,” *Int. J. Antennas Propag.*, vol. 2012, 2012.
- [70] Y. Mahe, A. Chousseaud, M. Brunet, and B. Froppier, “New flexible medical compact antenna: Design and analysis,” *Int. J. Antennas Propag.*, vol. 2012, pp. 1–7, 2012.
- [71] H. L. Kao *et al.*, “Inkjet printed series-fed two-dipole antenna comprising a balun filter on liquid crystal polymer substrate,” *IEEE Trans. Components, Packag. Manuf. Technol.*, vol. 4, no. 7, pp. 1228–1236, 2014.

- [72] D. Unnikrishnan, D. Kaddour, S. Tedjini, E. Bihar, and M. Saadaoui, "CPW-Fed Inkjet Printed UWB Antenna on ABS-PC for Integration in Molded Interconnect Devices Technology," vol. 14, pp. 1125–1128, 2015.
- [73] J. G. Hester *et al.*, "Additively Manufactured Nanotechnology and Origami-Enabled Flexible Microwave Electronics," *Proc. IEEE*, vol. 103, no. 4, pp. 583–606, 2015.
- [74] C. Balanis, S. Saeed, and C. Birtcher, "Inkjet-Printed Flexible Reconfigurable Antenna for Conformal WLAN/WiMAX Wireless Devices," *IEEE Antennas Wirel. Propag. Lett.*, vol. 1225, no. c, pp. 1–1, 2016.
- [75] M. F. Farooqui and A. Shamim, "3D Inkjet Printed Helical Antenna with Integrated Lens," *IEEE Antennas Wirel. Propag. Lett.*, pp. 1–1, 2016.
- [76] A. Presse, J. M. Floc'H, A. C. Tarot, and C. Camus, "Broadband UHF flexible vivaldi antenna," *2013 Loughbrgh. Antennas Propag. Conf. LAPC 2013*, no. November, pp. 277–280, 2013.
- [77] M. C. Tang, T. Shi, and R. W. Ziolkowski, "Flexible Efficient Quasi-Yagi Printed Uniplanar Antenna," *IEEE Trans. Antennas Propag.*, vol. 63, no. 12, pp. 5343–5350, 2015.
- [78] M. C. Tang, B. Zhou, and R. W. Ziolkowski, "Flexible Uniplanar Electrically Small Directive Antenna Empowered by a Modified CPW-Feed," *IEEE Antennas Wirel. Propag. Lett.*, vol. 15, pp. 914–917, 2016.
- [79] B. S. Cook and A. Shamim, "Utilizing wideband AMC structures for high-gain inkjet-printed antennas on lossy paper substrate," *IEEE Antennas Wirel. Propag. Lett.*, vol. 12, pp. 76–79, 2013.
- [80] H. Saghlatoon, T. Bjorninen, L. Sydanheimo, M. M. Tentzeris, and L. Ukkonen, "Inkjet-printed wideband planar monopole antenna on cardboard for RF energy-harvesting applications," *IEEE Antennas Wirel. Propag. Lett.*, vol. 14, pp. 325–328, 2015.
- [81] D. De Donno, L. Catarinucci, and L. Tarricone, "An UHF RFID energy-harvesting system enhanced by a DC-DC charge pump in silicon-on-insulator technology," *IEEE Microw. Wirel. Components Lett.*, vol. 23, no. 6, pp. 315–317, 2013.
- [82] S. Lemey, F. Declercq, and H. Rogier, "Dual-band substrate integrated waveguide textile antenna with integrated solar harvester," *IEEE Antennas Wirel. Propag. Lett.*, vol. 13, pp. 269–272, 2014.
- [83] A. Georgiadis, A. Collado, S. Via, and C. Meneses, "Flexible hybrid solar/EM energy harvester for autonomous sensors," *IEEE MTT-S Int. Microw. Symp. Dig.*, pp. 6–9, 2011.
- [84] J. Maeng, B. Kim, D. Ha, and W. J. Chappell, "Parylene interposer as thin flexible 3-D packaging enabler for wireless applications," *IEEE Trans. Microw. Theory Tech.*, vol. 59, no. 12 PART 2, pp. 3410–3418, 2011.
- [85] H. Kanaya, S. Tsukamaoto, T. Hirabaru, D. Kanemoto, R. K. Pokharel, and K. Yoshida, "Energy

- harvesting circuit on a one-sided directional flexible antenna," *IEEE Microw. Wirel. Components Lett.*, vol. 23, no. 3, pp. 164–166, 2013.
- [86] A. Collado and A. Georgiadis, "Conformal hybrid solar and electromagnetic (EM) energy harvesting rectenna," *IEEE Trans. Circuits Syst. I Regul. Pap.*, vol. 60, no. 8, pp. 2225–2234, 2013.
- [87] K. L. Kim and V. Branimir, *Multiaccess, mobility and teletraffic for wireless communications*, vol. 3. Springer science Business media, LLC, 1999.
- [88] C. A. Balanis, *Antenna Theory: Analysis and Design*, Third Edit. A John Wiley & Sons, Inc., publication, 2012.
- [89] B. L. Pham and A. V. Pham, "Triple bands antenna and high efficiency rectifier design for RF energy harvesting at 900, 1900 and 2400 MHz," *IEEE MTT-S Int. Microw. Symp. Dig.*, pp. 13–15, 2013.
- [90] D. Masotti, a. Costanzo, and S. Adami, "Design and realization of a wearable multi-frequency RF energy harvesting system," *Proc. 5th Eur. Conf. Antennas Propag.*, pp. 517–520, 2011.
- [91] H. Kanj and S. M. Ali, "Compact multiband folded 3-D monopole antenna," *IEEE Antennas Wirel. Propag. Lett.*, vol. 8, pp. 185–188, 2009.
- [92] Y. Song, J. C. Modro, Z. Wu, and P. O'Riordan, "Miniature multiband and wideband 3-D slot loop antenna for mobile terminals," *IEEE Antennas Wirel. Propag. Lett.*, vol. 5, no. 1, pp. 148–151, 2006.
- [93] N. a. Zainuddin *et al.*, "Design of wideband antenna for RF energy harvesting system," *2013 3rd Int. Conf. Instrumentation, Commun. Inf. Technol. Biomed. Eng.*, pp. 162–166, 2013.
- [94] A. M. A. and M. a A. Ahmad Rashidy Razali1, "Compact Planar Multiband Antennas for Mobile Applications."
- [95] K. Li, C. H. Cheng, T. Matsui, and M. Izutsu, "Coplanar patch antennas: principle, simulation and experiment," *IEEE Antennas Propag. Soc. Int. Symp. 2001 Dig. Held conjunction with Usn. Natl. Radio Sci. Meet. (Cat. No.01CH37229)*, vol. 3, pp. 402–405, 2001.
- [96] M. W. A. Khan, E. Moradi, L. Syd??nheimo, T. Bj??rninen, Y. Rahmat-Samii, and L. Ukkonen, "Miniature coplanar implantable antenna on thin and flexible platform for fully wireless intracranial pressure monitoring system," *Int. J. Antennas Propag.*, vol. 2017, 2017.
- [97] H. Liu, P. Wen, S. Zhu, B. Ren, X. Guan, and H. Yu, "Quad-Band CPW-Fed Monopole Antenna Based on Flexible Pentangle-Loop Radiator," *IEEE Antennas Wirel. Propag. Lett.*, vol. 14, pp. 1373–1376, 2015.
- [98] S. Ahmed, F. A. Tahir, A. Shamim, and H. M. Cheema, "A Compact Kapton-Based Inkjet-Printed Multiband Antenna for Flexible Wireless Devices," *IEEE Antennas Wirel. Propag. Lett.*, vol. 14,

pp. 1802–1805, 2015.

- [99] Z. Hamouda *et al.*, “Dual-band elliptical planar conductive polymer antenna printed on a flexible substrate,” *IEEE Trans. Antennas Propag.*, vol. 63, no. 12, pp. 5864–5867, 2015.
- [100] H. Liu, S. Zhu, P. Wen, X. Xiao, W. Che, and X. Guan, “Flexible CPW-fed fishtail-shaped antenna for dual-band applications,” *IEEE Antennas Wirel. Propag. Lett.*, vol. 13, pp. 770–773, 2014.
- [101] H. R. Khaleel, H. M. Al-Rizzo, D. G. Rucker, and S. Mohan, “A compact polyimide-based UWB antenna for flexible electronics,” *IEEE Antennas Wirel. Propag. Lett.*, vol. 11, pp. 564–567, 2012.
- [102] M. O. Sallam, S. M. Kandil, V. Volski, G. A. E. Vandenbosch, and E. A. Soliman, “Wideband CPW-Fed Flexible Bow-Tie Slot Antenna for WLAN/WiMax Systems,” *IEEE Trans. Antennas Propag.*, vol. 65, no. 8, pp. 4274–4277, 2017.
- [103] S. Zhu and R. Langley, “Dual-band wearable textile antenna on an EBG substrate,” *IEEE Trans. Antennas Propag.*, vol. 57, no. 4 PART. 1, pp. 926–935, 2009.
- [104] T. Jung, J. Kwon, and S. Lim, “Flexible Zeroth-Order Resonant Antenna Independent of Substrate Deformation,” *Electron. Lett.*, vol. 46, no. 11, pp. 740–742, 2010.
- [105] B. S. Cook, S. Member, and A. Shamim, “Inkjet Printing of Novel Wideband and High Gain Antennas on Low-Cost Paper Substrate,” vol. 60, no. 9, pp. 4148–4156, 2012.
- [106] S. Kim *et al.*, “Monopole Antenna With Inkjet-Printed EBG Array on Paper Substrate for Wearable Applications,” vol. 11, pp. 663–666, 2012.
- [107] V. Nitu, G. Lojewski, and S. Nitu, “Electromagnetic field evaluation on an antenna shared site,” *Ieee Eurocon*, pp. 70–75, 2009.
- [108] S. Kitazawa, H. Ban, and K. Kobayashi, “Energy harvesting from ambient RF sources,” *2012 IEEE MTT-S Int. Microw. Work. Ser. Innov. Wirel. Power Transm. Technol. Syst. Appl. IMWS-IWPT 2012 - Proc.*, pp. 39–42, 2012.
- [109] L. Jianying *et al.*, “Bending effects on a flexible Yagi-Uda antenna for wireless body area network,” *2016 Asia-Pacific Int. Symp. Electromagn. Compat. APEMC 2016*, pp. 1001–1003, 2016.
- [110] S. M. Sze, *Semiconductor Devices: Physics and Technology*. 2006.
- [111] P. A. Blakelock, “Scale modelling and computer non-linear analysis of a Schottky Barrier Structure at 35 GHz,” Loughborough University of Technology, 1989.
- [112] L. U. Rohde and P. D. Newkirk, *RF/Microwave circuit design for wireless applications*, Second edi. John Wiley & Sons, inc., 2012.
- [113] K. Kaviarasu and V. Ganesh, “Design and simulation of a 900 MHz rectifier for Rectenna application,” *2015 Int. Conf. Commun. Signal Process. ICCSP 2015*, pp. 754–756, 2015.

- [114] C. Song, Y. Huang, S. Member, J. Zhou, J. Zhang, and S. Yuan, "A High-Efficiency Broadband Rectenna for Ambient Wireless Energy Harvesting A High-efficiency Broadband Rectenna for Ambient Wireless Energy Harvesting," vol. 63, no. MAY, pp. 3486–3495, 2015.
- [115] R. J. Weber and IEEE Microwave Theory and Techniques Society., *Introduction to microwave circuits : radio frequency and design applications*. 2001.
- [116] C. Papadopoulos, *Solid-State Electronic Devices*. Springer science Business media, LLC, 2014.
- [117] K. S. Dieter, *Semiconductor Material and device characterization*, Third Edit. Wiley Interscience, 2006.
- [118] H. Wang, X. Chen, G.-H. Xu, and K.-M. Huang, "A novel physical parameter extraction approach for Schottky diodes," *Chinese Phys. B*, vol. 24, no. 7, p. 77305, 2015.
- [119] F. Sischka, "Diode modeling tutorial," 2016.
- [120] L. Stauffer, "Fundamentals of Semiconductor C-V Measurements," Cleveland, 2009.
- [121] T. Kiuru, K. Dahlberg, J. Mallat, A. V Räsänen, and T. Närhi, "Comparison of low-frequency and microwave frequency capacitance determination techniques for mm-wave Schottky diodes," *14th Eur. Microw. Week 2011 "Wave to Futur. EuMW 2011 - 6th Eur. Microw. Integr. Circuit Conf. EuMIC 2011*, no. EuMIC, pp. 53–56, 2011.
- [122] H. Y. Zeng, G. M. Wang, D. Z. Wei, and Y. W. Wang, "Planar diplexer using composite right-/ left-handed transmission line under balanced condition," *Iet Journals Mag.*, vol. 48, no. 2, pp. 104–106, 2012.
- [123] T. Yang, P. L. Chi, and T. Itoh, "High isolation and compact diplexer using the hybrid resonators," *IEEE Microw. Wirel. Components Lett.*, vol. 20, no. 10, pp. 551–553, 2010.
- [124] F. Fu, X. J. Zhou, H. W. Deng, Y. J. Zhao, and Y. Y. Liu, "Compact and high isolation microstrip diplexer for GPS and UWB application," *Electron. Lett.*, vol. 49, no. 10, pp. 659–661, 2013.
- [125] P.-H. Deng and J.-T. Tsai, "Design of Microstrip Lowpass-Bandpass Diplexer," *IEEE Microw. Wirel. Components Lett.*, vol. 23, no. 7, pp. 332–334, 2013.
- [126] X. Guo, B. Cao, X. Lu, X. Zhang, and B. Wei, "Wideband superconducting diplexer with stepped-impedance cross-structure," *Electron. Lett.*, vol. 50, no. 18, pp. 1324–1326, 2014.
- [127] T. Yang, P. L. Chi, and T. Itoh, "Compact quarter-wave resonator and its applications to miniaturized diplexer and triplexer," *IEEE Trans. Microw. Theory Tech.*, vol. 59, no. 2, pp. 260–269, 2011.
- [128] S. Srisathit, S. Patisang, R. Phromloungsri, S. Bunnjaweht, S. Kosulvit, and M. Chongcheawchamnan, "High isolation and compact size microstrip hairpin diplexer," *IEEE Microw. Wirel. Components Lett.*, vol. 15, no. 2, pp. 101–103, 2005.

- [129] L. Zhu and K. Wu, "Accurate circuit model of interdigital capacitor and its application to design of new quasi-lumped miniaturized filters with suppression of harmonic resonance," *IEEE Trans. Microw. Theory Tech.*, vol. 48, no. 3, pp. 347–356, 2000.
- [130] KOA SPEER Electronics Inc., "Ceramic Chip Capacitors - Type NPO , X5R , X7R , Y5V."
- [131] F. Lafon, "Développement de techniques et de méthodologies pour la prise en compte des contraintes CEM dans la conception d'équipements du domaine automobile . Etude de l'immunité , du composant à l'équipement .," INSA de Rennes, 2011.
- [132] M. E. Goldfarb and R. A. Pucel, "Modeling Via Hole Grounds in Microstrip," *IEEE Microwave and Guided Wave Letters*, vol. 1, no. 6. pp. 135–137, 1991.
- [133] N. Shinohara and H. Matsumoto, "Dependence of dc output of a rectenna array on the method of interconnection of its array elements," *Electr. Eng. Japan*, vol. 125, no. 1, pp. 9–17, 1998.
- [134] J. Kimionis, M. Isakov, B. S. Koh, A. Georgiadis, and M. M. Tentzeris, "3D-Printed Origami Packaging With Inkjet-Printed Antennas for RF Harvesting Sensors," *IEEE Trans. Microw. Theory Tech.*, vol. 63, no. 12, pp. 4521–4532, Dec. 2015.
- [135] T. Q. Van Hoang, L. H. Trinh, F. Ferrero, E. Seguenot, T.-P. Vuong, and J.-L. Dubard, "Rectenna measurement in a realistic environment," in *2014 IEEE Conference on Antenna Measurements & Applications (CAMA)*, 2014, pp. 1–4.
- [136] T. K. Sarkar, Z. Ji, K. Kim, A. Medouri, and M. Salazar-Palma, "A Survey of Various Propagation Models for Mobile Communication," *IEEE Antennas Propag. Mag.*, vol. 45, no. 3, pp. 51–82, 2003.
- [137] M. Y. Naderi, K. R. Chowdhury, and S. Basagni, "Wireless sensor networks with RF energy harvesting: Energy models and analysis," in *2015 IEEE Wireless Communications and Networking Conference (WCNC)*, 2015, pp. 1494–1499.
- [138] A. U. Sheikh, M. Abdi, and M. Handforth, "Indoor mobile radio channel at 946 MHz: Measurements and modeling," in *IEEE 43rd Vehicular Technology Conference*, pp. 73–76.
- [139] T. Q. Van Hoang, E. Seguenot, F. Ferrero, J.-L. Dubard, P. Brachat, and J.-L. Desvilles, "3D Voltage Pattern Measurement of a 2.45 GHz Rectenna," *IEEE Trans. Antennas Propag.*, vol. 61, no. 6, pp. 3354–3356, Jun. 2013.
- [140] J. Kimionis, M. Isakov, B. S. Koh, A. Georgiadis, and M. M. Tentzeris, "3D-Printed Origami Packaging with Inkjet-Printed Antennas for RF Harvesting Sensors," *IEEE Trans. Microw. Theory Tech.*, vol. 63, no. 12, pp. 4521–4532, 2015.
- [141] F. Fezai, C. Menudier, and M. Thevenot, "Multidirectional Receiving System for RF to dc Conversion Signal," no. june, 2016.
- [142] H. J. Visser, *Array and Phased Array Antenna Basics*. 2005.

- [143] H. U. I. Li, *Decoupling and Evaluation of Multiple Antenna Systems in Compact MIMO Terminals*. 2012.
- [144] S. Microwave, "Pushing Board-to-Board Interconnect Performance Boundaries," no. May, 2016.

List of publications

Journal

- [1] **D. H. N. Bui**, T. P. Vuong, B. Allard, J. Verdier and P. Benech, "Compact low-loss microstrip diplexer for RF energy harvesting," in *Electronics Letters*, vol. 53, no. 8, pp. 552-554, 4 13 2017.
- [2] **D. H. N. Bui**, T. P. Vuong, B. Allard, J. Verdier and P. Benech, "Multi-direction rectenna diversity in packaging for ambient RF energy scavenging in realistic indoor scenarios", *IEEE Transactions on Components, Packaging and Manufacturing*, **submitted**.

International conferences

- [1] **D. H. N. Bui**, T. P. Vuong, J. Verdier, B. Allard, P. Benech, "3-D multi-frequency antenna for RF energy harvesting application", *2015 International Conference on Advanced Technologies for Communications (ATC)*, pp. 59-62, Hochiminh, Vietnam, Oct 2015
- [2] L. Benmessaoud, R. Touhami, **D. H. N. Bui**, T.P. Vuong, M.C.E. Yagoub, "3D High Gain UHF RFID Tag for Navigation Applications", *2015 IEEE 15th Mediterranean Microwave Symposium (MMS)*, pp. 1-4, Lecce, Italy, Nov 2015.
- [3] **D. H. N Bui**, T.P. Vuong, J. Verdier, B. Allard, P. Benech, "Adjustable Frequency Antenna Using Flexible Material for RF Energy Harvesting Application", *2016 IEEE International Symposium on Antennas and Propagation/USNC-URSI National Radio Science meeting*, Puerto Rico, 26 June- 1 July 2016.
- [4] **D. H. N Bui**, T.P. Vuong, J. Verdier, B. Allard, P. Benech, "Influences des connexions sur la caracterisation de petites antennes", *18^{ème} Colloque International et Exposition sur la Compatibilité ÉlectroMagnétique (CEM 2016)*, Rennes, 11-13 Juillet 2016.
- [5] **D. H. N Bui**, T.P. Vuong, J. Verdier, B. Allard, P. Benech, "Gain Enhancement of Suspended Miniaturized Antenna on High-loss paper substrate", *2017 IEEE International Symposium on Antennas and Propagation/USNC-URSI National Radio Science meeting*, San Diego, 9-14 July 2017
- [6] T. Q. V Hoang, **D. H. N Bui**, T. P. Nguyen, T.P. Vuong, C. Defay, "Passive Battery-Free UHF RFID Tag for Athermic Car Windshields", *2017 IEEE International Symposium on Antennas and Propagation/USNC-URSI National Radio Science meeting*, San Diego, 9-14 July 2017.
- [7] **D. H. N Bui**, T.P. Vuong, G. Depres, J. Verdier, B. Allard, P. Benech, "Coplanar Multiband Antenna on Flexible substrate in Energy Harvesting System for IoT Applications", *2018 European Conference on Antennas and Propagation*, London, April 2018, **submitted**

National conferences

- [1] **D. H. N Bui**, T. P. Vuong, J. Verdier, B. Allard, P. Benech, "Antennes souples imprimables pour la récupération de champs électromagnétiques ambiants", *Assemblée Générale GDR Ondes*, Ecully, France, Oct 2015
- [2] **D. H. N Bui**, T. P. Vuong, J. Verdier, B. Allard, P. Benech, " Antennes multibandes pour la récupération d'énergies sans fils", *Journées Nationales du Réseau Doctoral en Micro-nanoélectronique (JNRDM)*, Toulouse, 11-13 Mai 2016.

- [3] **D. H. N Bui**, T.P. Vuong, J.Verdier, B. Allard, P. Benech, “Multi-frequency solution for Energy harvesting RF ambient energy”, *6iemes Journees Nationales sur la Recuperation et le Stockage de l’energie pour alimentation de microsystemes autonomes (JNRSE2016)*, pp. 48-49, Bordeaux, 9-10 Mai 2016.
- [4] **D. H. N Bui**, T. P. Vuong, J.Verdier, B. Allard, P. Benech, “Diplexeur compacte à faible perte pour la recuperation d’energie ambiante”, *20èmes Journees Nationales Microondes (JNM2017)*, Saint Malo, 16-19 Mai 2017.
- [5] **D. H. N Bui**, T.P. Vuong, J.Verdier, B. Allard, P. Benech, “ Design and integration of flexible antenna in RF energy harvesting circuit”, *7iemes Journees Nationales sur la Recuperation et le Stockage de l’energie pour alimentation de microsystemes autonomes (JNRSE2017)*, Lyon, 9-10 Mai 2017.

List of acronyms and abbreviations

IoT	Internet-of-Things
3D	3-dimensional
RF	Radio Frequency
DC	Direct Current
RFID	Radio Frequency Identification
DSRC	Dedicated Short Range Communications
ICNIRP	International commission on non-ionizing radiation protection
IEEE	Institute of Electrical and Electronics Engineers
ICES	IEEE International Committee on Electromagnetic Safety
EU	European Union
ANFR	National Agency of Frequencies of France
FM	Frequency Modulation
RNT	Radio Numérique Terrestre (Digital Terrestrial Radio)
PMR	Professional Mobile Radio
TV	Television
GSM	Global System for Mobile Communications
UMTS	Universal Mobile Telecommunications System
WLAN	Wireless Local Area Network
LTE	Long-Term Evolution
WiMAX	Worldwide Interoperability for Microwave Access
EIRP	Equivalent Isotropically Radiated Power
CMOS	Complementary Metal-Oxide-Semiconductor
RFoM	Figure of Merit
LED	Light-Emitting Diode
PMMs	Power Management Modules
MPP	Maximum Power Point
PEDOT	Poly(3,4-ethylenedioxythiophene)
Ppy	Polypyrrole
AMC	Artificial Magnetic Conductor
FSS	Frequency Selective Surfaces
VNA	Vector Network Analyzer

PET	Polyethylene Terephthalate
SMD	Surface-Mount Technology
ESR	Equivalent Series Resistor
ESL	Equivalent Series Inductor
MIMO	Multiple-Input Multiple-Output
PDF	Probability Density Function
CDF	Cumulative Density Function
CPW	Coplanar Waveguide
SIW	Substrate integrated waveguide

Résumé

L'Internet-of-Things désigne un développement en plein essor d'objets interconnectés et qui sont susceptibles de modifier nombre de services au sein de l'industrie comme pour la personne. Les développements actuels buttent sur plusieurs verrous dont celui de l'autonomie énergétique des objets ou encore des procédés de fabrication économiquement acceptables et respectueux de la planète. Dans ce contexte, la récupération d'énergie est une thématique largement répandue faisant appel à des sources très variées (mécanique, thermique, électromagnétique...). Cette thèse est notamment orientée vers la récupération d'énergie électromagnétique ambiante. Le second point caractéristique de cette thèse est de s'intéresser à des substrats souples et si possible recyclables. Le défi consiste à récupérer l'énergie provenant d'un champ électromagnétique ambiant extrêmement faible : ceci concerne l'antenne, qui doit par ailleurs répondre à une exigence de flexibilité pour son intégration future à un objet souple et déformable, et l'électronique de traitement de l'énergie.

Le travail de thèse est articulé autour de trois phases principales

Dans la première phase, il s'agissait de l'étude des structures d'antennes compatibles en fréquence et en puissance reçue avec l'application de récupération d'énergie et une réalisation physique sur base souple (papier, tissu...). Cette phase a permis de présenter les différentes approches pour combiner les sources RF.

Dans la deuxième phase, il s'agit de l'étude sur le rôle de circuits redresseurs dans le système de récupérer d'énergie. Les méthodes d'extraction des paramètres sont discutées en dissociant chaque élément et leurs rôles. De nombreuses mesures ont été réalisées afin de comparer différents modèles de la diode utilisée pour le redressement, en tenant compte également de l'impact réel du processus de fabrication et du processus de mesure.

Une troisième phase permet l'optimisation de l'ensemble antenne et électronique (rectenna) pour divers scénarii et le suivi de la variabilité pour maintenir les pertes du système à minima. La réalisation de démonstrateurs pertinents, testés et caractérisés est présentée.

Mot clés : antenne, récupération d'énergie, matériaux souples, antenne 3D, antenne diversité

Abstract

Internet-of-Things means a growing development of interconnected objects that are likely to change many services within the industry as well as for the individual. Several barriers, including the energy autonomy of objects or production processes that are economically acceptable and respectful of the planet, hamper current developments. In this context, energy recovery is a widespread theme using a wide range of sources (mechanical, thermal, electromagnetic, etc.). This thesis is oriented towards the recovery of ambient electromagnetic energy. The second characteristic point of this thesis is to focus on flexible and, if possible, recyclable substrates. The challenge is to recover energy from an extremely low ambient electromagnetic field: this concerns the antenna, which must also meet a requirement for flexibility for its future integration with a flexible and deformable object, and the electronics of energy processing.

The work of this thesis conducted in three phases.

In the first phase, it was the study of the antenna structures compatible with frequency and power received with the energy harvesting application and a physical realization on flexible base (paper, textile, etc.). This phase allowed presenting the different approaches to combining the RF sources.

In the second phase, the study on the role of rectifying circuit in the system of recovering wireless energy was presented. Methods for extracting parameters were discussed by separating each element and its roles. Numerous measurements have been conducted to compare different models of the diode, taking into account also the actual impact of the manufacturing process and the measurement process.

A third phase allows the optimization of the antenna and electronic assembly (rectenna) for various scenarios and the monitoring of variability to keep the losses of the system at minima. The production of relevant demonstrators, test, and characterization were presented.

Keywords: antenna, RF energy harvesting, flexible material, 3D-antenna, diversity antenna